Fall 2014

Excited states of chromophores and vibronic interactions

Benjamin T. Nebgen
Purdue University

Recommended Citation

Nebgen, Benjamin T., "Excited states of chromophores and vibronic interactions" (2014). *Open Access Dissertations*. 338.
https://docs.lib.purdue.edu/open_access_dissertations/338

Graduate School Form 30
(Updated 11/20/2014)

PURDUE UNIVERSITY
GRADUATE SCHOOL
Thesis/Dissertation Acceptance

This is to certify that the thesis/dissertation prepared

By Benjamin T. Nebgen

Entitled
EXCITED STATES OF CHROMOPHORES AND VIBRONIC INTERACTIONS

For the degree of Doctor of Philosophy

Is approved by the final examining committee:

Lyudmila Slipchenko

Timothy Zwier

Adam Wasserman

Garth J. Simpson

To the best of my knowledge and as understood by the student in the Thesis/Dissertation Agreement, Publication Delay, and Certification/Disclaimer (Graduate School Form 32), this thesis/dissertation adheres to the provisions of Purdue University's "Policy on Integrity in Research" and the use of copyrighted material.

Approved by Major Professor(s): Lyudmila Slipchenko

Approved by: R. E. Wild 12/03/2014

Head of the Department Graduate Program Date

EXCITED STATES OF CHROMOPHORES AND VIBRONIC INTERACTIONS

A Dissertation

Submitted to the Faculty

of

Purdue University

by

Benjamin T. Nebgen

In Partial Fulfillment of the

Requirements for the Degree

of

Doctor of Philosophy

December 2014

Purdue University

West Lafayette, Indiana

To my parents Mark and Nancy for getting me here. To my soon to be wife, Kelly, for getting me through.

ACKNOWLEDGMENTS

I would like to thank Dr. Lyudmila Slipchenko for her great amount of advice over the last 4.5 years. I would like to acknowledge the Fredrick N. Andrews Purdue Fellowship as well as the NSF for funding.

TABLE OF CONTENTS

Page

LIST OF TABLES

LIST OF FIGURES

ABSTRACT

Nebgen, Benjamin T. Ph.D., Purdue University, December 2014. Excited States of Chromophores and Vibronic Interactions. Major Professor: Lyudmila V. Slipchenko.

The main focus of my Ph.D. work has been on building a vibronic coupling model for multichromophores and extending that model to more general systems. This Dissertation serves as both a summary of this work as well as a manual for the two vibronic coupling programs I have written. It is my hope that the instructions written here are complete enough for any who would like to replicate my work on vibronic coupling on other systems.

Additionally, I have also worked on a few purely computational projects not directly related to the vibronic coupling work. The status of these projects is recorded here. Chapter 5 details electronic structure calculations of the α-methylbenzyl radical and there use in determining the excited state geometry of the methyl rotor next to a radical center. Chapter 6 discusses ab-initio simulations of the phenylcyanomethyl molecule and explores the vibrational envelope following the $D_0 \rightarrow D_1$ transition. Finally, Chapter 7 examines the ultrafast radiationless decay of the photoacid 3-cyano-6-hydroxycoumarin in relation to the proton transfer to solvent mechanism.

1. THEORETICAL TREATMENT OF VIBRONIC COUPLING IN ASYMMETRIC BICHROMOPHORES

1.1 Introduction

The interaction of light and matter is a fundamental phenomenon of which understanding and control are quintessential for advances in science and technology. Often, quantum-mechanical treatment of the light-induced processes can be simplified by separating electronic and nuclear degrees of freedom by introducing the conventional Born-Oppenheimer approximation. [1] Yet, to explain processes such as conversion of solar to electrical energy as occurs in photosynthetic centers of plants and bacteria and is mimicked in photovoltaic devices, the electronic and nuclear motions cannot be uncoupled such that the BO approximation should be abandoned. A wide variety of classical, semi-classical, and quantum techniques have been suggested to simulate dynamics in such systems. [2] In classical approaches the nuclear wavepacket is approximated by an ensemble of particles that follow classical trajectories. Semi-classical methods add some missing quantum effects to this picture by allowing transitions between the electronic states, for example through surface-hopping [3] or using mean-field approximation [4, 5]. In quantum-dynamics methods the nuclear wavepacket is described by including quantum effects, such as interference between different parts of the packet. [6, 7]

Alternatively, one can circumvent complexities associated with modeling dynamics of vibronic systems and describe their vibronic spectra statically. This can be accomplished by solving the time-independent Schrodinger equation with an electronic-nuclear Hamiltonian. This work employs the latter (static) approach to a molecular system composed of two (nearly) identical chromophores. Such bichromophores have nearly degenerate electronic energy levels with an energy splitting close to the separation in vibrational energy levels, resulting in coupling of the electronic and nuclear degrees of freedom. Pioneering work in this direction was done by Fulton and Gouterman. [8, 9] They developed a vibronic theory (FG model) describing bichromophores possessing a specific symmetry element exchanging the monomer Hamiltonians. [9, 10] Since then, FG model has been applied to a number of molecular dimers [11–16], extended to include multiple vibrational modes [17–19] and to describe vibronic states in more complex molecular aggregates [20, 21].

The original FG model is limited to cases where the dimer has a symmetry element interchanging the Hamiltonians of monomers. The symmetry element simplifies the dimer Hamiltonian and its numerical solution. However, at the expense of increased computational complexity, the Hamiltonian can be left in the asymmetric form and, after expanding the vibrational wave function in a basis, diagonalized numerically using the iterative Lanczos diagonalization routine, as perviously suggested by Domcke and co-workers. [22] This approach can handle asymmetries arising from asymmetric molecular orientations, substituent groups or partial deuteration, or from effects of environment, as would occur in realistic biological or materials systems. This work presents an extension of the FG model to asymmetric bichromophores. Additionally, the Hamiltonian for the inter-chromophore vibrational modes, i.e., vibrations that occur between the chromophores themselves, is introduced and included in the vibronic model. The inter-monomer Hamiltonian is fundamentally different from the intra-monomer one because the electronic coupling depends on the distance and orientation between the two monomers and thus upon the inter-monomer vibrations. To characterize the developed model, a series of model spectra are produced and analyzed. As a stringent test, the extended FG model is applied to vibronic spectra of flexible bichromophore diphenylmethane (DPM), which has been the subject of many spectroscopic studies over the last half century. [23–27]

1.2 Theory

For a bichromophore (also called dimer) composed of two (nearly) identical monomers, the Hamiltonian can be written as a sum of the monomer Hamiltonians and electronic coupling $V_{AB}(L)$ and kinetic energy T_L terms:

$$H = H_A + H_B + V_{AB}(L) + T_L \tag{1.1}$$

The electronic coupling and the kinetic energy terms depend on the vector of six inter-monomer vibrational modes L. In this treatment, the electronic wavefunction of the dimer is not antisymmetrized, i.e., the electron exchange between the two monomers is neglected. This is a reasonable assumption for a large class of molecules, especially when monomers are spatially separated.

Vibrations considered in this model are divided into intra-monomer and inter-monomer vibrations. Intra-monomer modes have kinetic and potential energy terms located within H_A and H_B and thus can be computed by calculations on either monomer. The inter-monomer modes are vibrations along the L vector introduced above. Typically, the inter-monomer modes have much lower frequencies than the intra-monomer modes. They cannot be obtained from monomer properties but require (partial) knowledge of the dimer Hessian. Because of these principal differences, the treatment of the intra- and inter-monomer modes in the model should be different. Note that only the intra-monomer modes were considered in the original FG model and most extensions. The current paper provides the first systematic extension of the FG model to the inter-monomer vibrations.

1.2.1 Intra-monomer Modes

Main steps of the FG model are repeated here in order to introduce notations and bring into context our developments. For the intra-monomer modes, the Hamiltonian of monomer A (and analogously for monomer B) is written as a sum of the vibrational kinetic energy term $T_A(Q_A)$ and the electronic Hamiltonian $h_A(q_A; Q_A)$:

$$H_A = h_A(q_A; Q_A) + T_A(Q_A) \tag{1.2}$$

The electronic Hamiltonian depends explicitly on the electron coordinate (q_A) and parametrically on the nuclear coordinate (Q_A) of monomer A. Let $\{\psi_i^{\text{el}}\,(q_A; Q_A)\}_{\forall i\geq 0}$ be the eigenvectors of the electronic Hamiltonian h_A with energies $E_i(Q_A)$; $\{\phi_j\,(Q_A)\}_{\forall j\geq 0}$ be the eigenvectors of the vibrational Hamiltonian $E_i(Q_A) + T_A(Q_A)$. Since similar relationships hold for monomer B, $H_A + H_B$ will satisfy the eigenvalue problem:

$$\begin{aligned}(H_A{+}H_B)\psi_i^{\text{el}}\,(q_A; Q_A)\,\phi_n\,(Q_A)\,\psi_j^{\text{el}}\,(q_B; Q_B)\,\phi_m\,(Q_B)\\ = E_{i,j,n,m}(Q_A, Q_B)\psi_i^{\text{el}}\,(q_A; Q_A)\,\phi_n\,(Q_A)\,\psi_j^{\text{el}}\,(q_B; Q_B)\,\phi_m\,(Q_B)\end{aligned} \tag{1.3}$$

where

$$E_{i,j,n,m}(Q_A, Q_B) = E_{i,n}(Q_A) + E_{j,m}(Q_B) \tag{1.4}$$

i and j represent the level of electronic excitation on monomers A and B respectively. Similarly, n and m represent the vibrational excitation on either monomer.

Before introducing the electronic coupling, the energies obey the following relation:

$$E_{i,j,n,m} = E_{j,i,m,n} \tag{1.5}$$

The degeneracy in the electronic states is split by the electronic coupling term $V_{AB}(L)$ in the electronic Hamiltonian Eq. (1.1).

Consider now a pair of exciton states. The excitation may occur either on monomer A or monomer B; neither double excitations (both on A and B) or charge-transfer excitations (electron moves from A to B or vice versa) are considered in this model. Thus, a two element basis is sufficient for the electronic wavefunction:

$$\{\pi_A^{(1)} = \psi_1^{\text{el}}\psi_0^{\text{el}}, \pi_B^{(1)} = \psi_0^{\text{el}}\psi_1^{\text{el}}\} \tag{1.6}$$

Though the following derivations are valid for any electronic states in the monomer, for the sake of simplicity, we use the notations corresponding to the electronic transition from the ground state ψ_0 to the first electronic excited state ψ_1.

To find algebraic expressions for the vibrational energies, the Hamiltonian has to be expanded in the electronic basis, resulting in the following matrix elements:

$$\left\langle \pi_A^{(1)} \middle| H \middle| \pi_A^{(1)} \right\rangle = T_A + E^{(1)}\left(Q_A\right) + T_B + E^{(0)}\left(Q_B\right) + \left\langle \pi_A^{(1)} \middle| V_{AB} \middle| \pi_A^{(1)} \right\rangle \tag{1.7}$$

$$\left\langle \pi_B^{(1)} \middle| H \middle| \pi_B^{(1)} \right\rangle = T_A + E^{(0)}\left(Q_A\right) + T_B + E^{1}\left(Q_B\right) + \left\langle \pi_B^{(1)} \middle| V_{AB} \middle| \pi_B^{(1)} \right\rangle \tag{1.8}$$

$$\left\langle \pi_A^{(1)} \middle| H \middle| \pi_B^{(1)} \right\rangle = \left\langle \pi_B^{(1)} \middle| H \middle| \pi_A^{(1)} \right\rangle = \left\langle \pi_A^{(1)} \middle| V_{AB} \middle| \pi_B^{(1)} \right\rangle \tag{1.9}$$

In case of the intra-monomer modes, $V_{AB}(L)$ is expanded in Taylor series about the equilibrium position of $L = 0$ and only the zero-order term is kept:

$$\begin{aligned} \left\langle \pi_A^{(1)} \middle| V_{AB}(L) \middle| \pi_B^{(1)} \right\rangle &\simeq \left\langle \pi_A^{(1)} \middle| V_{AB}(0) \middle| \pi_B^{(1)} \right\rangle \\ &+ \frac{\partial}{\partial L} \left\langle \pi_A^{(1)} \middle| V_{AB}(L) \middle| \pi_B^{(1)} \right\rangle \bigg|_{L=0} L + \frac{\partial^2}{\partial^2 L} \left\langle \pi_A^{(1)} \middle| V_{AB}(L) \middle| \pi_B^{(1)} \right\rangle \bigg|_{L=0} \frac{L^2}{2} \end{aligned} \tag{1.10}$$

The remaining terms in the Taylor expansion along with the T_L term will be considered in the subsequent section regarding inter-monomer modes. Assuming the harmonic approximation for the potential energy surface in the vicinity of the minimum provides a functional form for $E^{(0)}(Q_A)$, $E^{(1)}(Q_A)$, $E^{(0)}(Q_B)$, and $E^{(1)}(Q_B)$. For example, for monomer A:

$$E^{(0)}\left(Q_A\right) = \frac{1}{2} M \omega_A^2 Q_A^2 \tag{1.11}$$

$$E^{(1)}\left(Q_A\right) = E_e + l_A Q_A + \frac{1}{2} M \omega_{*A}^2 Q_A^2 \tag{1.12}$$

where M is the reduced mass, ω is the characteristic frequency of the normal mode in the ground state, and ω_{*A} is the characteristic frequency of the normal mode in the excited state. The displacement l_A is defined as

$$l_A = dQ M \omega_A^2 \tag{1.13}$$

dQ is the displacement along the normal mode between geometries of the ground and excited states (see Fig. (1.1)). For simplicity $Q_A = 0$ is defined as the equilibrium

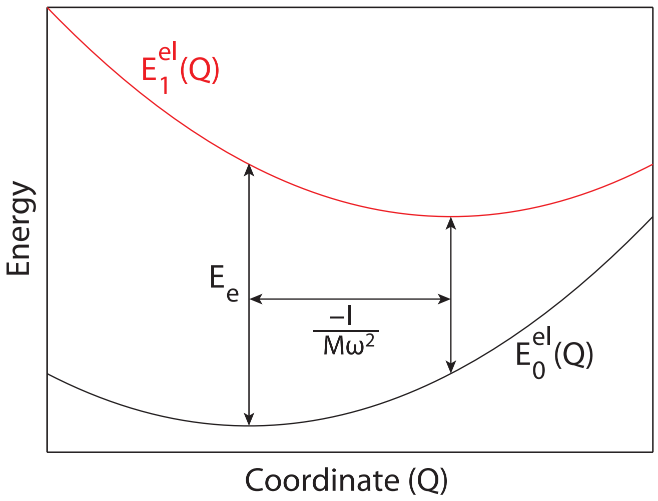

Figure 1.1. Potential energy surfaces for the ground (black) and excited (red) electronic state along vibrational mode Q. E_e is the vertical excitation energy and $\frac{-l}{M\omega^2}$ is the displacement between the two minima.

position for the normal mode in the ground electronic state, such that a linear term is only present in the expression for the excited state potential energy surface.

While the $\left\langle \pi_A^{(1)} \middle| V_{AB} \middle| \pi_A^{(1)} \right\rangle$ could be evaluated from standard electronic structure packages by modifications of the electronic structure integral codes, it is not necessary for bichromophores with symmetric electronic wavefunction since, by symmetry,

$$\left\langle \pi_A^{(1)} \middle| V_{AB} \middle| \pi_A^{(1)} \right\rangle = \left\langle \pi_B^{(1)} \middle| V_{AB} \middle| \pi_B^{(1)} \right\rangle \tag{1.14}$$

Thus, these terms shift all energy levels by the same quantity and do not affect energy spacings. The Leutwyler group studied electronic wavefunction asymmetry in the 2-pyridone·6-methyl-2-pyridone dimer using precisely these constants. [15]

To summarize, the Hamiltonian in the electronic basis can be written as:

$$H = \begin{pmatrix} \frac{P_A^2}{2M} + E_A + l_A Q_A + \frac{1}{2} M\omega_{*A}^2 Q_A^2 + \frac{P_B^2}{2M} + \frac{1}{2} M\omega_B^2 Q_B^2 & V_{AB} \\ V_{AB} & \frac{P_A^2}{2M} + \frac{1}{2} M\omega_A^2 Q_A^2 + \frac{P_B^2}{2M} + E_B + l Q_B + \frac{1}{2} M\omega_{*B}^2 Q_B^2 \end{pmatrix} \tag{1.15}$$

The electronic coupling (or resonance integral) V_{AB} term can be evaluated by a number of perturbative or supermolecular techniques. [28, 29] In this work, the coupling is calculated as half the splitting between the exciton states of the dimer.

In the original FG model, the Hamiltonian in Eq. (1.15) is transformed to a symmetric basis:

$$\pi_{+}^{(1)} = \frac{1}{\sqrt{2}}\left(\pi_{A}^{(1)} + \pi_{B}^{(1)}\right) \tag{1.16}$$

$$\pi_{-}^{(1)} = \frac{1}{\sqrt{2}}\left(\pi_{A}^{(1)} - \pi_{B}^{(1)}\right) \tag{1.17}$$

This unitary transformation does not change the eigenvalues of the Hamiltonian. In addition to the electronic basis transformation, Fulton and Gouterman used a vibrational coordinate transformation from Q_A and Q_B to:

$$Q_{\pm} = \frac{1}{\sqrt{2}}\left(Q_A \pm Q_B\right) \tag{1.18}$$

This step simplifies diagonalization of the Hamiltonian, but only when the dimer has a symmetry element ensuring $l_A = l_B$, $\omega_A = \omega_B$, and $\omega_{*A} = \omega_{*B}$.

In order to extend the model to asymmetric dimers, the transformation to the symmetric basis is omitted. By expressing momentum and position operators with raising and lowering operators and assuming a harmonic basis, the Hamiltonian matrix elements are:

$$\begin{aligned}\left\langle \pi_{A}^{(1)} \middle| H \middle| \pi_{A}^{(1)} \right\rangle = {} & b_A \hbar\omega_A \left(\sqrt{n+1}\,\delta_{(n',n+1)} + \sqrt{n}\,\delta_{(n',n-1)}\right)\delta_{(m',m)} + \\ & \left(\frac{\hbar\omega_A}{2}\left(\left(\frac{\omega_{*A}}{\omega_A}\right)^2 + 1\right)\left(n + \frac{1}{2}\right) + \hbar\omega_B\left(m + \frac{1}{2}\right) + E_A\right)\delta_{(n',n)}\delta_{(m',m)}\end{aligned} \tag{1.19}$$

$$\begin{aligned}\left\langle \pi_{B}^{(1)} \middle| H \middle| \pi_{B}^{(1)} \right\rangle = {} & b_B \hbar\omega_B \left(\sqrt{m+1}\,\delta_{(m',m+1)} + \sqrt{m}\,\delta_{(m',m-1)}\right)\delta_{(n',n)} + \\ & \left(\hbar\omega_A\left(n + \frac{1}{2}\right) + \frac{\hbar\omega_B}{2}\left(\left(\frac{\omega_{*B}}{\omega_B}\right)^2 + 1\right)\left(m + \frac{1}{2}\right) + E_B\right)\delta_{(n',n)}\delta_{(m',m)}\end{aligned} \tag{1.20}$$

$$\left\langle \pi_{A}^{(1)} \middle| H \middle| \pi_{B}^{(1)} \right\rangle = \left\langle \pi_{B}^{(1)} \middle| H \middle| \pi_{A}^{(1)} \right\rangle = V_{AB}\,\delta_{(n',n)}\delta_{(m',m)} \tag{1.21}$$

n and n' (m and m') represent the excitation quanta of a given normal mode for the vibration on A (B) monomer. Dimensionless displacement parameters b_A and b_B are related to l_A and l_B as

$$b_A \hbar \omega_A = l_A \sqrt{\frac{\hbar}{2M\omega_A}} \tag{1.22}$$

The expressions in Eqs. (1.19)-(1.21) are expanded in the vibrational basis. The solution generally converges rapidly, requiring around five basis functions in each vibration for spectroscopically reasonable values of b_A and b_B. Convergence with respect to the size of the basis is shown in Section (1.5).

Eqs. (1.19)-(1.21) can be extended in a straightforward manner for multiple vibrational modes on each monomer. In this case, each matrix element is a sum over Hamiltonians for different vibrations and the basis functions are products of the basis function from each vibration.

As pointed out by Förster and others [13,29] there are different regimes of vibronic coupling: strong, weak, and intermediate. The quantity that characterizes a mode as either being strongly coupled or weakly coupled to the electronic excitation is given as [9,10]

$$p = \frac{2\left|\left\langle \pi_A^{(1)} \right| V_{AB} \left| \pi_B^{(1)} \right\rangle\right|}{M\omega^2 dQ^2} \tag{1.23}$$

Here, $p >> 1$ corresponds to strongly coupled systems; $p << 1$ characterizes weakly coupled systems. $p \simeq 1$ defines the intermediate coupling regime which exhibits the most complicated spectra. For a vibration in the strong or weak limit, it is possible to analytically compute the energies and intensities. [13] Application of perturbation theory to strong and weak coupling regimes is shown in Section (1.4). However, analytic solutions break down as the vibration enters the intermediate coupling regime. Therefore, in the present work, numerical diagonalization of the Hamiltonian using the Lanczos algorithm is employed for all cases, resulting in what Andrzejak and Petelenz call the exact numerical solution. [13]

1.2.2 Zero Point Energy Level Splitting

One of the key effects of asymmetry is that the excitation energies of the two monomers in symmetric bichromophores are the same ($E_A = E_B$), while in asymmetric bichromophores they are different ($E_A \neq E_B$). An example of a molecular change that can lead to this effect is when one monomer has certain elements replaced by different isotopes from the other, as will be examined in Section 1.7. In such a case, the excitation energies of deuterated and non-deuterated monomers are slightly different due to zero point vibrational energies (ZPVE). Vibrational modes contribute to ZPVE whether or not they are explicitly included in the vibronic coupling model Hamiltonian. For modes that are explicitly included in the Hamiltonian, the effect on ZPVE can be accounted for by using an appropriate value of ω_*, the excited state frequency of a vibrational mode, in Eq. 1.11.

For vibrational modes that are not directly included in the vibronic coupling calculation, changes in the ZPVE can be accounted for with a new parameter defined as:

$$\begin{aligned} \Delta\Delta ZPVE = E_A - E_B = \left(E_e + E_e^H\right) - \left(E_e + E_e^D\right) = \\ \sum_m \left(\frac{\hbar\omega_m^{H*}}{2} - \frac{\hbar\omega_m^H}{2}\right) - \sum \left(\frac{\hbar\omega_n^{D*}}{2} - \frac{\hbar\omega_n^D}{2}\right) \end{aligned} \tag{1.24}$$

Where E_e is the electronic excitation energy which is nearly the same for the two monomers. $E_e^{H/D}$ are the contributions to the excitation energy due to changes in vibrational frequencies between the ground and excited states of the non-deuterated and deuterated monomers, respectively. In Eq. 1.24, n and m range over all modes on the deuterated and non-deuterated monomers that are not explicitly included in the vibronic coupling model Hamiltonian (Eq. 1.15). Thus, $\Delta\Delta ZPVE$ is the difference between the change in ZPVEs between the ground and excited states for the deuterated and non-deuterated monomers. This is the only additional parameter needed to model molecules that have broken vibrational symmetry but retain electronic symmetry. Formally, this parameter is identical to the parameter used by Leutwyler et al. to simulate broken electronic symmetry. [15] $\Delta\Delta ZPVE$ term is added to upper left hand block of the Hamiltonian in Eq. 1.15.

1.2.3 Inter-monomer Modes

To compute the eigenstates of inter-monomer vibrations, it is necessary to account for the inter-monomer kinetic energy term, T_L from Eq. (1.1), as well as higher order terms from the Taylor expansion of V_{AB} in Eq. (1.10). In order to build a total Hamiltonian, the inter-monomer Hamiltonian will be constructed in the $\{\pi_A^{(1)}, \pi_B^{(1)}\}$ basis and added onto the intra-monomer Hamiltonian. However, because the inter-monomer modes are inherently dependant on the electronic state geometries of the dimer, it is convinient to work in the symmetrized basis $\{\pi_+^{(1)}, \pi_-^{(1)}\}$ as defined in Eqs. (1.16) and (1.17) which more closely resembles the actual dimer electronic wavefunctions. So, the Hamiltonian matrix elements of T_L and $V_{AB}(L)$ are first evaluated in the symmetrized basis $\{\pi_+^{(1)}, \pi_-^{(1)}\}$ and then transformed to the monomer basis $\{\pi_A^{(1)}, \pi_B^{(1)}\}$ and added to the Hamiltonian of the intra-monomer modes.

Since the geometries of both exciton states $\pi_+^{(1)}$ and $\pi_-^{(1)}$ are different from the ground state geometry along the inter-monomer mode L, the excited state surfaces are described as displaced parabolas. Thus, for geometries near the minima of the excited states:

$$\left\langle \pi_+^{(1)} \middle| V_{AB}(L) + T_L \middle| \pi_+^{(1)} \right\rangle = l_+ L + \frac{1}{2} M \omega_+^2 L^2 + \frac{P_+^2}{2M} \tag{1.25}$$

$$\left\langle \pi_-^{(1)} \middle| V_{AB}(L) + T_L \middle| \pi_-^{(1)} \right\rangle = l_- L + \frac{1}{2} M \omega_-^2 L^2 + \frac{P_-^2}{2M} \tag{1.26}$$

where l_+ and l_- are the displacement parameters analogous to the l_A and l_B terms in the intra-monomer mode case. In the dimer basis, each mode has two displacement parameters (l_+ and l_-) corresponding to the displacements between the ground and first and second exciton states. P_+ and P_- are the kinetic energy terms for the inter-monomer mode in the exciton states. The off-diagonal terms of the inter-monomer

Hamiltonian are zero for symmetric electronic wave function due to the hermicity of V_{AB} and T_L:

$$\begin{aligned}&\left\langle \pi_{+}^{(1)} \middle| V_{AB}(L) + T_L \middle| \pi_{-}^{(1)} \right\rangle = \\ &\quad \frac{1}{2}\left(\left\langle \pi_A^{(1)} \left| V_{AB}(L) + T_L \right| \pi_A^{(1)} \right\rangle - \left\langle \pi_B^{(1)} \left| V_{AB}(L) + T_L \right| \pi_B^{(1)} \right\rangle\right) = 0\end{aligned} \tag{1.27}$$

The reverse transformation from dimer symmetrized electronic basis into the monomer localized basis can be realized by using the following matrix equality:

$$\begin{bmatrix} \pi_A^{(1)} \\ \pi_B^{(1)} \end{bmatrix} = \frac{1}{\sqrt{2}} \begin{bmatrix} 1 & 1 \\ 1 & -1 \end{bmatrix} \begin{bmatrix} \pi_{+}^{(1)} \\ \pi_{-}^{(1)} \end{bmatrix} \tag{1.28}$$

Applying this matrix transformation to the $V_{AB}(L) + T_L$ terms results in the following form of the inter-monomer mode Hamiltonian:

$$\begin{aligned}&\left\langle \pi_A^{(1)} \middle| V_{AB}(L) + T_L \middle| \pi_A^{(1)} \right\rangle = \left\langle \pi_B^{(1)} \middle| V_{AB}(L) + T_L \middle| \pi_B^{(1)} \right\rangle \\ &\quad = \frac{1}{2}\left(l_{+} + l_{-}\right) L + \frac{1}{2}\left(\frac{1}{2} M\omega_{+}^{2} + \frac{1}{2} M\omega_{-}^{2}\right) L^2\end{aligned} \tag{1.29}$$

$$\begin{aligned}&\left\langle \pi_A^{(1)} \middle| V_{AB}(L) + T_L \middle| \pi_B^{(1)} \right\rangle = \left\langle \pi_B^{(1)} \middle| V_{AB}(L) + T_L \middle| \pi_A^{(1)} \right\rangle \\ &\quad = \frac{1}{2}\left(l_{+} - l_{-}\right) L + \frac{1}{2}\left(\frac{1}{2} M\omega_{+}^{2} - \frac{1}{2} M\omega_{-}^{2}\right) L^2\end{aligned} \tag{1.30}$$

The Hamiltonian described in Eqs. (1.29) and (1.30) can be added to the intra-monomer mode Hamiltonian (Eqs. (1.19)–(1.21)), expanded in a vibrational basis of inter- and intra- monomer modes, and numerically diagonalized.

1.2.4 Intensities

Diagonalizing the Hamiltonian (Eqs. (1.19)–(1.21), (1.29), and (1.30)) results in the vibrational substructure of the exciton states. Evaluation of the intensities of the vibronic states in a fluorescence spectrum is discussed in this subsection. Absorption intensities can be derived analogously. Following Fulton and Gouterman, [9] the transition dipoles of a symmetric R^+ and antisymmetric R^- excited state to the ground state are:

$$R^+ = \int\int \psi_1(q;Q,L)^* M^+ \psi_0(q;Q,L) dq \phi_1(Q,L)^* \phi_0(Q,L) dQ dL \tag{1.31}$$

$$R^- = \int\int \psi_1(q;Q,L)^* M^- \psi_0(q;Q,L) dq \phi_1(Q,L)^* \phi_0(Q,L) dQ dL \tag{1.32}$$

where $\psi_1(q;Q,L)$ is the initial (excited state) electronic wavefucntion of the dimer, $\phi_1(Q,L)$ is the initial vibrational wavefunction, $\psi_0(q;Q,L)$ and $\phi_0(Q,L)$ are the final (ground state) electronic and vibrational wavefunctions (the latter is not necessarily the wavefunction with no vibrational excitations). M^+ and M^- are the symmetric and antisymmetric transition dipole operators. The evaluation of R^+ shall now be demonstrated while R^- can be obtained analogously. Assuming that the electronic wave function is not strongly effected by the changes in vibrational coordinates, the integral over electronic coordinates and transition dipole operator may be factored out of the integral over nuclear coordinates. Expanding $\psi_1(q)$ in the vibrational basis results in:

$$\begin{aligned}\psi_1(q) = {} & \pi_A^{(1)} \sum_n \sum_m \sum_p C^A_{n,m,p} \phi_n(Q_A) \phi_m(Q_B) \phi_p(L) \\ & + \pi_B^{(1)} \sum_n \sum_m \sum_p C^B_{n,m,p} \phi_n(Q_A) \phi_m(Q_B) \phi_p(L)\end{aligned} \tag{1.33}$$

where $\{C^A_{n,m,p}, C^B_{n,m,p}\}$ are the expansion coefficients representing the dimer vibrational wavefunction in the basis of monomer vibrational wavefunctions. Eq. (1.33) can be transformed into the symmetrized electronic dimer basis by applying Eq. (1.16). It is easy to see that the evaluation of the symmetric transition dipole moment R^+ reduces to calculation of the vibrational overlap integral and the purely electronic transition dipole moment between the ground and symmetric excited state $\pi_+^{(1)}$:

$$\int \pi_+^{(1)} M^+ \psi_0 dq \tag{1.34}$$

To show that the transition dipole moment between the symmetric dipole operator and antisymmetric wavefunction is zero, the transition dipole operators in the symmetrized basis M^+ and M^- must be decomposed into localized monomer transition dipoles M^a and M^b:

$$M^+ = M^a + M^b \tag{1.35}$$

$$M^- = M^a - M^b \tag{1.36}$$

While this is mathematically allowed, the values for the monomer transition dipole moments M^a and M^b cannot be easily found from quantum simulation. Therefore, the intensity calculations are carried out in the symmetrized electronic basis (Eqs. (1.16) and (1.16)). Since M^a and M^b are localized operators on either the A or B monomers, the integrals of a transition dipole operator on A integrated over the wavefunction of the B monomer is zero and vice versa:

$$\int \pi_a^{(1)} M^b \pi_a^{(0)} dq = 0 \tag{1.37}$$

$$\int \pi_b^{(1)} M^a \pi_b^{(0)} dq = 0 \tag{1.38}$$

Likewise, the magnitude of the electronic transition dipole moments on either monomer must be the same:

$$\int \pi_a^{(1)} M^a \pi_a^{(0)} dq = \int \pi_b^{(1)} M^b \pi_b^{(0)} dq \tag{1.39}$$

Combining Eqs. (1.37) and (1.39), the integral between the antisymmetric wavefunction and the symmetric dipole operator is zero:

$$\begin{aligned} &\int \frac{1}{\sqrt{2}} \left(\pi_a^{(1)} - \pi_b^{(1)}\right) \left(M^a + M^b\right) \pi_a^{(0)} \pi_b^{(0)} dq \\ &= \frac{1}{\sqrt{2}} \left(\int \pi_a^{(1)} M^a \pi_a^{(0)} dq - \int \pi_b^{(1)} M^b \pi_b^{(0)} dq \right) = 0 \end{aligned} \tag{1.40}$$

A similar argument applies for the symmetric wavefunction and the antisymmetric dipole operator.

Since we now know that the symmetric transition dipole operator will only be non-zero with the symmetric wavefunction (and likewise for the antisymmetric transition dipole operator and antisymmetric wavefunction), Eq. (1.31) can be rewritten as:

$$
\begin{aligned}
R^{+} = \frac{1}{\sqrt{2}} \int \pi_{+}^{(1)} M^{+} \psi_0(q;Q)dq \\
\left(\int \sum_{n} \sum_{m} \sum_{p} C^{A}_{n,m,p} \phi_n\left(Q_A\right) \phi_m\left(Q_B\right) \phi_p\left(L\right) \phi_0(Q,L) dQdL \right. \\
\left. + \int \sum_{n} \sum_{m} \sum_{p} C^{B}_{n,m,p} \phi_n\left(Q_A\right) \phi_m\left(Q_B\right) \phi_p\left(L\right) \phi_0(Q,L) dQdL \right)
\end{aligned} \tag{1.41}
$$

Since the final state vibrational wavefunctions are combinations of wavefunctions corresponding to various vibrational modes, $\phi_0(Q,L) = \phi_i(Q_A)\phi_j(Q_B)\phi_k(L)$ where i, j, and k represent the excitation level on A, B, and inter-monomer vibrations respectively. Assuming orthogonality of the vibrational wavefunctions and the parallel mode approximation [30], the expression Eq. (1.41) reduces to

$$
R^{+} = \frac{1}{\sqrt{2}} \int \pi_{+}^{(1)} M^{+} \psi_0(q;Q)dq \left(C^{A}_{i,j,k} + C^{B}_{i,j,k} \right) \tag{1.42}
$$

The transition dipole corresponding to the transition from the antisymmetric electronic state is

$$
R^{-} = \frac{1}{\sqrt{2}} \int \pi_{-}^{(1)} M^{-} \psi_0(q;Q)dq \left(C^{A}_{i,j,k} - C^{B}_{i,j,k} \right) \tag{1.43}
$$

The intensity is proportional to a square of the transition dipole moment. The total spectrum may be obtained by summing the intensities of the peaks corresponding to the symmetric and antisymmetric transitions. Note that transitions in asymmetric bichromophores may have mixed symmetric/antisymmetric character.

1.3 Model Spectra

In this section, general behavior of a model vibronically coupled bichromophore system is considered. In particular, absorption and emission spectra corresponding to different coupling regimes (strong, weak, intermediate), spectra in a presence of two normal modes, spectra of asymmetric chromophores, i.e, chromophores with different vibrational frequencies or displacements of a normal mode, and spectra of inter-monomer modes are discussed. In all figures in this section, transitions through the

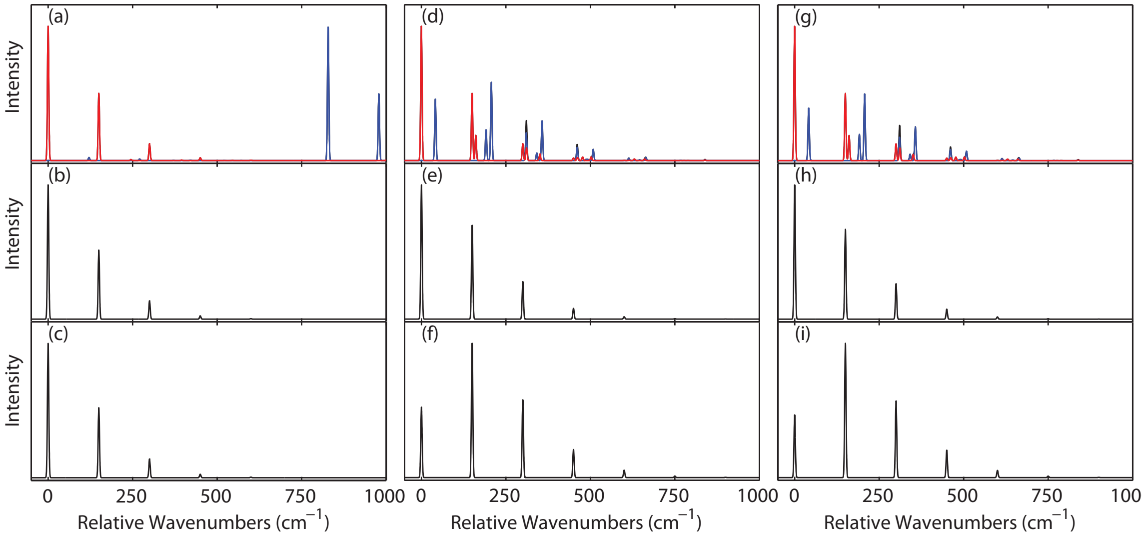

Figure 1.2. Simulations of intra-monomer vibrations in different coupling regimes. $\omega_A = \omega_B = 150\,\mathrm{cm}^{-1}$, $b_A = b_B = 1.0$. The first row is absorption, the second row is S_1 emission, and the third row is S_2 emission. In frames (a)-(c) the electronic coupling $V_{AB} = 400\,\mathrm{cm}^{-1}$ places a vibration in the strong coupling limit. S_2 origin is found at $2{*}V_{AB} = 800\mathrm{cm}^{-1}$. In frames (d)-(f) the same vibration is in the weak coupling limit with $V_{AB} = 60$. The S_2 origin appears at $49.0\,\mathrm{cm}^{-1}$ that is in good agreement with the perturbation theory result of $44.1\,\mathrm{cm}^{-1}$. The discrepancy is because with $p = 0.4$ the case is approaching the intermediate coupling regime. Frames (g)-(i) have $V_{AB} = 400\,\mathrm{cm}^{-1}$ and an additional vibration with parameters $\omega_{2A} = \omega_{2B} = 5000\,\mathrm{cm}^{-1}$, $b_{2A} = b_{2B} = 1.3774$. Formally, the low-frequency mode is in the strong coupling regime, while the high-frequency mode is weakly coupled. However, the high-frequency mode quenches the S_2 state, effectively changing the coupling regime of the low-frequency mode from strong to weak coupling. The displacement parameter b of the high frequency mode was chosen to quench the coupling constant so that it would mimic the weak coupling case of one vibration shown in (d)-(f).

antisymmetric TDM are shown in red while transitions through the symmetric TDM are shown in blue.

Left column (frames (a)-(c)) of Fig. (1.2) show absorption and emission spectra of a vibration in the strong coupling regime ($p >> 1$, Eq. (1.23)), where electronic $S_1 - S_2$ coupling is much larger than the frequency of the vibration. In this case the

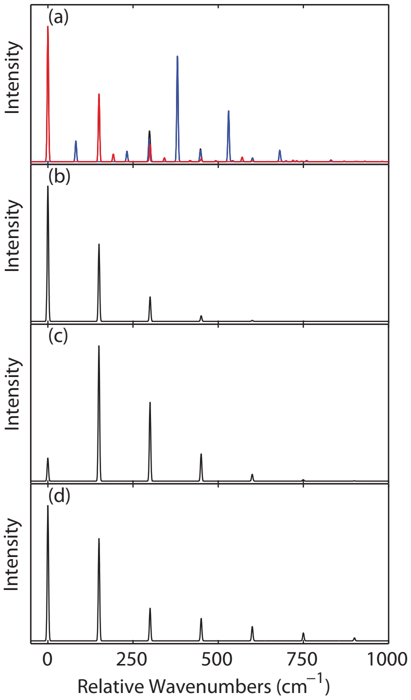

Figure 1.3. Model spectra of one intra-monomer vibrational mode in intermediate coupling limit. $\omega_A = \omega_B = 150\,\mathrm{cm}^{-1}$, $b_A = b_B = 1.0$, $V_{AB} = 150\,\mathrm{cm}^{-1}$. (a) Absorption, (b) emission from the S_1 origin, (c) emission from the state at $82.1\,\mathrm{cm}^{-1}$, and (d) emission from the state at $380.2\,\mathrm{cm}^{-1}$. The emission spectrum from the lower state resembles emission from S_2 in weak coupling limit; the emission spectrum from the higher state resembles emission from S_2 in strong coupling limit.

spectra closely resemble unperturbed spectra with a Frank-Condon (FC) progression off both the S_1 and S_2 origins. In the week coupling limit (frames (d)-(f) of Fig. (1.2)), the vibrational frequency is larger than the coupling between the electronic states. In this case the S_2 state is quenched by a factor of $exp(-b/2)$ for each weakly coupled mode as derived from perturbation theory (see Section (1.4)). Apart from the decreased (quenched) splitting between S_1 and S_2, the origin in the S_2 emission spectrum becomes less intense. This feature will be clearly observed in vibronic spectra of DPM, discussed in Sec. (1.6). The right column of Fig. (1.2) (frames (g)-(i)) show a case when two vibrational modes are present simultaneously. The parameters for the lower-frequency vibration are identical to those used for the strong coupling regime (frames (a), (b), and (c)). The second vibration with very high frequency is in the weak coupling limit. This weakly-coupled mode quenches the S_2 state and effectively lowers the electronic coupling for the first vibration, placing it in the weak-coupling limit as well. Indeed, parameters of the high-frequency mode were chosen such that the resulting absorption and emission spectra for the low-frequency mode are near perfect replicas of the spectra provided in (d)-(f). This example shows that for the normal modes with very different frequencies, the only effect of a high frequency mode on a low frequency mode is through the quenching of the electronic coupling constant of the latter.

Fig. (1.3) shows the spectra corresponding to the intermediate coupling regime, $p \simeq 1$, i.e., when the electronic coupling and vibrational mode frequency are of similar values. The S_2 state is redistributed over several irregularly spaced peaks with varying intensity, for example, one could argue that the S_2 origin is located at either $82.1\,\mathrm{cm}^{-1}$ or $380.2\,\mathrm{cm}^{-1}$. The emission spectra from $82.1\,\mathrm{cm}^{-1}$ band resembles that of a weakly coupled case while the emission from $380.2\,\mathrm{cm}^{-1}$ looks like the vibration is strongly coupled. Thus, it is very hard or impossible to unambiguously assign the S_2 origin in the intermediate coupling regime.

Various effects of asymmetry in intra-monomer vibrational modes are illustrated in Figs. (1.4)-(1.6). The asymmetry of the vibrational mode is controlled by parameter δ,

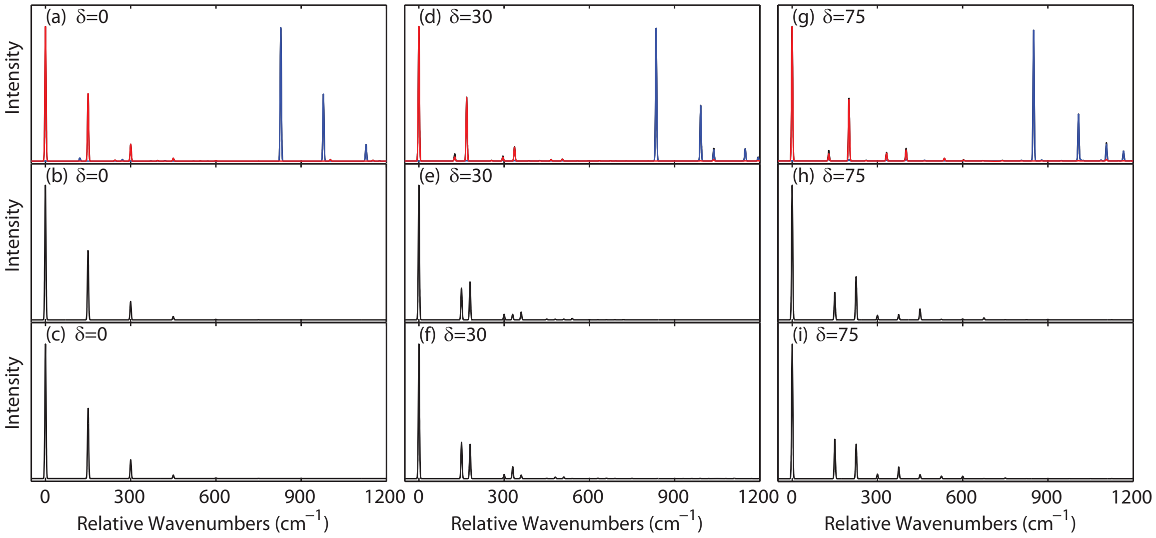

Figure 1.4. Model spectra of one intra-monomer vibrational mode in strong coupling regime with different frequencies on either monomer. $\omega_A = 150\,\mathrm{cm}^{-1}$, $\omega_B = 150 + \delta\,\mathrm{cm}^{-1}$, $b_A = b_B = 1.0$, $V_{AB} = 400\,\mathrm{cm}^{-1}$. The first row is absorption, the second row is S_1 emission, and the third row is S_2 emission. $\delta = 0$ in (a)-(c); $\delta = 30\,\mathrm{cm}^{-1}$ in (d)-(f); $\delta = 75\,\mathrm{cm}^{-1}$ in (g)-(i). As δ is increased, the asymmetry between the modes becomes more pronounced.

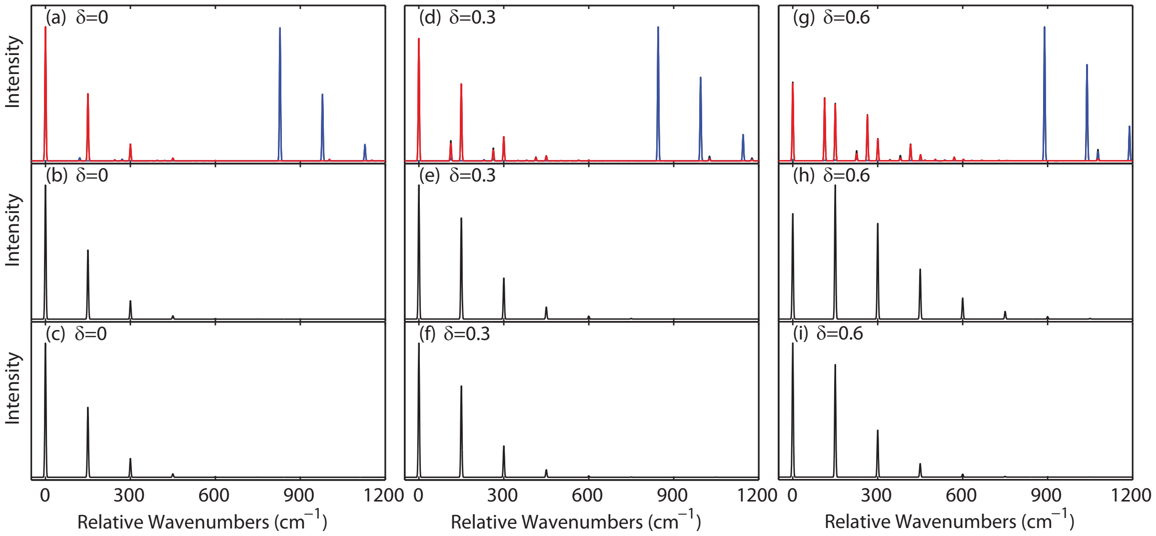

Figure 1.5. Model spectra of one intra-monomer vibrational mode in strong coupling regime with different displacements on either monomer. $\omega_A = \omega_B = 150$ cm^{-1}, $b_A = 1.0$, $b_B = 1.0 + \delta$, $V_{AB} = 400$ cm^{-1}. The first row is absorption, the second row is S$_1$ emission, and the third row is S$_2$ emission. $\delta = 0$ in (a)-(c); $\delta = 0.3$ in (d)-(f); $\delta = 0.6$ in (g)-(i). As δ is increased, the asymmetry between the modes becomes more pronounced.

with $\delta = 0$ corresponding to a symmetric vibration, i.e., vibration that is identical on monomers A and B. Fig. (1.4) shows a case when vibrational modes on monomers have different frequencies. The interesting effect arising due to this asymmetry is splitting of the vibrational peaks in the absorption spectrum. Interestingly, the progression off the S$_1$ state favors the higher energy vibration while the progression off the S$_2$ state favors the lower energy one. The picture does not change when the symmetries of S$_1$ and S$_2$ states are switched: the lowest state exhibits the more intense progression in a high-frequency vibration. Splittings of the vibrational peaks are also observed in the corresponding emission spectra, but intensities of the split lines are almost equal.

A different case of asymmetry arises when the vibrational modes on the monomers have different displacements between the ground and excited state. Such asymmetries are expected to occur in deuterated molecules because deuteration changes the normal mode vectors, and thus the displacements to the excited state geometry. Model spec-

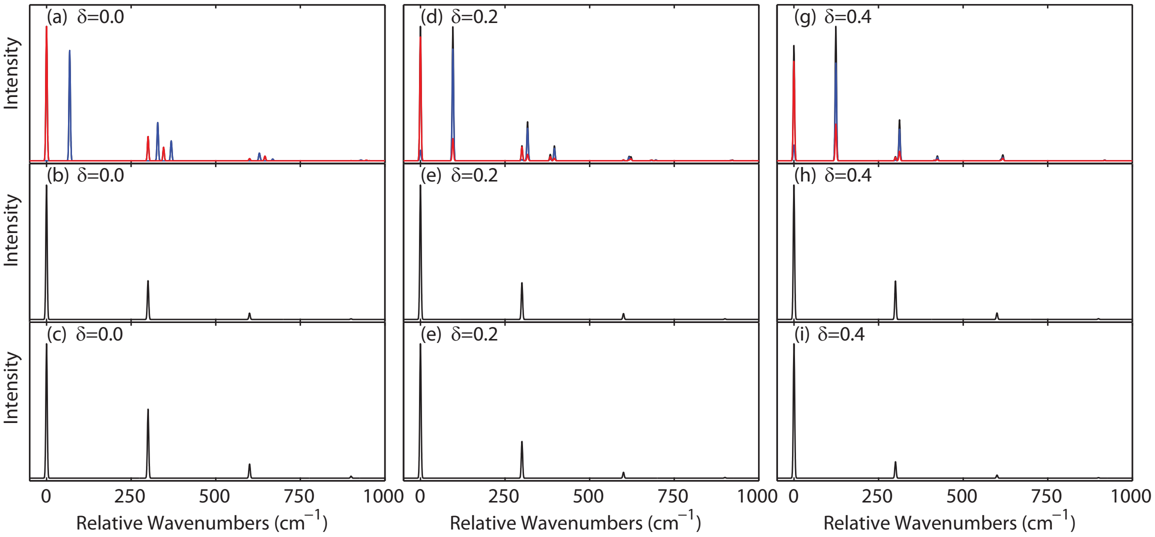

Figure 1.6. Model spectra of one intra-monomer vibrational mode in weak coupling regime with different displacements on either monomer. $\omega_A = \omega_B = 300\ \mathrm{cm}^{-1}$, $b_A = 0.6$, $b_B = 0.6 - \delta$, $V_{AB} = 50\ \mathrm{cm}^{-1}$. The first row is absorption, the second row is S_1 emission, and the third row is S_2 emission. $\delta = 0$ in (a)-(c); $\delta = 0.2$ in (d)-(f); $\delta = 0.4$ in (g)-(i). As δ is increased, the asymmetry between the modes becomes more pronounced.

tra corresponding to the mode in strong coupling regime are reported in Fig. (1.5). Despite the fact that the frequencies of the two vibrations are identical, the absorption spectrum shows energy splittings in the FC progressions both off S_1 and S_2 origins. Similarly to the case of the asymmetric frequencies, the lower-frequency peak has lower intensity off S_1 and higher intensity off S_2. However, unlike the case with asymmetric frequencies, the intensity of the S_1 origin and S_1 band is depleted suggesting that the vibration with higher b value is coupled to the S_1 state. Differently from the case of asymmetric vibrational frequencies, no splitting is present in the emission spectra because the emission levels are governed by the ground state frequencies.

In the previous example (Fig. (1.5)), the vibration is in the strong coupling limit. In Fig. (1.6), the vibrational mode with asymmetric displacements is placed in the weak coupling regime. In this case, the asymmetry is manifested in mixing of S_1 and S_2 progressions, i.e., as the asymmetry is increased, each peak in the absorption

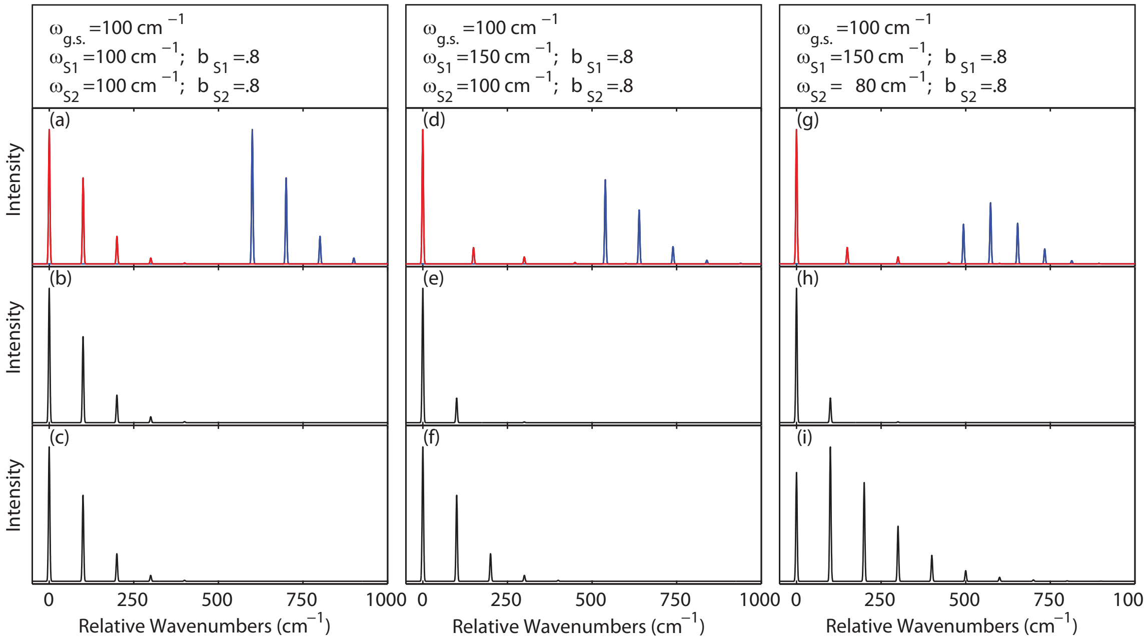

Figure 1.7. Model spectra of one inter-monomer vibrational mode with different frequencies in the ground and first and second excited states of the dimer. $V_{AB} = 300\ \mathrm{cm}^{-1}$, $b_{\mathrm{S}_1} = b_{\mathrm{S}_2} = 0.8$ in all spectra. $\omega_{\mathrm{S}_0} = \omega_{\mathrm{S}_1} = \omega_{\mathrm{S}_2} = 100\ \mathrm{cm}^{-1}$ in (a)-(c); $\omega_{\mathrm{S}_0} = 100\ \mathrm{cm}^{-1}$, $\omega_{\mathrm{S}_1} = 150\,\mathrm{cm}^{-1}$, $\omega_{\mathrm{S}_2} = 100\,\mathrm{cm}^{-1}$ in (d)-(f); $\omega_{\mathrm{S}_0} = 100\,\mathrm{cm}^{-1}$, $\omega_{\mathrm{S}_1} = 150\,\mathrm{cm}^{-1}$, $\omega_{\mathrm{S}_2} = 80\,\mathrm{cm}^{-1}$ in (g)-(i). The first row is absorption, the second row is S_1 emission, and the third row is S_2 emission. Changing the frequency of one state does not change the spacing between frequency levels for the other state.

spectrum has a mixture of the symmetric and antisymmetric character. The peak corresponding to the S_2 origin gains intensity while the higher vibrational energy levels in the S_2 emission spectrum are reduced in intensity. Another interesting effect observed in these spectra is the increase of the splitting between the S_1 and S_2 origins upon increasing asymmetry between the modes.

Finally, the properties of the inter-monomer vibrations are examined. In the considered examples, the S_1 state is antisymmetric and S_2 is symmetric. As discussed above, the inter-monomer vibrations may have different displacement and frequency parameters for the first and second excited states of a bichromophore. In the first series of spectra, shown in Fig. (1.7), the effect of changing an excited state frequency

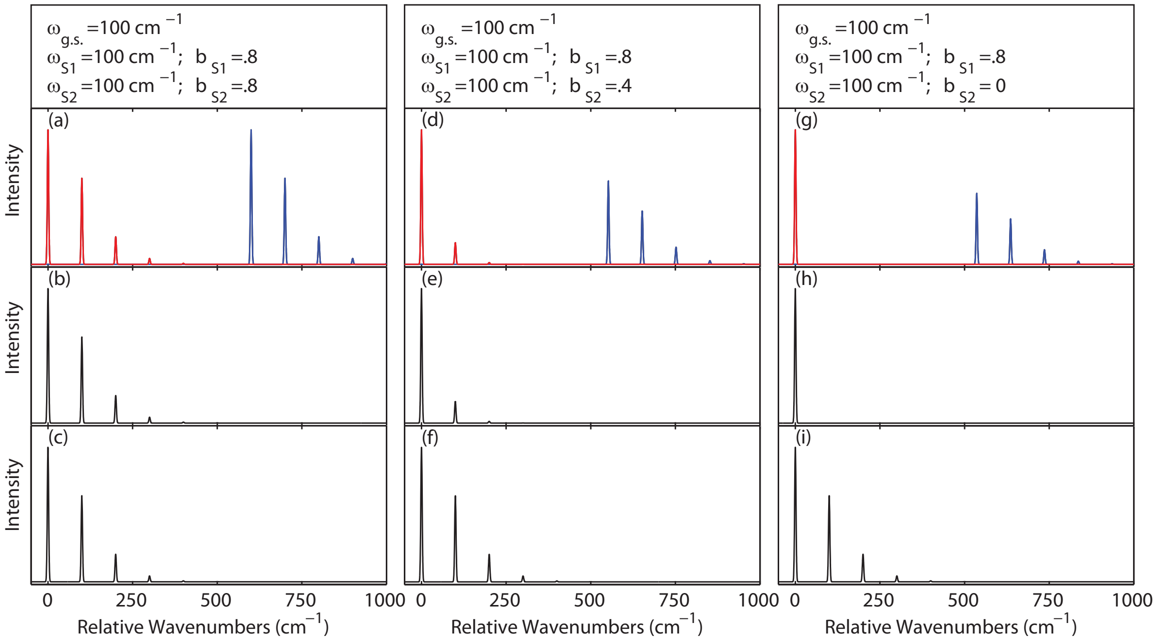

Figure 1.8. Model spectra of one inter-monomer vibrational mode with different displacement parameters for the S_1 and S_2 states of the dimer. $V_{AB} = 300\ \mathrm{cm}^{-1}$, $\omega_{\mathrm{S}_0} = \omega_{\mathrm{S}_1} = \omega_{\mathrm{S}_2} = 100\ \mathrm{cm}^{-1}$ in all spectra. $b_{\mathrm{S}_1} = b_{\mathrm{S}_2} = 0.8$ in (a)-(c); $b_{\mathrm{S}_1} = 0.4$, $b_{\mathrm{S}_2} = 0.8$ in (d)-(f); $b_{\mathrm{S}_1} = 0.0$, $b_{\mathrm{S}_2} = 0.8$ in (g)-(i). The first row is absorption, the second row is S_1 emission, and the third row is S_2 emission. Changing the displacement for one state allows to suppress the Frank-Condon progression on this state while keeping it on the other.

is investigated. As demonstrated in Fig. (1.7), changing the S_1 frequency for an inter-monomer mode results in corresponding change in the vibrational progression off the S_1 origin, while maintaining the same vibrational pattern for the progression off the S_2 state. Both the S_1 and S_2 emission spectra retain the same vibrational spacing because these progressions are dictated by the ground state vibrational states which are independent of whether the molecule was in the S_1 or S_2 excited states.

The effect of different displacements between the $S_1 - S_0$ and $S_2 - S_0$ states (b_{S_1} and b_{S_2} parameters, respectively) is investigated in Fig. (1.8). When the b_{S_1} displacement is decreased, the FC progression off the S_1 origin in absorption and emission is depleted, while the S_2 bands remain unaffected. Similar effects are observed in the spectra of diphenylmethane, analyzed in Fig. (1.6). In those spectra, the low frequency inter-monomer vibrations T and $\bar{\mathrm{T}}$ appear in the S_1 but not S_2 florescence spectra.

1.4 Perturbation Theory For the Strong and Weak Coupling Limits

As was shown in Fig. (1.2), there is almost no effect on the splitting between the S_1 and S_2 energy levels by a strongly coupled mode, yet weakly coupled modes cause the splitting between the S_1 and S_2 states to decrease by a factor of $exp(-b^2/2)$. This section applies perturbation theory to illustrate why there is no quenching in the strongly coupled case and derive the exponential factor in the weakly coupled case. In the strong coupling limit the linear displacement terms (l_A, l_B) can be set to zero. This assumption allows the Hamiltonian (Eq. (1.15)) of the system to be solved analytically and the linear displacement terms re-introduced as a perturbation. In the weak coupling limit, the electronic coupling term V_{AB} can be set to zero allowing for the analytic solution of the system Hamiltonian. By re-introducing V_{AB} by perturbation theory, it will be demonstrated that the vibronic quenching of the electronic energy levels originates from vibrational overlap integrals.

1.4.1 Strong Coupling

Starting with the intra-mode molecular Hamiltonian in Eq. (1.15) and setting displacement terms l_A and l_B terms to zero causes the upper left and lower right matrix elements to become:

$$\frac{P_A^2}{2M} + \frac{1}{2}M\omega_A^2 Q_A^2 + \frac{P_B^2}{2M} + \frac{1}{2}M\omega_B^2 Q_B^2 \tag{1.44}$$

Since the diagonal matrix elements are those of a harmonic oscillator, the stationary states of these vibronic Hamiltonians are known:

$$\left(\frac{P_A^2}{2m} + \frac{1}{2}m\omega_A^2 Q_A^2\right)\phi_0\left(Q_A\right) = E_A\phi_0\left(Q_A\right) \tag{1.45}$$

The eigenfunctions of the total Hamiltonian will be the symmetric and anti-symmetric combinations of the eigenfunctions of Hamiltonian from Eq. (1.45)

$$\left\{\begin{pmatrix} \phi_0\left(Q_A\right)\phi_0\left(Q_B\right) \\ \phi_0\left(Q_A\right)\phi_0\left(Q_B\right) \end{pmatrix}, \begin{pmatrix} \phi_0\left(Q_A\right)\phi_0\left(Q_B\right) \\ -\phi_0\left(Q_A\right)\phi_0\left(Q_B\right) \end{pmatrix}\right\} \tag{1.46}$$

with eigenvalues of $E^+ = E_A + E_B + V_{AB}$ and $E^- = E_A + E_B - V_{AB}$, respectively.

The perturbation to this system provided by displacement along the normal modes is:

$$H' = \begin{pmatrix} l_A Q_A & 0 \\ 0 & l_B Q_B \end{pmatrix} \tag{1.47}$$

The first order corrections to the energies, given in Eq. (1.48), are zero as the integrands are anti-symmetric:

$$\begin{aligned} E_1^+ &= l_A\langle\phi_0(Q_A)\left|Q_A\right|\phi_0(Q_A)\rangle\langle\phi_0(Q_B)|\phi_0(Q_B)\rangle \\ &\quad + l_B\langle\phi_0(Q_A)|\phi_0(Q_A)\rangle\langle\phi_0(Q_B)\left|Q_B\right|\phi_0(Q_B)\rangle = 0 \\ E_1^- &= l_A\langle\phi_0(Q_A)\left|Q_A\right|\phi_0(Q_A)\rangle\langle\phi_0(Q_B)|\phi_0(Q_B)\rangle \\ &\quad - l_B\langle\phi_0(Q_A)|\phi_0(Q_A)\rangle\langle\phi_0(Q_B)\left|Q_B\right|\phi_0(Q_B)\rangle = 0 \end{aligned} \tag{1.48}$$

To compute the second order perturbation energies E_2^+ and E_2^-, higher order vibrational wavefunctions should be introduced. The wavefunctions have the same form as the eigenfunctions for the ground vibrational state:

$$\begin{aligned} E_2^+ &= \frac{\left|l_A\langle\phi_0(Q_A)\left|Q_A\right|\phi_1(Q_A)\rangle\right|^2}{E_0 - E_1} + \frac{\left|l_B\langle\phi_0(Q_B)\left|Q_B\right|\phi_1(Q_B)\rangle\right|^2}{E_0 - E_1} \\ &= \frac{-l_A^2}{2m\omega_A} + \frac{-l_B^2}{2m\omega_B} = -b_A^2\hbar\omega_A - b_B^2\hbar\omega_B \\ E_2^- &= \frac{\left|l_A\langle\phi_0(Q_A)\left|Q_A\right|\phi_1(Q_A)\rangle\right|^2}{E_0 - E_1} + \frac{\left|l_B\langle\phi_0(Q_B)\left|Q_B\right|\phi_1(Q_B)\rangle\right|^2}{E_0 - E_1} \\ &= \frac{-l_A^2}{2m\omega_A} + \frac{-l_B^2}{2m\omega_B} = -b_A^2\hbar\omega_A - b_B^2\hbar\omega_B \end{aligned} \tag{1.49}$$

Thus, to the second order in perturbation theory, the vibrational excitations in the strong coupling limit do not affect the splitting between the electronic states $\Delta E = E^+ - E^-$ and their intensities.

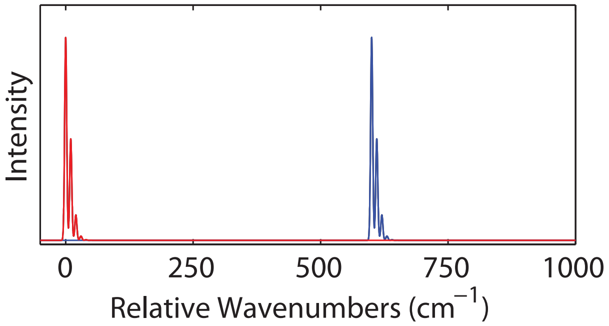

Figure 1.9. Model spectrum of a intra-monomer mode with the following parameters: $V_{AB} = 300$ cm^{-1}, $\omega_A = \omega_B = 10$ cm^{-1}, and $b_A = b_B = 1.0$. Numerically obtained $\mathrm{S}_1 - \mathrm{S}_2$ splitting of 600.17 cm^{-1} agrees very well with the second order perturbation theory result of 600 cm^{-1}.

Let us consider a system with $V_{AB} = 300\text{cm}^{-1}$, $\omega_A = \omega_B = 10\text{cm}^{-1}$, and $b_A = b_B = 1.0$. This set of parameters puts the system in the strong coupling regime. From the second order perturbation theory, the expected energy of the S$_2$ state would appear 600 cm^{-1} above the energy of the S$_1$ state. The simulation returns a spectrum with S$_1 - S_2$ splitting of 600.17 cm^{-1}, in good agreement with the results of perturbation theory (see Fig. (1.9)).

1.4.2 Weak Coupling

Starting with the system Hamiltonian from (Eq. (1.15)), set the electronic coupling term, V_{AB}, to zero so the matrix becomes diagonal. Define the eigenfunctions of the vibrational Hamiltonian as

$$\left(\frac{P_A^2}{2m} + l_A Q_A + \frac{1}{2} m\omega_A^2 Q_A^2\right)\phi_0^*\left(Q_A\right) = E_A^* \phi_0^*\left(Q_A\right) \tag{1.50}$$
$$\left(\frac{P_A^2}{2m} + \frac{1}{2} m\omega_A^2 Q_A^2\right)\phi_0\left(Q_A\right) = E_A \phi_0\left(Q_A\right)$$

where ϕ_0^* is the wavefunction for the ground vibrational state under the potential of the electronic excited state and ϕ_0 is the wavefunction for the ground vibrational state in the ground electronic state. Since the electronic excited state Hamiltonian is a shifted harmonic oscillator potential, the excited state wavefunction can be related to the ground state wavefunction through Eq. (1.51) (assuming the frequency is unchanged between ground and excited states):

$$\phi_0^*(Q_A) = \phi_0\left(Q_A + \frac{l_A}{m\omega_A^2}\right) \tag{1.51}$$

The eigenvectors of the system Hamiltonian are the eigenfunctions of the diagonal matrix elements:

$$\left\{\begin{pmatrix} \phi_A^*\left(Q_A\right)\phi_B\left(Q_B\right) \\ 0 \end{pmatrix}, \begin{pmatrix} 0 \\ \phi_A\left(Q_A\right)\phi_B^*\left(Q_B\right) \end{pmatrix}\right\} \tag{1.52}$$

with eigenvalues of $E_A^* + E_B$ and $E_A + E_B^*$, respectively.

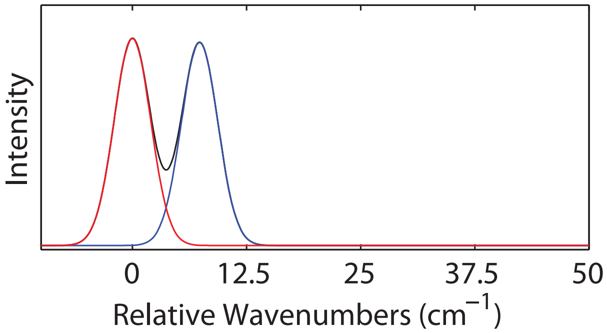

Figure 1.10. Model spectrum of a intra-monomer mode with the following parameters: $V_{AB} = 10$ cm^{-1}, $\omega_A = \omega_B = 1000$ cm^{-1}, and $b_A = b_B = 1.0$. Numerically obtained $\mathrm{S}_1 - \mathrm{S}_2$ splitting of 7.357 cm^{-1} agrees very well with the perturbation theory result of 7.358 cm^{-1}.

The electronic coupling term can be re-introduced using perturbation theory as the coupling between the two electronic states

$$H' = \begin{pmatrix} 0 & V_{AB} \\ V_{AB} & 0 \end{pmatrix} \tag{1.53}$$

In the case of $E_A^* + E_B = E_A + E_B^*$, the two eigenvectors are degenerate before the application of the perturbation. Applying degenerate perturbation theory, the following perturbation matrix is obtained:

$$W = \begin{pmatrix} \langle \phi_0^*(Q_A)\phi_0(Q_B)\,|0|\,\phi_0^*(Q_A)\phi_0(Q_B)\rangle & \langle \phi_0^*(Q_A)\phi_0(Q_B)\,|V_{AB}|\,\phi_0(Q_A)\phi_0^*(Q_B)\rangle \\ \langle \phi_0(Q_A)\phi_0^*(Q_B)\,|V_{AB}|\,\phi_0^*(Q_A)\phi_0(Q_B)\rangle & \langle \phi_0(Q_A)\phi_0^*(Q_B)\,|0|\,\phi_0(Q_A)\phi_0^*(Q_B)\rangle \end{pmatrix} \tag{1.54}$$

$$= V_{AB} \begin{pmatrix} 0 & \langle \phi_0^*(Q_A)|\phi_0(Q_A)\rangle\langle \phi_0(Q_B)|\phi_0^*(Q_B)\rangle \\ \langle \phi_0(Q_A)|\phi_0^*(Q_A)\rangle\langle \phi_0^*(Q_B)|\phi_0(Q_B)\rangle & 0 \end{pmatrix} \tag{1.55}$$

The overlap integrals can be calculated using Eq. (1.51) resulting in:

$$\langle \phi_0^*(Q_A)|\phi_0(Q_A)\rangle = e^{\frac{-l_A^2}{4m\omega_A^3\hbar}} = e^{\frac{-b_A^2}{2}} \tag{1.56}$$

The eigenvalues of the perturbation matrix W are $-V_{AB}e^{\frac{-b_A^2}{2}}e^{\frac{-b_B^2}{2}}$ and $V_{AB}e^{\frac{-b_A^2}{2}}e^{\frac{-b_B^2}{2}}$, resulting in a $\mathrm{S}_1 - \mathrm{S}_2$ splitting of $2V_{AB}e^{\frac{-b_A^2}{2}}e^{\frac{-b_B^2}{2}}$. Thus, in the weak coupling limit, the

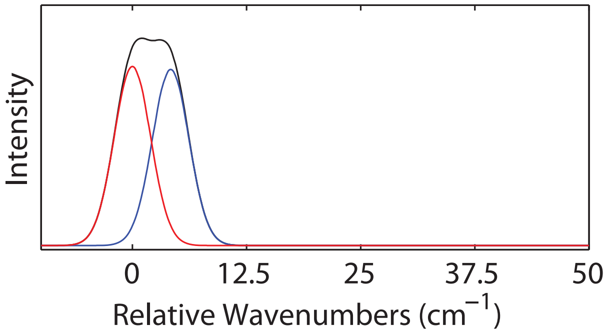

Figure 1.11. Model spectrum of two intra-monomer modes with the following parameters: $V_{AB} = 10$ cm^{-1}, $\omega_{1A} = \omega_{1B} = 1000$ cm^{-1}, $\omega_{2A} = \omega_{2B} = 2000$ cm^{-1}, $b_{1A} = b_{1B} = 1.0$, and $b_{2A} = b_{2B} = .75$. Numerically obtained $\mathrm{S}_1 - \mathrm{S}_2$ splitting of 4.192 cm^{-1} agrees with the perturbation theory result of 4.192 cm^{-1}.

splitting between the electronic states is decreased (quenched) by vibrational overlap integrals.

Let us consider a system in the weak coupling regime with $V_{AB} = 10\,\mathrm{cm}^{-1}$, $\omega_A = \omega_B = 1000\,\mathrm{cm}^{-1}$, and $b_A = b_B = 1.0$. A numerical simulation on this system results in a spectrum shown in Fig. (1.10) and a $\mathrm{S}_1 - \mathrm{S}_2$ splitting of 7.357 cm^{-1}. This is in excellent agreement with the perturbation theory splitting of 7.358 cm^{-1}. In case of two vibrational modes, shown in Fig. (1.11), the quenching factor is a product of the vibrational overlap integrals. The numerically calculated spectrum produces a splitting of $4.192\,\mathrm{cm}^{-1}$ which is again in excellent agreement with the perturbation theory result of $4.192\,\mathrm{cm}^{-1}$.

1.5 Convergence With Respect to the Vibrational Basis Set

Before commencing with the modeling of DPM, it is important to demonstraight convergence of the exact numerical solution with regard to basis set size and displacement parameter b. Since the computation of the electronically excited eigenstates essentially assumes describing a harmonic oscillator wavefunction with a displaced basis, larger displacement b requires more basis functions for an accurate description of the

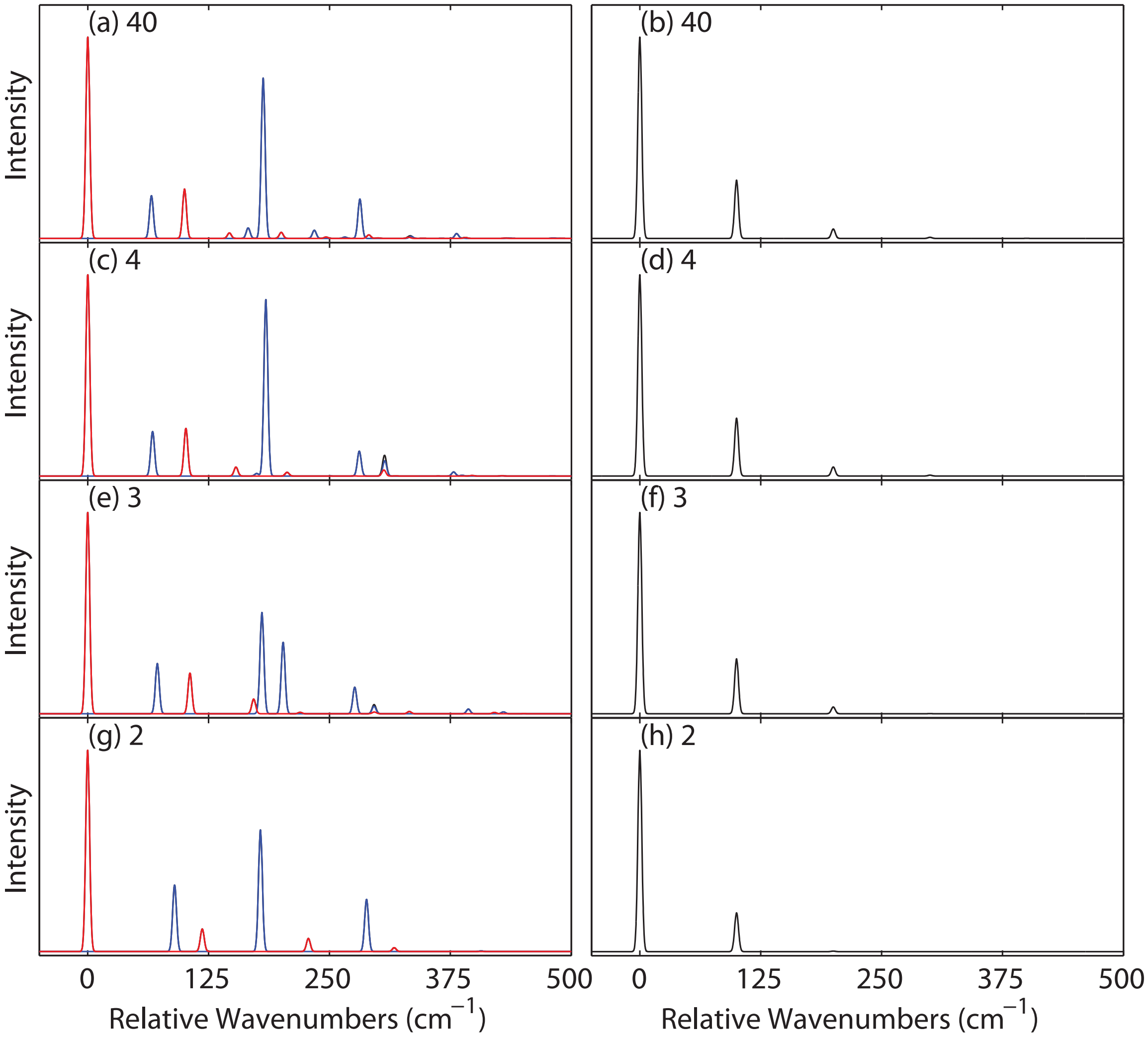

Figure 1.12. Model spectra showing the convergence of the numerical solution with respect to the number of vibrational basis functions. Absorption spectra are in the left panel and emission spectra from the S_1 state are in the right panel. The number of vibrational basis functions used is given in the frame label. The frequency of the vibrational mode is $100\,\mathrm{cm}^{-1}$, $b = 0.7$, and the coupling constant $V_{AB} = 75\,\mathrm{cm}^{-1}$, setting the vibration in the intermediate regime. This sequence shows that four basis functions are required to converge the entire absorption spectra and three basis functions are needed for convergence of the emission spectra from the first excited state.

wavefunction. Thus, we intentionally chose a b value bigger than spectroscopically realistic values to find the minimum number of functions required for convergence. It is important to note that it is more difficult to converge the absorption spectra (which requires all the spectroscopically significant eigenstates to be converged) than the $S_1 \rightarrow S_0$ florescence spectra (which only requires the lowest energy excited state to be converged). Though to converge other emission spectra more basis functions will be required. For high frequency intra-monomer vibrations with relatively small b values, a smaller number of basis functions may be used because only the first vibrational excited state will play a significant role in the spectra. For lower frequency inter-monomer vibrations, enough basis functions must be included to converge the entire absorption spectra. As shown in Fig. (1.12), for $b = .7$, four basis functions per vibrational mode are required to converge the entire absorption spectrum and only three basis functions to converge the ground state.

1.6 Modeling Vibronic Spectrum of Diphenylmethane

In this section the extended FG model is applied to simulate vibronic spectra of the bichromophore diphenylmethane (DPM). High-resolution absorption and emission spectra of the first two singlet excited states of DPM have been measured by Zwier and co-workers [26] and we will follow the same notations on labeling DPM vibrational modes.

1.6.1 Computational Details

In order to perform the Fulton-Gouterman simulation, vibrational frequencies and displacement parameters for each vibration as well as an electronic coupling term and relative transition dipole moments of S_1 and S_2 are required as input. The parameters for intra-monomer modes were obtained from density functional theory (DFT) and time-dependent density functional theory (TD-DFT) calculations on toluene which is considered a "monomer" of diphenylmethane. The ground and first excited state

Table 1.1.

Intra-monomer vibrational parameters for diphenylmethane found from B3LYP/cc-pVTZ calculations on toluene.

Assignment	expt. ω^1(cm^{-1})	calc. ω (cm^{-1})	b	p	quenching factor^2
$6a_1^0$	554	530	.26	3.4	simulated
$6b_1^0$	622	639	.43	1.1	simulated
11_1^0	749	748	.05	68	1.0
1_1^0	822	801	.65	.36	simulated
12_1^0	1006	1023	.73	.23	.81
$18a_1^0$	1035	1054	.39	.77	.97
$9a_1^0$	1204	1206	.43	.54	.89
$19b_1^0$	1447	1535	.02	129	1.0

[1] DPM experimental frequencies from the Zwier group. [26]

[2] Quenching factors used to compute the effective electronic coupling as in Eq. (1.57) for modes not directly included in the simulation ("simulated"). The product of all quenching factors $\prod_{i=1}^{N} e^{-b_i^2}$ is .48.

geometries of toluene were optimized with B3LYP functional [31–33] in the cc-pVTZ basis set [34] with the Q-Chem electronic structure package. [35] Vibrational frequencies of the ground state of toluene were obtained at the same level of theory. ezSpectrum software [36] was used to find the displacements between the ground and first excited state geometries in the basis of the ground state vibrational vectors. These displacements were converted into b parameters; the normal modes with the largest b parameters and corresponding p values (Eq. (1.23)) are listed in Table (1.1).

To obtain the parameters for the inter-monomer modes (as pictured in Fig. (1.13), one needs to perform *ab-initio* structure calculations on the S_0, S_1, and S_2 states of the dimer (DPM). The parameters obtained from DFT and TD-DFT B3LYP/cc-pVTZ computations are summarized in Table (1.2). The experimental spectra of

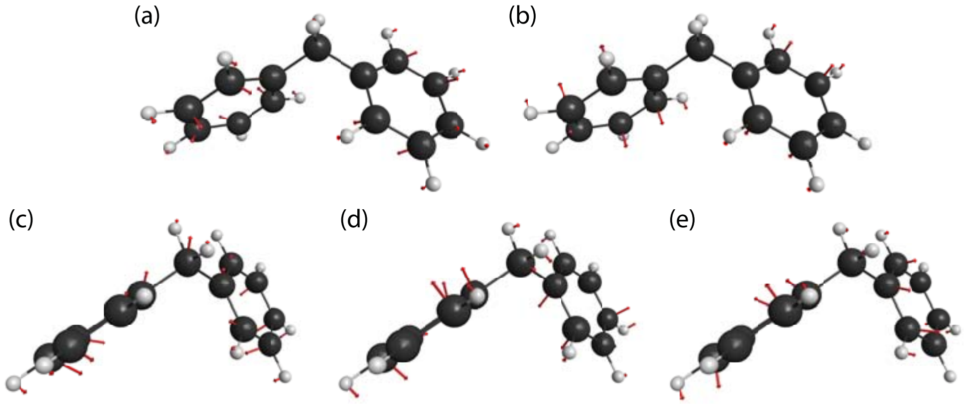

Figure 1.13. Inter-monomer vibrational modes of DPM: a) anti-symmetric torsion $\bar{\mathrm{T}}$, b) symmetric torsion T, c) butterfly mode β, d) anti-symmetric libration $\bar{\mathrm{R}}$, and e) symmetric libration R.

DPM reveal progressions along five low-frequency inter-monomer modes: symmetric and antisymmetric torsions T and $\bar{\mathrm{T}}$, symmetric and antisymmetric R and $\bar{\mathrm{R}}$ modes, and the butterfly mode β. From those, parameters of R and $\bar{\mathrm{R}}$ were computed in a standard way, i.e., S_0, S_1, and S_2 states of DPM were optimized (the constrained optimization with fixed values of torsional angle corresponding to the T mode was employed for S_2), then the displacements between the ground and the first and second excited state geometries were found in the basis of the ground state vibrations.

Due to an anharmonic nature of the other three modes and extreme sensitivity of their parameters to the level of theory employed, their parameters were obtained from potential energy surface (PES) calculations. Namely, potential energy slices were constructed along normal mode vectors of each mode starting from the S_1 state geometry and employing $.002\,\text{Å}\sqrt{amu}$ displacement increments in either direction of the vibrational vector. TD-DFT B3LYP/cc-pVTZ calculations were performed to find energies of S_1 and S_2 states at each of these geometries. For each vibration, the S_1 and S_2 energies were fit to parabolas, from which frequency and displacement parameters were extracted. As an example, plots of the energies and parabolic fits for the T mode are shown in Fig. (1.14). However, while this procedure improved agreement between experimental and calculated values of the low-frequency modes compared to the direct calculation of Hessians of the S_1 and S_2 states, it still resulted in overestimated frequencies for all modes and strongly overestimated displacement for the β mode. It should be noted, however, that the β mode is governed by an interplay of covalent and non-covalent, in particular dispersion, interactions between the aromatic rings, and as such is extremely sensitive to the level of theory.

In order to improve the agreement with the experimental spectra, some of the parameters for inter-monomer modes were adjusted. The butterfly mode β that reveals very little intensity in the experimental spectra, was excluded from modeling. The resulting set of inter-monomer parameters is presented in Table (1.3).

Vertical splittings between the first and second electronic excited states of DPM were computed by a number of electronic structure methods, including TD-DFT with

Table 1.2.

Inter-monomer vibrational parameters as found from B3LYP/cc-pVTZ calculations on S_0, S_1, and S_2 states of diphenylmethane.

Assignment	ω_{S_0} (cm^{-1})	ω_{S_1} (cm^{-1})	ω_{S_2} (cm^{-1})	b_{S_1}	b_{S_2}
$\bar{\mathrm{T}}$	22.5	38.3	—[1]	-.02	-.06
T	38.5	47.9	35.2	.60	.60
β	68.1	62.0	67.5	-1.0	1.2
$\bar{\mathrm{R}}$	191	192	105	0.0	0.0
R	225	202	157	-.62	-.08

[1] No real-value frequency could be obtained.

Table 1.3.

Adjusted (fitted to experimental spectra) inter-monomer vibrational parameters. Ab-inito values were kept where appropriate.

Assignment	ω_{S_0} (cm^{-1})	ω_{S_1} (cm^{-1})	ω_{S_2} (cm^{-1})	b_{S_1}	b_{S_2}
$\bar{\mathrm{T}}$	10.0	23.0	10.0	-.02	-.06
T	20.0	28.3	20.0	1.40	0.0
$\bar{\mathrm{R}}$	191	275	105	0.0	0.0
R	225	285	188	-.55	-.08

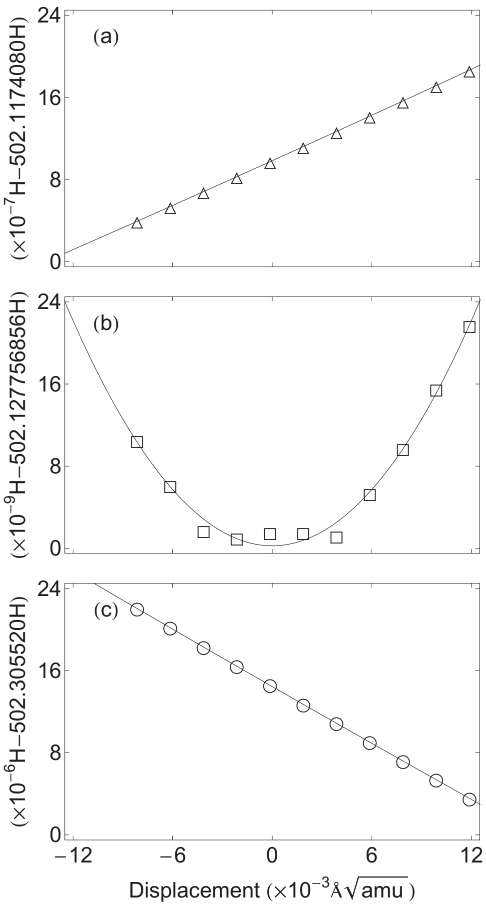

Figure 1.14. Potential energy surfaces of the symmetric torsion T mode in (a) the second excited state, (b) the first excited state, and (c) the ground state. The abscissa is the displacement from the optimized S_1 geometry. Energy scales in frames (a), (b), and (c) are different because near the S_1 minimum, the PES of the S_1 state is dominated by second order effects while PESs of the other two states are dominated by first order effects.

Table 1.4.
Vertical $S_1 - S_2$ splittings computed at the ground state optimized geometry.

level of theory	$S_1 - S_2$ splitting (cm^{-1})
EOM-CCSD/cc-pVDZ	430
ωB97X-D/cc-pVTZ	549
BP86/cc-pVTZ	539
B3LYP/cc-pVTZ	1069

[1] MP2/cc-pVTZ ground state geometry was used in these calculations.

various functionals (B3LYP, BP86 [37, 38], and long-range and dispersion corrected ωB97X-D [39]), and equation-of-motion coupled cluster with single and double excitations method [40–43] (EOM-CCSD) (see Table (1.4)). Apparently, the value of splitting is sensitive to the level of theory, with the best estimates provided by EOM-CCSD and TD-DFT with ωB97X-D. This results in the electronic coupling, taken as a half of the splitting, in the range of $215 - 275\,\text{cm}^{-1}$. Including quenching factor due to high-frequency (weakly-coupled) vibrational modes not explicitly included in the simulation (see Table (1.1)) results in the effective electronic coupling:

$$V_{AB}^{eff} = V_{AB} \prod_{i=1}^{N} e^{\frac{-b_{A,i}^2}{2}} e^{\frac{-b_{B,i}^2}{2}} = V_{AB} \prod_{i=1}^{N} e^{-b_i^2} \tag{1.57}$$

where $b_{A,i}$ and $b_{B,i}$ are displacements for the i'th mode on monomer A and B, respectively. In the symmetric case, as in DPM, $b_{A,i} = b_{B,i}$. Using the parameters in Table (1.1), this results in an effective coupling in the range of $103 - 132\,\text{cm}^{-1}$. The coupling constant used for modeling DPM spectra was taken as $155.8\,\text{cm}^{-1}$. All simulated peaks were modeled by gaussians with a standard deviation of $1\,\text{cm}^{-1}$.

1.6.2 DPM Spectra

Using simulated parameters for intra-monomer vibrational modes (Table (1.1)), partly fitted parameters for inter-monomer vibrational modes (Table (1.3)), and effective coupling constant $V_{AB} = 155.8\,\mathrm{cm}^{-1}$, theoretical spectra for DPM were computed as shown in Fig. (1.15). Comparison of the experimental and theoretical low-frequency absorption spectra (Fig. (1.15a)) shows a quantitative agreement both in peak positions and intensities. In particularly, one can clearly recognize a progression along the torsional mode T, with peaks at 27, 54, and 81 cm^{-1}. The peak at 43 cm^{-1} is the second vibrational state of $\bar{\mathrm{T}}$ (i.e., $\bar{\mathrm{T}}^2$), while the first vibrational quanta is not present. This is because the intensity in the $\bar{\mathrm{T}}$ mode is originated due to a frequency change rather than a displacement between the electronic states. Therefore, only even quanta of this mode gain non-zero intensity. As follows from decomposition of the absorption spectrum into symmetric and antisymmetric components (Fig. (1.15b)), the origin of the second excited state appears at about 123 cm^{-1}, in agreement with experimental assignment. The intensity of S_2 origin is well reproduced by a $\mathrm{S}_1/\mathrm{S}_2$ TDM ratio of 2.08 : 1, which is in close agreement with the 1.98 : 1 ratio computed at the ωB97X-D/cc-pVTZ level of theory.

Analysis of the emission spectrum from the S_1 origin (Fig. (1.15c)) shows that the peak at 63 cm^{-1}, missing in the simulated spectrum, is due to the β mode that was excluded from simulations, as mentioned above. Another inter-monomer vibration, R, reveals itself in an intense line at 221 cm^{-1}. This peak is well reproduced by the ab-initio computations, with only a minor correction in the displacement parameter. All intra-monomer modes, $6\mathrm{a}^0_1$, $6\mathrm{b}^0_1$, and 1^0_1, are reasonably well described by ab-initio calculations, with frequency discrepancies not exceeding 30 cm^{-1}. The 11^1_0 vibration with frequency $748\,\mathrm{cm}^{-1}$ was not included in the calculation due to a lack of intensity in the S_2 emission spectrum (Fig. (1.15d)). There is also a nice agreement between theory and experiment in the high-frequency peaks due to inter-monomer vibrations in the emission spectrum of the S_2 origin (Fig. (1.15d)). It is very encouraging that the model spectrum accurately predicts the change in intensity of vibronic bands in the S_1 and S_2 emission spectra, even though there is no parameter that directly controls that intensity ratio.

The obviously missing part of the modeled S_2 emission spectrum is the so called 'clump' emission around $100\,\mathrm{cm}^{-1}$. As proposed by Zwier and co-workers, these bands are not vibronic progressions off the S_2 state but emissions from the S_1 vibrational bands that gain their intensity due to the energetic proximity to the S_2 origin. [26] [LVS: check this!] Indeed, the simulation produces two vibronic S_1 states (with very low intensity) within $\pm 5\,\mathrm{cm}^{-1}$ of the S_2 origin. We mimicked the "clump" emission spectrum by producing emission spectra from these two vibronic states and adding them in equal proportions, and fitting the intensity of the combined spectra to the experimental "clump" emission. The resulting spectrum is provided in Fig. (1.16). The modeled "clump" spectrum qualitatively reproduces the experimental emission in the region $0 - 200\,\mathrm{cm}^{-1}$, with a low-intensity region from $0 - 80\,\mathrm{cm}^{-1}$ followed by a clump of peaks. Thus, our results are in accord with assignments suggested by Zwier. [26]

1.7 Modeling Vibronic Spectrum of d_5-diphenylmethane

The asymmetric vibronic coupling model developed and applied to DPM-d_0 above is applied to DPM-d_5 here. The model spectra are compared to high-resolution absorption and emission spectra of the first two singlet excited states of DPM-d_5 taken under jet-cooled conditions. [44] The notations for DPM-d_5 vibrational modes follow notations from Zwier and co-workers. [26, 45] The only significant change from the previously reported DPM-d_0 modeling is the increased electronic coupling constant to compensate for the additional quenching caused by the frequency changes. It is reassuring, though, that the updated electronic coupling constant is closer to the coupling obtained from the excited state calculations on the DPM-d_0 bichromophore.

For modeling vibronic spectra of DPM-d_5, vibrational frequencies and displacement parameters between the ground and first excited states are required for both

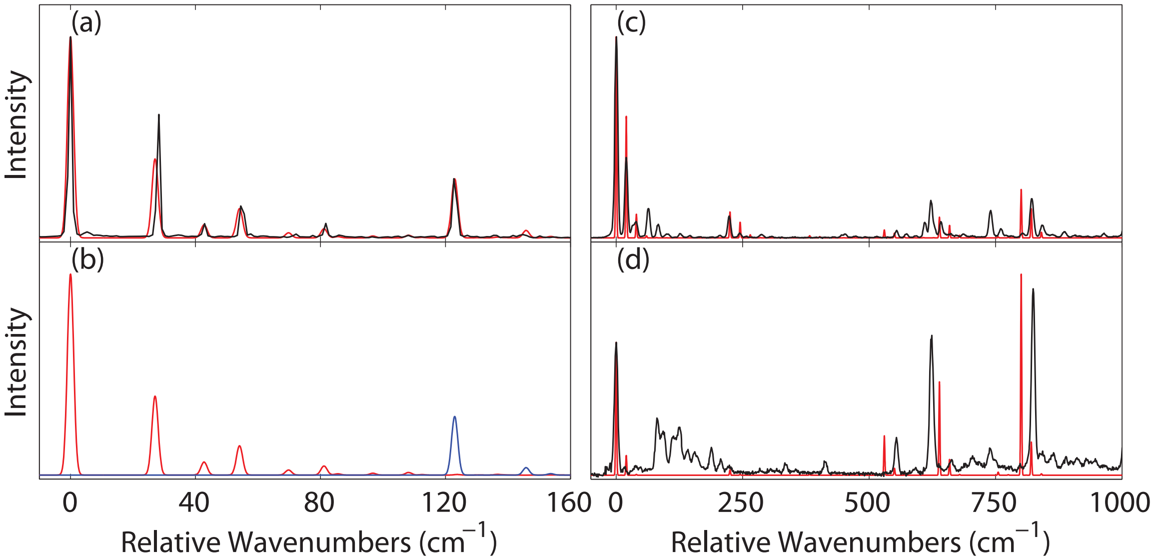

Figure 1.15. DPM spectra produced from parameters in Tables (1.1) and (1.3) with an electronic coupling constant of 155.8 cm^{-1}. Comparison of the calculated (red) and experimental (black) absorption spectra are shown in (a). Breakdown of the calculated spectrum by the electronic state, with the red trace representing the S_1 (antisymmetric) state and the blue trace representing the S_2 (symmetric) state are in (b). (c) and (d) provide comparisons of the calculated (red) and experimental (black) emission spectra from the S_1 and S_2 origins, respectively.

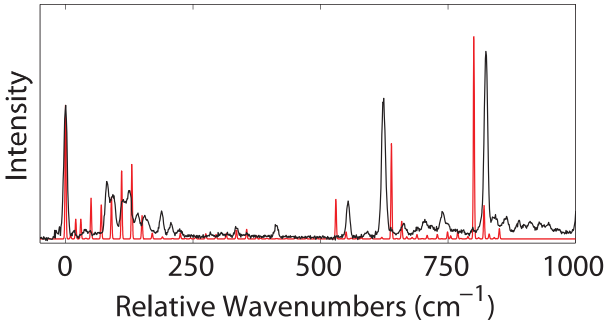

Figure 1.16. S_2 "clump" emission spectra. The calculated spectrum (in red) is produced by adding S_2 emission spectrum as in Fig. (1.15d) with emissions from energetically close S_1 vibrational states. Experiential spectrum is in black.

Table 1.5.

Intra-monomer vibrational parameters for DPM-d_5 as found from B3LYP/cc-pVTZ calculations on toluene and toluene-d_5. Assignment of vibrational modes follows Varsanyi notations for modes of benzene.

Assignment	Calc. $\omega(\mathrm{cm}^{-1})$	Calc. $\omega^*(\mathrm{cm}^{-1})$	b	P	Quenching Factor	Basis Functions
$6\mathrm{a}^0_1$	518	492	0.23	3.8	Simulated	3
11^0_1	558	361	0.03	49	1.0	—
$6\mathrm{b}^0_b$	612	606	0.36	1.49	Simulated	3
$18\mathrm{a}^0_1$	749	673	0.35	0.87	Simulated	4
1^0_1	758	539	0.08	7.1	Simulated	3
$19\mathrm{b}^0_1$	862	841	0.17	4.7	0.99	—
$9\mathrm{a}^0_1$	888	774	0.53	0.28	0.87	—
12^0_1	980	955	0.66	0.26	0.80	—

the deuterated and non-deuterated monomers, i.e., toluene and toluene-d_5 molecules. For consistency with the previously modeled spectra of DPM-d_0, we enforced that vibrations corresponding to the non-deuterated monomer retain the same parameters as were used in the DPM-d_0 simulations. The parameters for toluene-d_5 and toluene were obtained using density functional theory (DFT) and time dependent (TD) DFT calculations at the B3LYP [31–33]/cc-pVTZ [34] level in the Q-Chem electronic structure package. [35]

EzSpectrum software [36] was used to compute displacements between the ground and excited state geometries of the monomers in the basis of the ground state normal mode vectors. These displacements are converted into b parameters as prescribed in Eq. 1.22. [45] The results from these calculations for the partially deuterated monomer are listed in Table 1.5 along with results for non-deuterated toluene in Table 1.1.

As follows from Table 1.5, calculations show a large number of vibronically active normal modes, i.e., the modes with b values of 0.2 and higher. Due to steep exponential scaling of the algorithm, the present implementation of the vibronic coupling model is limited to simultaneous modeling of 10-15 vibrations, depending on the size of the basis set. Note that vibrations on two monomers are counted as separate modes. Thus, we limited our modeling to the lowest active vibrations of DPM-d_5 as they are distinct in experimental spectra. Additionally, the closer the vibrational frequency is to the value of the electronic coupling, the worse the quenching factor approximation will capture the effects of the vibration on the second excited state. On the other hand, density of vibronic states increases in higher-frequency region, making the assignment and comparison less ambiguous. Combining these considerations, we opted to include all active vibrations with frequencies below 800 cm^{-1}. Interestingly, the asymmetric model does not require inclusion of pairs of identical modes on both monomers. For example, we included mode 18a on toluene-d_5 but not on toluene-d_0, as its frequency in toluene-d_0 exceeds 800 cm^{-1} cut-off.

In addition to the monomer vibrational frequencies and displacements, the inter-monomer vibrational frequencies and displacements are also required for modeling vibronic spectra of DPM-d_5. The inter-monomer parameters for DPM-d_5 (shown in Table 1.6) were obtained analogously to the parameters of DPM-d_0. [26] Similarly to DPM-d_0, five important low-frequency inter-monomer vibrations were found for DPM-d_5, namely: symmetric and antisymmetric torsions T and $\bar{\mathrm{T}}$, symmetric and antisymmetric vibrations R and $\bar{\mathrm{R}}$, and the butterfly mode β. Normal mode vectors of these vibrations are shown in Fig. 1.17.

Inter-monomer vibrations depend on non-covalent interactions between monomers such as dispersion forces that are not well reproduced by many electronic structure methods, including B3LYP functional used in this work. Additional complexity arises due to anharmonicity of these low-frequency modes. As a result, parameters of inter-monomer modes obtained from electronic structure calculations resulted in a poor fit to experiment. Therefore, it was necessary to fit these parameters to experiment

Table 1.6.

Inter-monomer vibrational parameters as found from B3LYP/cc-PVTZ calculations on S_0, S_1, and S_2 states of DPM-d_5.

Assignment	ω_{S_0} ($\omega_{g.s.}$) (cm^{-1})	ω_{S_1} (ω_-) (cm^{-1})	ω_{S_2} (ω_+) (cm^{-1})	b_{S_1} b_-	b_{S_2} b_+
$\bar{T}$	22	37	—	-0.12	-0.23
T	37	46	36	0.61	0.62
β	66	60	58	-1.03	0.95
$\bar{R}$	184	184	61	-0.12	0.00
R	218	196	151	-0.62	-0.08

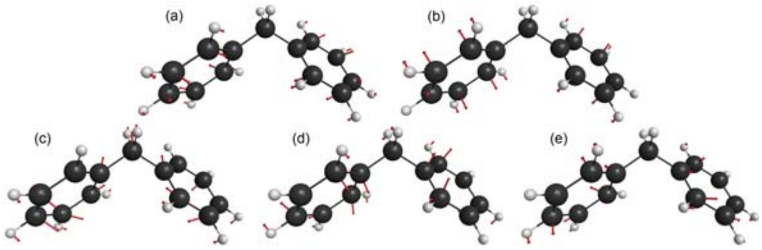

Figure 1.17. First five inter-monomer vibrational modes of DPM-d_5: a) anti-symmetric torsion $\bar{T}$, b) symmetric torsion T, c) butterfly mode β, d) anti-symmetric libration $\bar{R}$, and e) symmetric libration R. These are very similar to the inter-monomer modes observed in DPM.

Table 1.7.

Adjusted (fitted to experimental spectra) inter-monomer vibrational parameters for DPM-d_5.

Assignment	ω_{S_0} ($\omega_{g.s.}$) (cm^{-1})	ω_{S_1} (ω_-) (cm^{-1})	ω_{S_2} (ω_+) (cm^{-1})	b_{S_1} b_-	b_{S_2} b_+	Basis Functions
$\bar{\mathrm{T}}$	18	21	15	0.09	0.00	8
T	23.5	25	28	1.10	0.00	8
$\bar{\mathrm{R}}$	176	160	100	0.01	0.21	4
R	215	200	193	0.34	0.01	4

(similarly to the approach used for modeling DPM-d_0). The fitted parameters of the inter-monomer modes are shown in Table 1.7. The strongest disagreement is observed for the butterfly β mode. In the experimental spectra, β mode shows very little activity, while electronic structure calculations indicate a large displacement factor upon excitation. A failure of electronic structure calculations in describing accurate displacement along this mode in in accord with the observation that the ground state equilibrium value of the valence angle between two benzene rings (Phe-C-Phe), related to the butterfly mode, is very sensitive to the level of theory. Specifically, correlated methods accounting for dispersion interactions such as MP2 and CCSD provide more compact geometries with smaller values of this angle (111°). On the other hand, Kohn-Sham functionals, which often underestimate dispersion forces, show more open structures with larger angle values (113°-114°) and larger distances between the two rings. As even the ground state frequency of β mode is not well reproduced by electronic structure calculations, it is not surprising that subtle changes in geometry due to electronic excitation are not properly captured. Therefore, parameters for β mode had to be fitted to reproduce experimental spectra, which suggest that this mode is barely active. As such, and taking into account considerations of computational cost, the butterfly mode was excluded from simulations.

The method used to calculate the vertical energy splitting between the first and second excited states is unchanged from that used for DPM-d_0. Specifically, equation of motion coupled cluster (EOM-CC) and TD-DFT calculations of the S_1-S_2 splitting in DPM-d_0 were performed (see Table 1.4). The quenching factor due to vibrational modes not included in the simulation is nearly identical between the deuterated and non-deuterated monomers, changing from .479 for DPM-d_0 to .475 to DPM-d_5. Thus, the electronic structure simulations predict a similar range for the effective coupling parameter of 106 cm^{-1} to 137 cm^{-1}. An effective coupling constant of 143 cm^{-1} is used to model DPM-d_0 spectra, while the effective coupling of 110 cm^{-1} is used in the simulations of DPM-d_5. The decrease in the coupling constant in case of DPM-d_5 can be rationalized by change in the ZPVE between the two monomers. Since the ZPVE-corrected excitation energy of the deuterated monomer is slightly different from that of the non-deuterated monomer, the two electronic states interact less strongly resulting in a reduced coupling constant in case of DPM-d_5.

The difference in excitation energies between the non-deuterated and deuterated monomers due to the vibrational modes not included in the simulation can be obtained from the ground and excited state frequency calculations of the two monomers. After applying Eq. 1.24 to the ground and excited state frequencies of toluene and toluene-d_5, a $\Delta\Delta ZPVE$ splitting of -255 cm^{-1} was found. Since ZPVE of either toluene or toluene-d_5 is on the order of 25,000 cm^{-1}, this parameter is obtained by taking sums and differences of large numbers and has large numerical uncertainty. Namely, since this parameter is the sum of 156 individual frequencies, an average error of only one wavenumber in each frequency could easily produce a total error of nearly 200 cm^{-1}. Thus, it is hard to accurately obtain this parameter from electronic structure calculations. It was found that the splitting of -50 cm^{-1} provides a better agreement with experimental spectra; thus, the latter value was used in the spectra presented below.

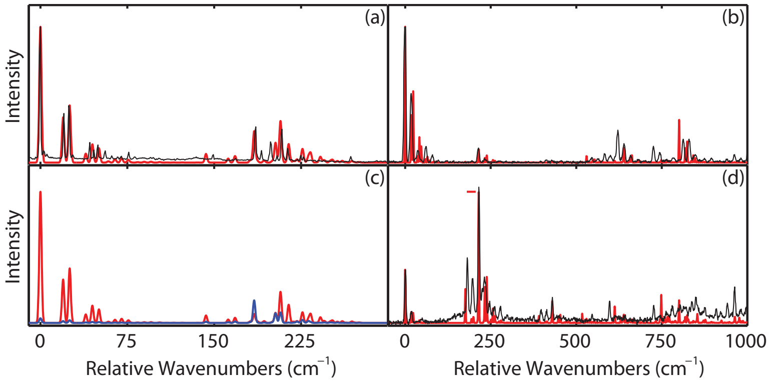

Figure 1.18. (a) Absorption spectrum of DPM-d$_5$ compared to experiment. The black trace is experiment; simulated absorbance is broken down by state, where red is S$_1$ and blue is S$_2$. (b) Experimental (black) and computed (red) S$_1$ emission spectrum. (c) Experimental (black) and computed (red) S$_2$ emission spectrum, where the horizontal dash indicates the height of the computed 215 cm^{-1} peak.

1.7.1 Absorption and Emission Spectra

Using simulated parameters for intra-monomer modes on the non-deuterated and deuterated monomers (Tables 1.5 and 1.1), partly fitted parameters for the inter-monomer modes (Table 1.7), an effective coupling constant $V_{AB} = 110\,\mathrm{cm}^{-1}$, and a ZPVE splitting of $\delta\delta ZPVE = -50\,\mathrm{cm}^{-1}$, vibronic spectra for DPM-d$_5$ were calculated. Comparisons of theoretical and experimental absorption and emission spectra are shown in Fig. 1.18. The agreement between the theoretical and experimental spectra is truly remarkable. In the absorption spectrum, the intensity of nearly every peak is reproduced to within 20% accuracy. The position, intensity and composition of the suspected S2 state at 186 cm^{-1} is replicated nearly exactly. Even the vibrational band structure off the S$_2$ peak is accurately reproduced.

Agreement for the S$_1$ emission is worse than for the other two spectra, but is still quite good. While the peak heights are all very well reproduced in the high-frequency region of the spectra, they are less accurately reproduced for the low-frequency intra-monomer modes. The theory also does not reproduce doubling the peaks in many intra-monomer modes. The origin of the doubling is most likely in purely mechanical coupling between the normal modes of the two monomers over the methyl bridge. However, the present vibronic coupling model does not include terms responsible for vibrational coupling of the monomers.

The most remarkable agreement of the three spectra, though, is the S_2 emission spectra. Just as with the DPM-d_0 S_2 emission spectra (see Fig. 1.15), a clump emission is observed. In case of DPM-d_0, the clump emission was originated in higher-order coupling of vibrational levels off the S_1 state with the S_2 origin. In the original modeling of DPM-d_0 above, the clump emission was mimicked (Fig. 1.16) by artificially increasing the intensity of the vibronic bands off the S_1 state near the S_2 origin. In case of DPM-d_5, however, fundamental R and $\bar{\mathrm{R}}$ vibrations off S_1 are located near the origin of the S_2 state. Coupling between R/$\bar{\mathrm{R}}$ fundamentals and S_2 origin produces a tremendous intensity around 215 cm^{-1} in the S_2 emission spectrum with no continued Franck-Condon progression. The theory replicates peaks in the clump emission at 176, 215, 233 and 238 cm^{-1}, only missing the peak at 180 cm^{-1}. The experimental S_2 emission spectrum is also correctly replicated in the 400 to 700 cm^{-1} region. Past 700 cm^{-1}, the density of states becomes large and the multitude of peaks creates an elevated baseline (in the region from 750 to 850 cm^{-1}). As no intra-monomer modes are included in the calculation past 850 cm^{-1}, the spectra cannot be expected to be accurate past this point.

The model also provides wave function composition (i.e., vibronic mixing) and transition dipole moment (TDM) directions for specific vibronic peaks, which can be compared with TDMs obtained from rotational band contour analysis. Table 1.8 summarizes this information for several selected bands. While the S_1 origin in symmetric DPM-d_0 is of a:c type (i.e., TDM is oriented along x and z directions) and the S_2 origin is mainly of b type (TDM is along y direction), the S_1 and S_2 states become mixed in DPM-d_5. This is a manifestation of the asymmetry of the vibronic wave function with respect to the deuterated and undeuterated monomers. It is very encouraging that both the rotational band contour analysis and the model

Table 1.8.

Wavefunctions and squared TDM components in percent of various excited state peaks. $\mathrm{S}_1/\mathrm{S}_2$ refers to the electronic state of the given product basis function. The remaining characters indicate the number of vibrational quanta in the given mode. Vibrational basis functions that are not listed are in the ground vibrational state.

Frequency (cm^{-1})	Wavefunction Composition	Exp. TDM %			Comp. TDM %		
		X	Y	Z	X	Y	Z
0.0	$0.42\,\lvert\mathrm{S}_1\rangle - 0.25\,\lvert\mathrm{S}_1\mathrm{T}_1\rangle - 0.30\,\lvert\mathrm{S}_1\bar{\mathrm{T}}_1\rangle$	66	03	31	72	04	25
19.6	$0.24\,\lvert\mathrm{S}_1\rangle + 0.28\,\lvert\mathrm{S}_1\mathrm{T}_1\rangle - 0.29\,\lvert\mathrm{S}_1\mathrm{T}_2\rangle$	57	07	36	71	05	25
25.2	$-0.27\,\lvert\mathrm{S}_1\rangle - 0.22\,\lvert\mathrm{S}_1\bar{\mathrm{T}}_1\rangle + 0.33\,\lvert\mathrm{S}_1\bar{\mathrm{T}}_2\rangle$	63	03	34	70	05	24
184.5	$-0.32\,\lvert\mathrm{S}_1\mathrm{R}_1\rangle - 0.36\,\lvert\mathrm{S}_2\rangle + 0.17\,\lvert\mathrm{S}_2\bar{\mathrm{T}}_1\rangle$	30	50	20	19	74	07
193.0	$-0.23\,\lvert\mathrm{S}_1\bar{\mathrm{T}}_1\bar{\mathrm{R}}_1\rangle + 0.31\,\lvert\mathrm{S}_1\bar{\mathrm{T}}_3\bar{\mathrm{R}}_1\rangle$ $-0.16\,\lvert\mathrm{S}_1\mathrm{T}_1\bar{\mathrm{T}}_3\bar{\mathrm{R}}_1\rangle$	—	—	—	61	18	21
203.0	$0.24\,\lvert\mathrm{S}_1\mathrm{T}_1\mathrm{R}_1\rangle + 0.24\,\lvert\mathrm{S}_2\rangle + 0.23\,\lvert\mathrm{S}_2\mathrm{T}_1\rangle$	—	—	—	36	52	12
207.2	$0.28\,\lvert\mathrm{S}_1\bar{\mathrm{T}}_1\mathrm{R}_1\rangle + 0.24\,\lvert\mathrm{S}_2\rangle - 0.21\,\lvert\mathrm{S}_2\mathrm{T}_1\rangle$	—	—	—	54	28	19
214.3	$0.31\,\lvert\mathrm{S}_1\mathrm{R}_1\rangle + 0.28\,\lvert\mathrm{S}_2\bar{\mathrm{T}}_1\rangle - 0.18\,\lvert\mathrm{S}_2\bar{\mathrm{T}}_2\rangle$	—	—	—	73	02	25

agree on partial delocalization of the S_1 and S_2 state origins (0.0 cm^{-1} and 184.5 cm^{-1}, respectively).

The model faithfully reproduces the TDM directions and delocalization of the S_1origin and low-frequency bands off S_1. Delocalization of the S_2 origin is less accurately described by the model because delocalization of S_2 originates both from mixing with R and $\bar{R}$ bands off S_1 and from higher-order coupling with T and $\bar{T}$ states off S_1. As the higher-order coupling is not accounted for by the model, the model only partially captures delocalization of the S_2 origin. However, even coupling with R/$\bar{R}$ bands results in a very mixed nature of the S_2 origin with a significant contribution from the S_1-originated bands.

Qualitative explanation of partial delocalization of the S2 state is provided below.

1.7.2 Qualitative Description of S_1 State

While in some ways the effects of deuteration of one ring on the spectroscopy and excited state vibronic mixing in DPM-d_5 are rather modest, in other ways they are strikingly obvious, and a bit puzzling. As already pointed out, the appearance of such a strong S_0-S_1 $\bar{T}^1_0$ fundamental in the DPM-d_5 excitation spectrum (Fig. 1.18) is in striking contrast to its forbidden nature in DPM-d_0, even more so because the high resolution UV spectrum has proven that electronic excitation in S_1 is still delocalized over both rings in DPM-d_5. Furthermore, the S_1 origin DFL spectrum (Fig. 1.18) has Franck-Condon activity involving three highly localized ring modes (6b, 12, 9a) that shows a strong asymmetry, in that emission to the ground state vibrational levels involving motion of the h_5-ring is much larger than the corresponding emission to its d_5-ring counterparts. Likewise, the S_2 origin DFL spectrum shows emission involving the same ring modes from the S_2 portion of the excited state wave function favoring the d_5 ring modes.

Localization of the vibrational wave functions occurs due to several effects produced by the asymmetric deuteration of the monomers. The first effect, reproduced by the electronic structure calculations, is the localization of the 6b, 12, and 9a vibrations to the individual aromatic rings. Due to the weak kinematic coupling between the two chromophores in all electronic states, the small mass perturbation causes a rotation of the nuclear wave functions from symmetric/antisymmetric pairs to vibrations localized on individual monomers.

Once the vibrations are localized, an examination of the electronic Hamiltonian reveals that the geometry at which the electronic excitation is perfectly delocalized is no longer the geometry at which both vibrations are displaced from their equilibrium positions by equal amounts. Working in the diabatic electronic basis, the system Hamiltonian can be written (considering only one vibration on each monomer):

$$\begin{pmatrix} \hbar\omega_H \left(Q_H + Q_0\right)^2 + \hbar\omega_D \left(Q_D\right)^2 & V \\ V & \hbar\omega_H \left(Q_H\right)^2 + \hbar\omega_D \left(Q_D + Q_0\right)^2 \end{pmatrix} \tag{1.58}$$

Here Q is a vibrational coordinate for either the deuterated or non-deuterated ring (labeled accordingly), ω is the corresponding localized vibrational frequency, Q_0 is the displacement along a normal mode upon electronic excitation of the corresponding chromophore, and V is an electronic coupling constant. The electronic states become completely delocalized in this model Hamiltonian when the two diagonal elements become equal. However, since $\omega_H > \omega_D$ due to the isotope effect, the electronic states become perfectly mixed when $Q_D > Q_H$ (assuming $Q_0 > 0$). This effect can be observed in the S_1 state potential energy surface in Fig. 1.21. In this figure the color of the surface indicates whether the electronic excitation prefers to localize on the d5-ring (orange) or the h_5-ring (blue). In frame (a) of Fig. 1.21 the parameters are completely symmetric and thus the change from orange to blue happens along $Q_a = Q_b$, while in frame (b) the change happens when $Q_D > Q_H$.

An additional contribution to the localization of the vibrational Franck-Condon activity of the S_1 state on the h_5-ring arises due to differences in zero point energies (ZPEs) of the vibrations not directly included in the vibronic coupling Hamiltonian. Vibrational frequencies in the excited state are on average smaller than those in

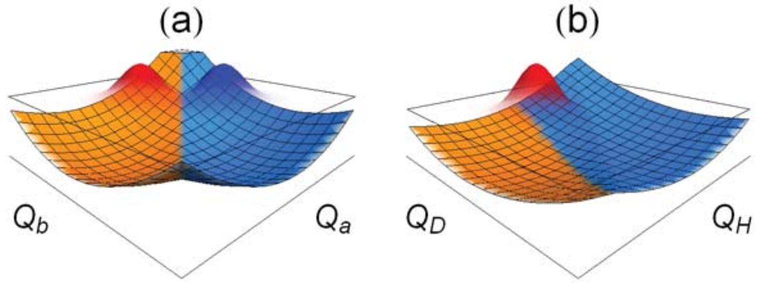

Figure 1.19. The potential energy surface (solid) and wave function (transparent) for two localized vibrations with symmetric parameters (frame (a)), and asymmetric parameters representing a partially deuterated bichromophore (frame (b)). The color of the surface indicates which monomer the excitation prefers to localize on, with blue representing the a/h_5-ring and orange representing the b/d_5-ring.

the ground state due to the reduced bonding character of the excited state. If this reduction in frequency affects both the h_5- and d_5-rings by the same multiplicative factor, the difference in ZPEs between the ground and excited states will cause the diabatic state in which the h_5-ring is excited to be slightly lower in energy than the state in which the d_5-ring is excited. This change in ZPEs can be represented by adding a small energy (approximately an order of magnitude less than the frequency values) to the lower right Hamiltonian element. The effect of this parameter can be observed in frame (b) of Fig. 1.21 by noting that the well with $Q_D < 0$ (right side of PES) is shallower than the well with $Q_H < 0$ (left side of PES). This slight asymmetry in the depth of the two wells causes the S1 state to localize around $Q_H = -Q_0$ and $Q_D = 0$. However, as noted above, this is precisely where the two electronic states are completely mixed from the Hamiltonian in Eq. 1.58. As a result, both the localization of the h_5-ring Frank-Condon activity on the S_1 state and the delocalization of the S_1 electronic state take place.

1.7.3 Qualitative Description of S_2 State

Though the unexpected localization of vibrational levels on the S_1 state can be qualitatively explained with a two-mode model, a more sophisticated three-mode system is needed for the S_2 state, as is discussed in Ref. [46]. Specifically, the model system includes two intra-monomer ring modes located on the h_5- and d_5-rings, respectively, and a single inter-monomer mode with parameters from the R mode in Table 1.7. The only change to the parameters from what was used in the full simulation of DPM-d_5 is the reduction of the electronic coupling constant V_{AB} from 110 cm^{-1} to 100 cm^{-1} to compensate for the reduced amount of vibronic quenching from the intra-monomer modes not included in this simplified model. As follows from the inter-monomer Hamiltonian (Eqs. 1.29 and 1.30), the electronic coupling V_{AB} changes along inter-monomer modes. Dependence of V_{AB} on displacement along mode R is shown in Fig. 1.20. As seen from Fig. 1.20, the dependence of the coupling parameter

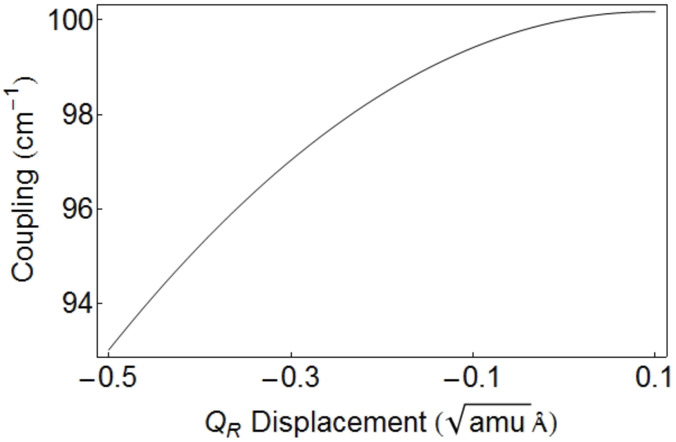

Figure 1.20. Magnitude of off-diagonal coupling parameter as a function of displacement along inter-monomer mode R.

on inter-monomer coordinate is relatively minor, such that harmonic approximation is well justified.

Analysis of experimental spectra suggests that the S_2 state is also mostly delocalized with both the excitation and Franck-Condon activity slightly favoring the d_5-ring. The qualitative explanation of this phenomenon relies on the dependence of the wavefunction on the intra-monomer mode. As shown in Fig. 1.21, while the S_1 wavefunction is similar for all values of Q_R, the S_2 wavefunction changes significantly as a function of Q_R. Due to the shape of the potential energy surface along Q_R, the density localizes near $Q_R = 0$. However, a negative displacement along the Q_R coordinate tends to correlate with localization on the h_5-ring (enhanced blue lobe), while zero to positive displacements along Q_R correlate with localization on d_5-ring (enhanced red lobe). The combination of these effects causes a suppression of the wavefunction when the density is localized on the h_5-ring and an increase in wavefunction magnitude when it is localized on the d_5-ring. Thus, the S_2 state partly localizes on the d_5-ring with most of the Franck-Condon activity occurring on modes located on the d_5-ring side. Yet the small amount of remaining intensity on the h5-ring side, occurring when Q_R is negative, results in rotational band contours which show partly delocalized S_2 state character.

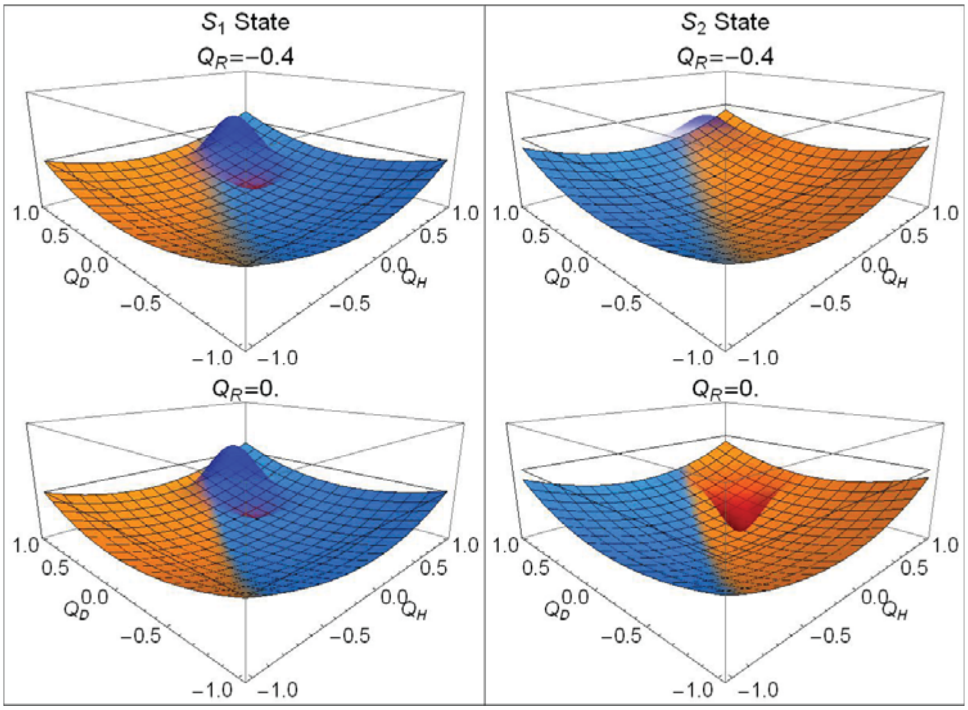

Figure 1.21. Graphical depiction of the wavefunction for the first and second excited singlet states of DPM-d$_5$. Coordinates are mass weighted with units $\sqrt{AMU}$Å. The color of the surface indicates which monomer the excitation prefers to localize on, with blue representing the h$_5$-ring and orange representing the d$_5$-ring. The semi-transparent blue-red surface represents the wavefunction density. The blue lobe of the wavefunction corresponds to an excitation on the h$_5$-ring; the red lobe corresponds to an excitation on the d$_5$-ring.

1.8 Conclusions and Future Simulations

The Fulton-Gouterman model for vibronic coupling in bichrompohores has been extended to treat asymmetric molecules and inter-chromophore vibrational modes. Several vibrational modes can be considered simultaneously by means of Lanczos diagonalization of the sparse Hamiltonian matrix. Considered model spectra provide detailed analysis of the theory, including effects of simultaneous modeling of several modes and effects of asymmetries in different kinds in intra- and inter-monomer vibrations.

Modeling of the vibronic spectra of the DPM bichromophore is a stringent test for performance of the extended FG model. It was found that obtaining accurate parameters for the FG model may be challenging, especially parameters for the low-frequency inter-monomer modes that require computations of optimal geometries and vibrational frequencies of a bichromophore. However, inclusion of the inter-monomer modes is essential for modeling spectra of flexible bichromophores. Using the computed parameters for the intra-monomer modes and partly fit parameters for the inter-monomer modes, the experimental absorption and emission spectra of DPM were successfully reproduced. Additionally, a qualitative modeling of the clump emission spectrum was provided, even though a more rigorous theoretical framework may be needed in order to provide physically meaningful rather than fit representation of this region.

2. VIBRONIC COUPLING IN N-CHROMOPHORE SYSTEMS

Here I will give a brief derivation of the Hamiltonian for the Fulton-Gouterman model extended to N-chromophore systems. This derivation will follow the bichromophore Hamiltonian derivation quite closely, however some complications will arise when considering the inter-monomer mode Hamiltonian and the computation of peak intensities. After the derivation, some model systems are proposed.

2.1 Theory

For an N-chrmophore system composed of N nearly identical chromophores, the system Hamiltonian can be written analogously to Eq. (1.1):

$$H = \sum_{i=1}^{N} \left(H_i + \sum_{j \neq i}^{N} V_{i,j}(L) \right) + T_L \tag{2.1}$$

$V_{i,j}(L)$ is the coupling between chromophores i and j, which is not always the same depending on the configuration of the monomers. T_L is now the momentum for the collection of $6N - 6$ normal modes that result from motions between the chromophores. Just as in the derivation for the bichromophore case, the vibrations will be divided into inter and intra-monomer vibrations. While the intra-monomer vibrations will remain essentially unchanged from the bi-chrmophore case, the inter-monomer vibrational Hamiltonian will see a significant change in form.

2.1.1 Multi-chromophore Intra-monomer Modes

To ease the derivation of the system Hamiltonian, we will work in a monomer localized electronic basis, which will have N functions.

$$\left\{ \pi_i^{(1)} = \psi_1^{\mathrm{el}}\left(q_i; Q_i\right) \prod_{j \neq i}^{N} \psi_0^{\mathrm{el}}\left(q_j; Q_j\right) \right\}_{i=1,2,\ldots N} \tag{2.2}$$

This basis reduces to the dimer basis (Eq. (1.6)) in the case where there is only two chromophores. Just as done in the bichromophore case (Eqs. (1.7) and (1.8)), it is now necessary to evaluate the Hamiltonian in this electronic basis.

$$\left\langle \pi_i^{(1)} \middle| H \middle| \pi_i^{(1)} \right\rangle = T_i + E^{(1)}\left(Q_i\right) + \sum_{j \neq i}^{N} \left(T_j + E^{(0)}\left(Q_j\right) + \left\langle \pi_i^{(1)} \middle| V_{i,j} \middle| \pi_i^{(1)} \right\rangle \right) \tag{2.3}$$

$$\left\langle \pi_i^{(1)} \middle| H \middle| \pi_j^{(1)} \right\rangle = \left\langle \pi_j^{(1)} \middle| H \middle| \pi_i^{(1)} \right\rangle = \left\langle \pi_i^{(1)} \middle| V_{i,j} \middle| \pi_j^{(1)} \right\rangle \tag{2.4}$$

By expanding the coupling term in a Taylor expansion and only keeping the constant term, as done in Eq. (1.10), we are able to simplify Eq. (2.4) to N-choose-2 constants (instead of just one constant in the dimer case). Eq. (2.3) will have each potential energy surface term ($E^{(1)}(Q_i)$) approximated as a parabola as in Eq. (1.11). This results in an $N \times N$ block matrix with the following structure.

$$H = \begin{pmatrix} H_{1,1} & V_{1,2} & \cdots & V_{1,N} \\ V_{1,2} & H_{2,2} & \cdots & V_{2,N} \\ \vdots & \vdots & \ddots & \vdots \\ V_{1,N} & V_{2,N} & \cdots & H_{N,N} \end{pmatrix} \tag{2.5}$$

$$H_{i,i} = \frac{P_i^2}{2M} + E_i + l_i Q_i + \frac{1}{2} M \omega_i^2 Q_i^2 + \sum_{j \neq i}^{N} \frac{P_j^2}{2M} + \frac{1}{2} M \omega_B^2 Q_j^2 \tag{2.6}$$

It is interesting to note that the magnitudes of the coupling matrix elements will depend highly on the structural layout of the chromophores. For instance, in linear trimer stacks as done by Seibt and co-workers [47], $V_{1,2} = V_{2,3} \neq 0$ and $V_{1,3} = 0$. For a trimer close to C_3 symmetry, the coupling constants will have the form $V_{1,2} \simeq V_{2,3} \simeq V_{1,3} \neq 0$.

By representing the position and momentum operators in Eq. (2.6), the matrix elements of Eq. (2.5) in a vibronic-electronic basis are computable:

$$\begin{aligned}\left\langle \pi_i^{(1)} \middle| H \middle| \pi_i^{(1)} \right\rangle &= b_i \hbar\omega_i \left(\sqrt{n_i+1}\,\delta_{\left(n_i',n_i+1\right)} + \sqrt{n_i}\,\delta_{\left(n_i',n_i-1\right)} \right) \prod_{j\neq i}^{N} \delta_{\left(n_j',n_j\right)} \\ &+ \left(E_i + \sum_{j=1}^{N} \hbar\omega_j \left(n_j + \frac{1}{2} \right) \right) \prod_{j=1}^{N} \delta_{\left(n_j',n_j\right)} \qquad (2.7)\end{aligned}$$

$$\left\langle \pi_i^{(1)} \middle| H \middle| \pi_j^{(1)} \right\rangle = V_{i,j} \prod_{j=1}^{N} \delta_{\left(n_j',n_j\right)} \qquad (2.8)$$

Here n_i and n_i' represent the excitation quanta of a given normal mode on the i'th chromophore. While it is not written out because the indexing gets very confusing, Eqs. (2.7) and (2.8) can also be easily extended to the case with multiple vibrations on each chromophore. Each matrix element becomes a sum over Hamiltonians for each vibration and the vibrational basis is a product of individual vibrational basis functions.

2.1.2 Multi-chromophore Inter-monomer Modes

The derivation of the inter-monomer mode Hamiltonian is much more complicated for the case where there are multiple chromophores. As done for the dimer case, the derivation will begin in the exciton de-localized basis. This electronic basis will be notated as $\left\{\pi_i^{(\pm)}\right\}_{i=1,2,\ldots N}$, where the ± is used to emphasize that it serves the same role at the $\pi_\pm^{(1)}$ basis in the dimer case and can be related to the basis seen in Eq. (2.2) with a linear transformation.

It is now possible to evaluate the T_L and remaining non-constant terms of $V_{i,j}$ using the exciton delocalized basis. This is done in the same way as in Eqs. (1.25) and (1.26), only now there will be N matrix elements to evaluate, one for each delocalized excited state. Note that the constant term with regard to the Taylor expansion of $V_{i,j}$ is not included with the inter-monomer mode Hamiltonian because it is already included with the intra-monomer mode Hamiltonian.

$$\left\langle \pi_k^{(\pm)} \right| T_L + \sum_{i=1}^{N} \sum_{j \neq i}^{N} V_{i,j}(L) \left| \pi_k^{(\pm)} \right\rangle \simeq l_{L,k} L + \frac{1}{2} M \omega_{L,k}^2 L^2 + \frac{P_L^2}{2M} \tag{2.9}$$

On first glance, this equation may seem overly simple. After all we have N-choose-2 $V_{i,j}$ terms on the left handed side and only three terms on the right hand side. This comes from the fact that each $V_{i,j}$ term contributes to the linear and quadratic constants in the Taylor expansion, but it does not matter how much each term contributes. In other words, one can write the following expression:

$$l_{L,k} = \sum_{i=1}^{N} \sum_{j \neq i}^{N} \frac{\partial}{\partial L} \left\langle \pi_k^{(\pm)} \right| V_{i,j}(L) \left| \pi_k^{(\pm)} \right\rangle \tag{2.10}$$

A similar relationship exists for the quadratic term $\omega_{L,k}$.

Now the cross terms of these inter monomer modes must be computed. Fortunately this is actually much simpler than the diagonal terms because the $\left\{ \pi_i^{(\pm)} \right\}_{i=1,2,\ldots N}$ is, by definition, the basis that diagonalize the coupling matrix. In other words, the wavefunctions returned by an electronic structure calculation (which is what is meant by the exciton delocalized basis) are not coupled through the Hamiltonian by the very nature of the calculation. Therefore, without further analysis it is possible to write:

$$\left\langle \pi_k^{(\pm)} \right| T_L + \sum_{i=1}^{N} \sum_{j \neq i}^{N} V_{i,j}(L) \left| \pi_l^{(\pm)} \right\rangle = 0 \tag{2.11}$$

(Aside: This is how I pictured things working when I originally started this math. However, on further thought, this may not be true. In fact, setting the cross term derivatives to non-zero parameters may allow for localization of the excitation by the vibration. I will attempt to code these parameters in a completely general way so that we can play around with these parameters.)

Now all that remains is transforming this coupling matrix back into the exciton localized basis so that it may be added to the intra-monomer Hamiltonian. However, because different coupling combinations are possible, the transformation between these bases is not known as it is in the dimer case (Eq. (1.28)). It can, however, be computed by diagonalizing the coupling matrix in the exciton localized basis. The eigenvectors produced from this digitalization step will be the exciton delocalized states in the exciton localized basis. Define the basis transformation matrix U in the following way:

$$\begin{pmatrix} \lambda_1 & 0 & \cdots & 0 \\ 0 & \lambda_2 & \cdots & 0 \\ \vdots & \vdots & \ddots & \vdots \\ 0 & 0 & \cdots & \lambda_N \end{pmatrix} = U^{-1} \begin{pmatrix} 0 & V_{1,2} & \cdots & V_{1,N} \\ V_{1,2} & 0 & \cdots & V_{2,N} \\ \vdots & \vdots & \ddots & \vdots \\ V_{1,N} & V_{2,N} & \cdots & 0 \end{pmatrix} U \tag{2.12}$$

In this calculation, the splittings between the λ_i values should match the splittings between the electronic energies of the molecule before applying the vibronic coupling model. That is to say that the splittings should be the same as those found in a pure electronic structure calculation. This can be used as a check to verify the accuracy of the coupling constants.

Once the U matrix is known, the transformation of the inter-monomer mode Hamiltonian back to the exciton localized basis is simply performed by matrix multiplication.

$$U \begin{pmatrix} l_{L,1}L + \frac{1}{2}M\omega_{L,1}^2 L^2 + \frac{P_L^2}{2M} & 0 & \cdots & 0 \\ 0 & l_{L,2}L + \frac{1}{2}M\omega_{L,2}^2 L^2 + \frac{P_L^2}{2M} & \cdots & 0 \\ \vdots & \vdots & \ddots & \vdots \\ 0 & 0 & \cdots & l_{L,2}L + \frac{1}{2}M\omega_{L,2}^2 L^2 + \frac{P_L^2}{2M} \end{pmatrix} U^{-1} \tag{2.13}$$

2.2 Intensities

After diagonalizing the full Hamiltonian in the vibronic-electronic basis and obtaining the energy levels, it becomes necessary to compute the intensity of each transition through the electronic dipole moment. In much the same manner as done in Eq. (1.41), it is possible to separate the transition dipole moment from the vibrational integrals. However, in this case there are now N independent transition dipole moments (TDMs) that a given state can transition through. Since these N TDMs do not all have to be of the same strength (or polarization), it must be possible to assign each transition to an individual TDM or some linear combination thereof. As it turns out, the U matrix becomes necessary for this segment as well.

Begin by defining the excited state as a linear combination of electronic-vibronic basis functions as done in Eq. (1.33) for the dimer calculation:

$$\psi_1 = \sum_{i=1}^{N} \pi_i^{(1)} \sum_{m,n_1,n_2,\ldots n_N} C^i_{m,n_1,n_2,\ldots n_N} \phi_m(L) \prod_{j=1}^{N} \phi_{n_j}(Q_j) \tag{2.14}$$

Here $C^i_{m,n_1,n_2,\ldots n_N}$ is the coefficient on a specific electronic-vibronic wavefunction, $\phi_{n_j}(Q_j)$ is the n_j vibrational basis function localized on the j'th monomer, and $\phi_m(L)$ is the m'th vibrational basis function for an inter-monomer mode. By applying the U matrix, it is possible to transform this wavefunction into the exciton delocalized electronic basis.

$$\psi_1 = \sum_{i=1}^{N} \pi_i^{(\pm)} \sum_{m,n_1,n_2,\ldots n_N} \left(\sum_{k=1}^{N} U_{i,k} C^k_{m,n_1,n_2,\ldots n_N} \right) \phi_m(L) \prod_{j=1}^{N} \phi_{n_j}(Q_j) \tag{2.15}$$

To find absorption intensities simply integrate over all coordinates the product of the initial ground state wavefunction, the final excited state wavefunction, and the transition dipole operator and square the result. Assuming we are starting in the unexcited vibrational wavefunction, coefficients of the final wavefunction with $m = n_1 = n_2 = \ldots n_N = 0$ will have a vibrational overlap integral of unity while all other basis function will have a vibrational overlap integral of zero. Since the electronic integral of the ground electronic state, i'th excited electronic state, and transistion dipole operator simply returns the i'th TDM, the total intensity for the transition can be written as:

$$R = \sum_{i=1}^{N} \mathrm{TDM}_i^2 \left(\sum_{k=1}^{N} U_{i,k} C^k_{0,0,\ldots 0} \right)^2 \tag{2.16}$$

In this expression it is easy to see the contribution from each individual TDM to the total intensity. Emission intensities can be computed analogously and hot bands may be computed by using vibrational quantum numbers other than all zeros.

3. FGMC PROGRAM FOR MODELING VIBRONIC INTERACTIONS

FGMC computes emission and absorption spectra for molecular systems with multiple chromophores where nearly degenerate excited states cause coupling between electronic and vibrational degrees of freedom. It is currently written in Matlab [48] and has a graphical user interface (GUI) for easy use. The theory behind FGMC was originally proposed by Witkowski and Moffitt [49] and extended upon by Fulton and Gouterman. [9]

This chapter describes the usage of FGMC and is broken into four sections, the first of which is this introduction. Section 3.1 will go over the parts of the GUI and describe it's functionality. Section 3.2 will cover the execution of a calculation. Finally, Section 3.3 will examine the output of a calculation.

3.1 Using the GUI

After extracting the zip file, it is necessary to add the directory containing these programs to the Matlab path. This can be done through the path dialogue box opened by clicking on 'File' and then 'Set Path' or it may be added using the following command:

```
path(path,'$Directory');
```

where $Directory is the location of the unzipped files.

After modifying Matlab's path, the GUI can be opened by typing 'FGMC' into the command line. This will bring up a window much like that seen in Fig. 3.1. For

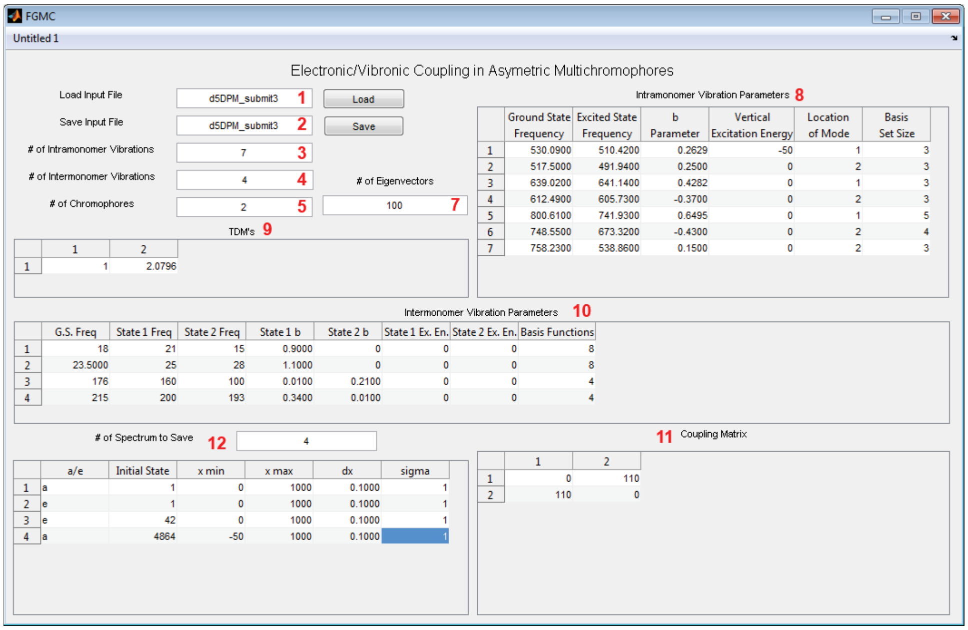

Electronic/Vibronic Coupling in Asymetric Multichromophores

Load Input File d5DPM_submit3 1
Save Input File d5DPM_submit3 2
# of Intramonomer Vibrations 7 3
# of Intermonomer Vibrations 4 4
# of Chromophores 2 5
# of Eigenvectors 100 7

TDM's 9

	1	2
1	1	2.0796

Intramonomer Vibration Parameters 8

	Ground State Frequency	Excited State Frequency	b Parameter	Vertical Excitation Energy	Location of Mode	Basis Set Size
1	530.0900	510.4200	0.2629	-50	1	3
2	517.5000	491.9400	0.2500	0	2	3
3	639.0200	641.1400	0.4282	0	1	3
4	612.4900	605.7300	-0.3700	0	2	3
5	800.6100	741.9300	0.6495	0	1	5
6	748.5500	673.3200	-0.4300	0	2	4
7	758.2300	538.8600	0.1500	0	2	3

Intermonomer Vibration Parameters 10

	G.S. Freq	State 1 Freq	State 2 Freq	State 1 b	State 2 b	State 1 Ex. En.	State 2 Ex. En.	Basis Functions
1	18	21	15	0.9000	0	0	0	8
2	23.5000	25	28	1.1000	0	0	0	8
3	176	160	100	0.0100	0.2100	0	0	4
4	215	200	193	0.3400	0.0100	0	0	4

# of Spectrum to Save 12 4

	a/e	Initial State	x min	x max	dx	sigma
1	a	1	0	1000	0.1000	1
2	e	1	0	1000	0.1000	1
3	e	42	0	1000	0.1000	1
4	a	4864	-50	1000	0.1000	1

11 Coupling Matrix

	1	2
1	0	110
2	110	0

Figure 3.1. Screenshot of the GUI with parameters used to simulate d_5-DPM. Numbers in red label various points referred to in text.

the remainder of this chapter the numbers in red in Fig. 3.1 will be used to refer to various sections of the GUI.

3.1.1 Loading and Saving

Using text box (1) in Fig. 3.1 and the 'Load' button it is possible to read in a previously written input file. The file name into the text box and press the load button. The current working directory of Matlab must be the directory containing the file that is to be read. Matlab's working directory can be determined by using the 'pwd' command and changed with the 'cd' command in the Matlab command line.

Once all of your parameters have been entered into the GUI, it is necessary to save your input file whether the calculation is to be run locally or on a remote server. Enter a file name into the text box (2) in Fig. 3.1 and press the save button to save an input file. It will be written in Matlab's current working directory.

3.1.2 Entering the Size of the Calculation

Text boxes (3-6) in Fig. 3.1 can be used to adjust the size of a calculation. Boxes (3) and (4) define the number of intra and inter-monomer modes in the system and will automatically adjust tables (7) and (10), respectively. Box (5) defines the number of chromophores (and thus the number of nearly degenerate electronic states) in your system. Thus changing the number of chromophores alters the size of tables (9-11). Finally, box (7) details how many eigenstates will be found using the Lanczos algorithm. This value directly effects computational time as well as memory requirements. The upper bound on the value of this box is given by:

$$\begin{aligned}\text{(Number of Eigenvectors)} < \text{(Number of Chromophores)} \times \\ \prod \text{(Intra-monomer Basis Set Sizes)} \times \\ \prod \text{(Inter-monomer Basis Set Sizes)} \qquad (3.1)\end{aligned}$$

This is simply the product of all the vibrational basis set sizes times the electronic basis set size and represents the dimensionality of the Hamiltonian.

3.1.3 Intra-monomer Vibrational Modes

Table (8) contains the parameters for the intra-monomer modes. It will always have 6 columns, but the number of rows depend on the value in box (3). The first column is for the ground state frequency of the vibrational mode multiplied by $\hbar$. Though any units of energy will work in these simulations so long as they are consistently used throughout the parameter set, normally these values are entered in wavenumbers. The second column is the frequency of the vibrational mode in the excited state.

The third column is the unit-less displacement, or Frank-Condon, parameter for the normal mode. These parameters can be obtained from Ez-Spectrum [36] and then performing a unit conversion on the listed dQ value.

$$b = dQ_m\sqrt{\left(\frac{\omega'}{\omega}\right)^3 \frac{\omega'}{2\hbar}} \simeq dQ_m\sqrt{\left(\frac{\omega'}{\omega}\right)^3 \omega' \times .01483 \frac{1}{cm\ AMU\ \text{Å}^2}} \tag{3.2}$$

In this equation ω' is the excited state frequency of the given normal mode and ω is the ground state frequency. An example for the necessary constant is given when using the wavenumber/angstrom/AMU unit system.

The fourth column of the table gives the vertical excitation energy for a given normal mode. While it is sometimes convenient to ascribe a value for the vertical excitation energy for each vibration, computationally the only value of importance is the sum of all vertical excitation energies on each monomer.

The fifth column of the table gives the location of the vibrational mode and has allowed values of 1 through N, where N is the number of chromophores. It does not matter how the chromophores are ordered, so long as the same ordering is used throughout the input.

The sixth column of the table gives the number of basis functions to be used to simulate the given vibration. 5 basis functions are recommended, though for vibrations that have small displacement and frequency change parameters as few as 3 may be used. Likewise, for vibrations with large displacements between the ground and excited state, more basis functions may be required.

3.1.4 Inter-monomer Vibrational Modes

Table (10) contains parameters for the inter-monomer modes. The number of columns in this table is dependant on the number of chromophores in the simulation. The first $N+1$ columns contain the ground through $N'th$ excited state frequencies for a given vibration. The next N columns contain the displacement parameter for that vibration for the N excited states, computed using 3.2. The final set of N columns contain the vertical excitation energies for each electronic excited state. Finally, the last column contains the number of basis functions that will be used to simulate each mode. Similar rules should be used for selecting the appropriate number of basis functions as were used in the intra-monomer vibrational modes.

3.1.5 Transition Dipole Moments

Table (9) contains the transition dipole moment values for the various excited states of the multi-chromophore. As a general rule, TDM's in this table should be given in the order from lowest energy electronic state to highest, though this may not always be the case for systems in a very weak coupling limit, [10] where $b\hbar\omega$ is large compared to V.

3.1.6 Electronic Coupling Matrix Elements

Table (11) contains the electronic inter-monomer coupling constants to be used in the simulation. This matrix is constrained to be Hermitian because of the following relation

$$\left\langle \pi_i^{(1)} \middle| V\left(L\right) \middle| \pi_j^{(1)} \right\rangle = \left\langle \pi_j^{(1)} \middle| V\left(L\right) \middle| \pi_i^{(1)} \right\rangle \tag{3.3}$$

For systems with more than 2 chromophores, it is necessary that the number labels for the coupling constants match the location labels given to the intra-monomer vibrations in table (8).

3.1.7 States to Print

Table (12) contains the information on which spectra should be saved. The first column defines whether to save an absorption (a) or emission (e) spectra. The second column contains integer value that denotes the state from which to emit or absorb. If an emission spectrum is requested this value is simply the state number printed out in the first column of the vibrationally unexcited ground state absorption spectrum.

If an absorption spectrum is requested this value can be used to denote a vibrationally excited ground state, resulting in a hot band. A value of '1' corresponds to the zero point vibrational ground state. To compute the value of this box for a given vibrational state, use the following expression

$$1 + \sum_{i=1}^{V} v_i \prod_{j<i} s_j \tag{3.4}$$

Here, v_i is the number of vibrational quanta in the i'th vibrational mode with zero representing the ground state, V is the total number of vibrations (inter and intra), and s_j is the total basis set size of the j'th vibration. For $i = 1$, $\prod_{j<i} s_j = 1$. It is also important to note that the order of modes is important, with the order being the same as they appear in the GUI tables and intra coming before inter-monomer vibrations. This calculation is easily performed in the Matlab command line interface. Start by creating a vector of the vibrational basis set sizes for both the intra and inter-monomer modes in the order in which they appear in the table, with the intra-monomer modes appearing first. Next, take the cumulative product of this vector, append a '1' to the beginning and delete the last element. Now create a new vector with the same number of elements as the first vector, where each element represents the number of vibrational quanta in each vibrational mode. Finally, take a dot product between the two vectors and add 1.

For example, the fourth absorption spectrum in 3.1 is the absorption from the vibrational state with one quantum of excitation in the second intra-monomer mode and 1 quanta of vibrational excitation in the first inter-monomer mode. The value 4864 is arrived at in the following way:

$$4864 = 1 * (3) + 1 * (3 * 3 * 3 * 3 * 5 * 4 * 3) + 1 \tag{3.5}$$

Column three and four give the lowest and highest energy value to be printed in the spectrum respectively. Column five is the spacing between points in the spectrum. Finally, column six is the width of a peak. Keep in mind that even though a large xmax is requested, the program will only find as many states as given in (7). Thus, if the highest energy computed state is less than xmax, the remainder of the spectrum will be shown as giving zero peaks even if there are states in that region of the spectrum.

3.2 Running a Calculation

Due to the size of some FGMC calculations, it is possible to run a calculation both locally and on a remote server. Generally smaller calculations (those with under 2,000,000 basis functions) can be run locally, though Matlab may end up consuming a fair amount of memory. Larger calculations can be run remotely, both to increase available memory and to allow for increased parallelization during the digitalization step.

3.2.1 Locally

Running calculations locally is straight forward, though it does require use of the command line. Once you have opened the GUI and entered the necessary parameters, switch back to the command line window. Move Matlab to a new directory, enter a name for the calculation into box (2) and press the save button. This will write the parameter file. Now switch back to the command line and run:

```
FGMC1server('$Filename');
```

where $Filename is the name entered into box (2). The calculation will run, printing out some diagnostic information to the command line window. Note that the 'Estimated completion time' only applies for the Hamiltonian generation segment of the program. For smaller calculations, this is the majority of the run time, though for larger calculations the digitalization algorithm will take much longer.

3.2.2 Submitting to a PBS Queue

Included in the zipped folder is a script called 'FGMCsub.sh'. This script is used to submit calculations to a Torque queueing system. 'FGMCsub.sh' operates by creating two scripts, one run by Matlab and one run by the Linux OS. Some likely modifications that will need to be made to get the program running on your system are:

- Line 63: Change the default queue.
- Line 83: Add the directory containing FGMC1server on the local system to the Matlab path.
- Line 96: Load Matlab system variables into the computer. This may not be needed depending on the system.

3.3 Interpreting the Results

After the program is complete, the spectra and state information will be saved to files named $Filename_N.mat and $Filename_N.txt respectively, where N is the row number in the spectrum table corresponding to that spectrum. The .txt file contains a list of transitions that make up the spectrum. If the spectrum is an absorption spectrum the first line will contain a list representing the initial vibrational state of the system. If the spectrum is an emission spectrum, the first line will contain a single number representing the state from which the emission spectrum was simulated. The 'zero' of energy for these simulations is always set as the excitation energy from the ground state to the lowest excited state.

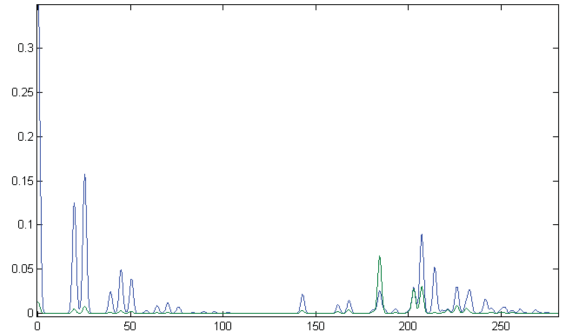

Figure 3.2. Absorption spectrum from DPM-d_5 simulation as plotted by Matlab. The S_1 origin is in blue at $0\,\mathrm{cm}^{-1}$ and the S_2 peak is in green at $185\,\mathrm{cm}^{-1}$.

The .mat file can be used to make plots of the spectra according to the plotting parameters input into the GUI, as seen in Fig. 3.2. With Matlab in the same directory as the .mat file, type 'load $JOBNAME_N.mat' followed by 'plot(xmin:dx:xmax,yvec)' to produce a plot of the simulated spectra. The absorption from the vibrationaly unexcited ground state for the d_5-DPM parameters shown in Fig. 3.1 is shown in Fig. 3.2. Transitions through different TDM's will be in separate traces, making the components of each electronic state easy to identify. Finally, different spectra can be loaded into Matlab and plotted by changing N in the load command, but unless the original spectra are renamed, the data will be lost.

4. EV-SPECTRUM FOR ELECTRONIC-VIBRONIC COUPLING

Due to the large number of application of vibronic electronic Hamiltonians in the literature. As we have found previously, the limiting factor in many of these calculations is the size of the Hamiltonian. The dimer simulations performed on DPM pushed the limit of modern computers, frequently requiring 16 or more gigabytes of memory to run successfully.

Another problem with previous simulations is the constrained form of the Hamiltonian. In the previous described model Hamiltonians, all terms were expanded to second order in a Taylor series. It is, however, possible to imagine many other types of Hamiltonian elements involved in vibronic coupling. For example, anharmonic or mechanical interactions can be included in the Hamiltonian with Q^3 or Q_1Q_2 terms respectively. Further, a more diverse set of electronic coupling terms exists involving any combination of $|i\rangle Q\langle j|$, where i and j are any two electronic states being examined.

With these challenges in mind, a new more general program for diagonalizing these Hamiltonians was written.

4.1 Design

To accommodate these requirements, a general sparse matrix diagonalization code was needed. PETSc with the SLEPc extension was chosen for this role. The primary feature of these codes that was needed here was the matrix shell functionallity. Instead of writing an algorithm to build the Hamiltonian and store it in memory, as is done

Figure 4.1. Traditional matrix multiplication, left, requires the entire Hamiltonian to be constructed to find the red product vector. The matrix/vector product algorithm in EVspectrum, pictured right, uses the operator form of the Hamiltonian to compute the matrix vector product.

in FGMC, an algorithm to compute a single matrix vector product based on the Hamiltonian's operator form was written (4.1). Then the Krylov-Schur sparse matrix diagonalization algorithm is used to determine the first few eigenvectors using only the matrix-vector product algorithm and the Hamiltonian's diagonal.

4.2 Installation

To install EVspectrum, the required PETSc [50–52] and SLEPc [53–55] packages must first be installed. These can be obtained from their respective websites http://www.grycap.upv.es/slepc/ and http://www.mcs.anl.gov/petsc/.

Once these two packages are installed, download the source code from GitHub [56]. After correctly defining the environment variables ${SLEPC_DIR} and ${PETSC_DIR}, run simply run make in the source code directory. This should create an executable file called EVspectrum. This executable can then be moved to a ${PATH} directory to be called later.

4.3 Running EVspectrum

To run EVspectrum, place an input file named ”input.inp” in an empty directory and set that directory to the current working directory. To run EVspectrum in serial, once the executable is in a ${PATH} directory, simply call EVspectrum from the command line with no arguments. After execution,

To run EVspectrum in parallel the petsc mpi kicker program, located at

```
${PETSC_DIR}/bin/petscmpiexec
```

must be used. Simply call

```
${PETSC_DIR}/bin/petscmpiexec -n ${TOTCPU} EVspectrum
```

from the command line where ${TOTCPU} is the total number of CPUs you would like to devote to the process.

4.4 Input File Format

The program will now be explained by way of example. Consider the following system Hamiltonian:

$$H = \begin{pmatrix} 550\left(n_A+\frac{1}{2}\right)+500\left(n_B+\frac{1}{2}\right)+440Q_A & 110 \\ 110 & 560\left(n_A+\frac{1}{2}\right)+490\left(n_B+\frac{1}{2}\right)+343Q_B \end{pmatrix} \tag{4.1}$$

This system can be described as a bichromophore with a single vibrational mode on each of two chromophores. The ground state vibration on chromophore A is $560\,\mathrm{cm}^{-1}$ while the excited state frequency is $550\,\mathrm{cm}^{-1}$. Similarly, the ground state vibration on chromophore B is $500\,\mathrm{cm}^{-1}$ while the excited state vibration is $490\,\mathrm{cm}^{-1}$. The displacement parameter b as defined in 1.22 for the two vibrations are .8 and .7 for the vibrations on the A and B monomers, respectively. Finally, the coupling constant between the two chromophores is $110\,cm^{-1}$.

The input to simulate this Hamiltonian can be found in the Appendix. There are 5 section to the input file, 4 of which contain input parsed by the program. Excluding the $comment section, the next four sections will be explained one by one.

4.4.1 Problem Section

The $problem section of the input outlines the basic parameters of the Hamiltonian you seek to diagonalize. There are precisely 4 keywords, all of which must be included but can be included in any order. The **nvib** keyword which dictates the total number of vibrational modes in the system. It must be followed by a single integer, which in this case is 2 since one vibrational mode belongs to each of the two chromophores. The **nelec** keyword dictates the number of electronic states in the Hamiltonian. There are 2 low level electronic states in a bichromophore so a Hamiltonian with two electronic states is considered. The **neigen** keyword dictates how many states will be computed. In this simulation, the lowest 30 states are requested. The **vbasis** keyword indicates the number of vibrational basis functions for each vibration which must be at least 2. Unlike the other keywords, this is followed by a list of integers with a number of elements equal to **nvib**. In this calculation, both vibrations will be simulated with 8 harmonic oscilator basis functions.

4.4.2 Hamiltonian Section

In this section, the individual Hamiltonian operators are listed, one per line. Each line has three parts which must be in the correct order. The first part is c[#], which indicates a constant value that must be listed in the next section. As seen in entries 1 and 2 in this section, multiple matrix elements may have the same constant value. The next section indicates the electronic states that the matrix element will interact with in bra-ket notation. Each value in the bras and kets must range between 1 and **nelec**. If the two values are the same the matrix element will be parameter for a specific electronic state. If the two values are different, the matrix element will appear in an off diagonal block of the Hamiltonian and represent an electronic coupling element. For instance, in this system, there is an electronic coupling constant (V_{AB}) of 110cm^{-1} indicated by entries 11 and 12.

The final entry in a given line is the list of vibrational operators that make up the Hamiltonian element. There can be as many or as few vibrational operators as desired, with no operators indicating a constant, on diagonal element. The three possible operators are the raising operator a∧, the lowering operator a_, and the number operator n. Each of these operators is followed by a number in square brackets that ranges from 1 to **nvib**, indicating which vibration the operator belongs to. This free form method for accepting kinimatic couplings such as a_[1]a_[2] or anharmonicities such as a_[1]a_[1]a_[1] terms.

4.4.3 Parameters Section

In this section, the values of the constants used in the $hamiltonian section are defined. One constant is reported on each line, followed by a space and the value to which it corresponds. Each constant is read in as a double precision floating point number, so decimals are allowed. It is important that the value for each constant used in the $hamiltonian section is defined.

4.4.4 Groundfrequency Section

In this section, the ground state frequencies for each of the vibrational modes are defined. The number of entries in this section should be equal to the value of **nvib** in the $problem section. These values are only used in computing the emission spectra from various excited states.

4.5 Conclusions

With this program it is possible to simulate vibronic coupling effects in a wide variety of systems with a wide variety of effects. The input file format for EVspectrum has been explained and should be fairly intuitive. In future work on this program, functionality for initially hot molecules should be added as well as a method to build a basic input from quantum chemical simulations. Further, there is a desire to interface the program with a genetic algorithm optimizer that will allow one to optimize a specific Hamiltonian when compared to an experimental spectrum.

5. α-METHYLBENZYL RADICAL SIMULATIONS

The goal of this chapter was to determine the geometry of the methyl rotor in the α-methylbenzyl (α-MeBz) radical in the ground and D_1 state. Based on experimental results [57] it is known that the methyl rotor changes geometry upon this excitation, but it was not immediately clear which orientation was present in the ground state and which was present in the excited state. The two possible structures are shown in Fig. 5.1. Various ab-initio stratagems were imploded to assist in answering this question.

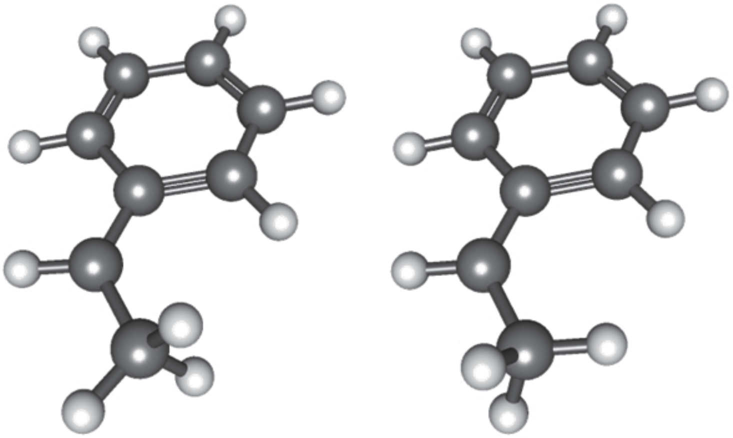

Figure 5.1. The two possible orientations of the methyl rotor in the α-MeBz radical. Left: the anti configuration with the in plane C-H methyl bond opposite the C-Ph bond. Right: the syn configuration with the C-H methyl bond on the same side as the C-Ph bond.

5.1 Methods

Excited state calculations on α-MeBz and benzyl radicals were carried out with a variety of correlated single-reference excited state methods of equation of motion coupled cluster (EOM-CC) family, [42, 58, 59] using the Q-Chem [35] electronic structure package. Vertical excited state properties (vertical excitation energies, transition dipole moment (TDM) components, oscillator strengths, and the D_1-D_2 energy splitting) for the benzyl radical and α-MeBz were determined using EOM-CC for ionization potentials (EOM-IP-CCSD) [60, 61] in the aug-cc-pVDZ basis. Vertical excitation energies for the D_1 and D_2 states were further refined by adding perturbative triple corrections as in the EOM-IP-CCSD(dT) method. EOM-CC method for excitation energies with single and double excitations (EOM-EE-CCSD) [42, 58, 59] in the aug'-cc-pVDZ basis (aug-cc-pVDZ without diffuse p functions on hydrogens and diffuse d functions on carbons) was also employed. EOM-EE-CCSD calculations used open-shell doublet reference, while all IP calculations used the closed shell anion state as the reference determinant.

In order to determine the preferred methyl rotor orientation in α-MeBz, the ground state and the D_1 excited state geometries were determined for the (fixed) anti and syn orientations of the methyl rotor with respect to the aromatic ring (Fig. 5.1. EOM-EE-CCSD/aug'-cc-pVDZ and the ionization potential configuration interaction with single and double excitations (IP-CISD) method in aug-cc-pVDZ were used for the geometry optimizations. Calculations with more accurate EOM-IP-CCSD and EOM-IP-CC(2,3) (EOM-IP method with single and double excitations for the reference state and single, double, and triple excitations for the excited state) [62] were additionally performed at the IP-CISD optimized geometries of the D_0 and D_1 states.

Additionally, a set of multi-configurational calculations with multi-configurational self-consistent field (MCSCF) [63] and multi-configurational quasi-degenerate perturbation theory (MCQDPT) [64] were performed in the GAMESS electronic structure software. [65] Equilibrium geometries of the D_0 and D_1 states in anti and syn orientations were optimized at the MCSCF/6-31G* [66, 67] level of theory. Single-point energy calculations at the optimized geometries were performed at the MCSCF/cc-pVTZ and MCQDPT/cc-pVTZ levels. Seven active orbitals (six π orbitals at the benzene ring and a radical π orbital on the CH_2 moiety) with seven electrons comprised the active space for the benzyl radical. σ and $\sigma*$ CH orbitals on the methyl rotor were added to the active space of $\alpha-$MeBz, bringing the active space to nine orbitals and nine electrons. State averaging of the three lowest states (D_0, D_1, and D_2) was employed in the MCSCF and MCQDPT energy calculations.

Additionally, geometry optimizations of the α-MeBz cation in anti and syn configurations of the methyl rotor were performed at the B3LYP/6-311+G** [33] level. Single point energies at these geometries were obtained at the coupled CCSD(T)/cc-pVTZ [68] level of theory.

The close correspondence between experiment and calculation establishes that the first transition in the excited state spectra involves transitions to the D_1 electronic state, producing a 53%:47% a:b hybrid band. By comparison, the corresponding D_0-D_2 transition would be pure a-type, inconsistent with the experimental data.

5.2 Calculated Results

To calibrate various levels of theory, we have carried out calculations on the excited states of the benzyl radical. Since the TDM directions and relative oscillator strengths of the D_0-D_1 and D_0-D_2 transitions are known for the benzyl radical, [69, 70] it provides a benchmark for decisions on the level of theory needed to correctly describe the excited states of α-MeBz. In the benzyl radical, the D_0-D_1 transition is known to be a very weak, pure B-type band, while the vibronically induced transitions are pure A-type peaks associated with the D_0-D_2 transition with much greater oscillator strength. Based on their analysis of this vibronic coupling, Cossart-Magos and Leach surmised that the D_2 state is only 430-485 cm^{-1} above D_1.

While MCSCF provides a qualitatively correct description of the first two excited states in benzyl and α-MeBz, it misses dynamic correlation effects which leads to the wrong order of the two states, as shown in Table 5.1, consistent with the calculations of Rice et al. [71] Introducing dynamic correlation through configuration interaction as was done by Negri et al. [72] or using multiconfigurational perturbation theory recovers the correct order of the excited states (see Table 5.1). Even though the 1^2A2 state in benzyl is the second excited state at the ground state geometry at the MCSCF level, it becomes the lowest excited state near its own equilibrium geometry. As a result, it is possible to find the optimized geometry of this state and its vibrational frequencies as needed. However, it was not possible to find an optimal geometry of the corresponding (B-type) state in α-MeBz using MCSCF, due to a destabilizing steric repulsion of the methyl group with the aromatic ring and stronger mixing of the two excited states. On the contrary, MCSCF geometry optimizations in α-MeBz always converge to the equilibrium structure of the other (A-type) state. Since the MCQDPT analytic gradients are not available, it becomes very challenging to obtain accurate values of the methyl rotor barrier

The spectral data and analysis just presented have provided experimentally derived shapes, barrier heights, and change in preferred orientations for the methyl group upon electronic excitation. However, a direct measure of the preferred orientation of the methyl rotor in either state is missing. Thus, we performed a set of ab initio calculations aiming to predict the preferred methyl orientations in D_0 and D_1. We also sought additional insight to the methyl CH stretch region of the infrared, and the observed changes that accompanied electronic excitation there.

To calibrate various levels of theory, we have carried out calculations on the excited states of the benzyl radical. Since the TDM directions and relative oscillator strengths of the $D_0 \rightarrow D_1$ and $D_0 \rightarrow D_2$ transitions are known for the benzyl radical, [70, 73] it provides a benchmark for decisions on the level of theory needed to correctly describe the excited states of α-MeBz. In the benzyl radical, the $D_0 \rightarrow D_1$ transition is known to be a very weak, pure B-type band, while the vibronically-induced transitions are

Table 5.1.

Comparison of the Vertical Energy Splittings (cm^{-1}) between the D_1 and D_2 states of benzyl and α-MeBz radicals provided by different levels of theory. Positive values correspond to the state with TDM along b axes ($^2A_2$ state of the benzyl radical) being the lowest one. All calculations are performed at the ground state geometries (geometry of the anti isomer is used for α-MeBz).

level of theory	benzyl	α-methylbenzyl
EOM-EE-CCSD/aug'-cc-pVDZ[1]	-239.0	563.8
EOM-IP-CCSD/6-311+G(d,p)[2]	1197.2	742.8
EOM-IP-CCSD(dT)/6-311+G(d,p)[2]	592.2	478.6
MCSCF/cc-pVTZ[3]	-1288.8	-1666.6
MCQPDT/cc-pVTZ[3]	1209.3	1138.1

[1] G.S. geometry optimized at EOM-EECCSD/aug'-cc-pVDZ.

[2] G.S. geometry optimized at EOM-IP-CCSD/6-311+G(d,p).

[3] G.S. geometry optimized at MCSCF(9,9)/6-31G(d). State averaging for the three lowest states (D_0, D_1, D_2) was employed for energy calculations.

pure A-type peaks associated with the $D_0 \rightarrow D_2$ transition with much greater oscillator strength. Based on their analysis of this vibronic coupling, Cossart-Magos and Leach surmised that the D2 state is only 430 – 485 cm^{-1} above D_1. [73]

Description of the electronic states in the benzyl radical is a challenging task for the electronic structure theory since both dynamic and non-dynamic correlations are important. The molecular orbitals involved in forming the three lowest electronic states of the benzyl radical are shown in Fig. 5.2. The ground state is of the $^2B_2$ character in the C_{2v} symmetry group (i.e., X^2B_2). The weak B-type band corresponds to the 1^2A_2 state, while the strong A-type transition results in the 2^2B_2 state. As follows from the MCSCF calculations, the ground X^2B_2 state is predominantly single-configurational with the radical $2b_2$ orbital being singly occupied. However, both 1^2A_2 and 2^2B_2 are two-configurational, with one excitation promoting electron from $1a_2$ or $1b_2$ to singly-occupied $2b_2$ and with the other excitation of almost the same weight promoting electron from $2b_2$ to either $2a_2$ or $3b_2$. The molecular orbital diagram and excitation amplitudes in Fig. 5.2 reflect the electronic structure of the α-MeBz radical as well, with the only significant difference that the C_{2v} symmetry is lifted to the C_s symmetry group, and both excited states belong to the A" type.

Not surprisingly, the low-correlated single-reference methods like CIS (see Ref. [72]) and TDDFT (our own preliminary calculations) also fail to produce a correct ordering of the excited states in benzyl and yield a D_1-D_2 energy splitting with significant error. EOM-EE-CCSD inverts the order of the D_1-D_2 states for benzyl, but gives the correct order in α-MeBz. On the other hand, the EOM-IP-CCSD method matches with the experiment for the benzyl radical, giving $D_0 \rightarrow D_1$ and $D_0 \rightarrow D_2$ transitions with the correct TDM direction, relative oscillator strength, and approximate energy splitting (see Table 5.3). While the agreement of EOM-IP-CCSD with the experiment is very encouraging, a care should be taken in applying single-reference methods to the benzyl radical and derivatives. For example, while EOM-EE-CCSD describes both important determinants for 1^2A_2 and 2^2B_2 as single excitations (see Fig. 5.2), the (open-shell) reference state is strongly spin-contaminated that

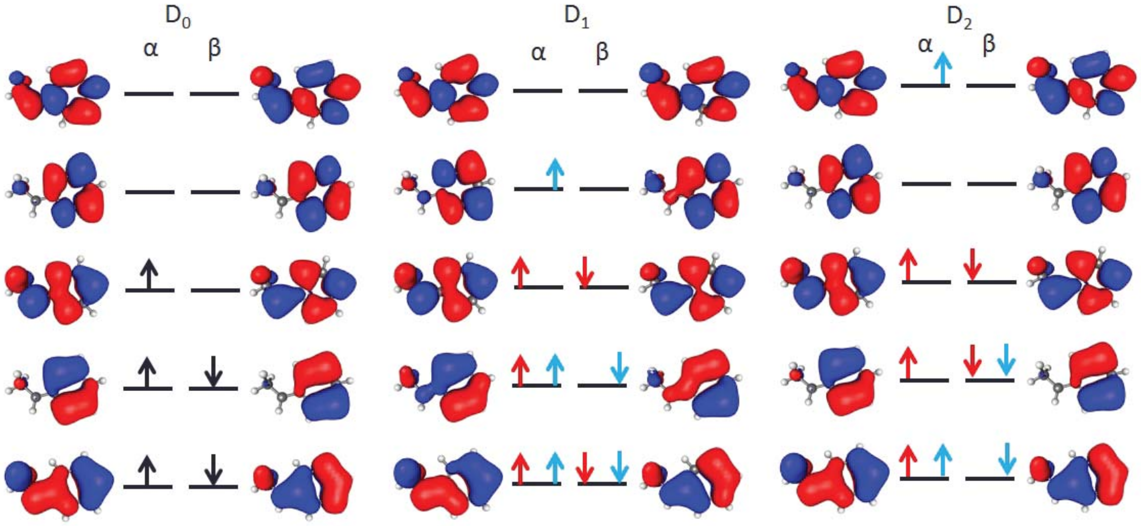

Figure 5.2. Orbitals comprising the D_0, D_1, and D_2 states of α-MeBz. The D_1 and D_2 states both have multi-reference character with both the blue and red determinants pictured contributing significantly to the state.

Table 5.2.

The Barrier Heights between the syn and anti conformations of the α-MeBz radical in the ground and first excited state. A positive value of the barrier means that the anti conformation is preferred. The rotation column indicates whether the method predicts methyl rotation between the ground and excited state.

Method	Geometry	D_0 barier (cm^-1)	D_1 barier (cm^-1)	rotation
IP-CISD aug-cc-pVDZ	IP-CISD aug-cc-pVDZ	-61	336	yes
EOM-IP-CCSD aug-cc-pVDZ	IP-CISD aug-cc-pVDZ	124	316	no
EOM-IP-CC(2,3) 6-31G(d)	IP-CISD aug-cc-pVDZ	185	294	no
(EOM-EE-)CCSD aug'-cc-pVDZ	(EOM-EE-)CCSD aug'-cc-pVDZ	146	377	yes
MCSCF cc-pVDZ	MCSCF 6-31G(d)	179	-123	yes
MCQDPT cc-pVDZ	MCSCF 6-31G(d)	166	-253	yes

Table 5.3.

Calculated properties of the D_1 and D_2 states of benzyl and α-MeBz radicals at the EOM-IP-CCSD/6-311+G(d,p) level of theory.

parameter	benzyl	α-methylbenzyl
$D_1\,(\mu_a^2 : \mu_b^2 : \mu_c^2)$	0:100:0	53:47:0
$D_2\,(\mu_a^2 : \mu_b^2 : \mu_c^2)$	100:0:0	99:1:0
$f_{D_1} : f_{D_2}$	0.0179:0.1218	0.0416:0.1030

might lead to a loss of accuracy in describing the excited states. [62] On the other hand, EOM-IP-CCSD (and all other ionization-potential methods employed in this work) may suffer from unbalanced treatment of two main electron transitions in 1^2A_2 and 2^2B_2. This is because when starting from the closed-shell anion reference with the doubly occupied $2b_2$ orbital, excitation of the β electron is formally described as a single "excitation" (i.e., annihilation of an electron) while excitation in the α space is a double excitation (annihilation of one electron and promotion of the other one). Thus, inclusion of triple excitations in EOM-IP is important for achieving quantitatively accurate results. On a positive note, both EOM-EE-CCSD and EOM-IP-CCSD, as well as configuration interaction version of the IP method, IP-CISD, have efficient analytic gradients that allows geometry optimizations of the ground and excited states.

Additional complexity in describing D_1/D_2 splittings arises due to non-adiabatic effects and vibronic interactions between these states. While investigating these topics is beyond a scope of the work described here, it is important to note that the vibronic couplings in α-MeBz are stronger and the adiabatic states are more mixed than the states in benzyl. This is because D_1 and D_2 belong to the same symmetry representation in α-MeBz and are allowed to mix, and because a presence of the methyl group rotates the TDM moments of D_1 and D_2 toward each other.

It was also found that the orientations and magnitudes of TDMs in α-MeBz are extremely sensitive to the electronic structure method, basis set, and the geometry of the molecule. Table 5.3 provides representative set of data comparing calculated properties of the D_1 and D_2 states in benzyl and α-MeBz. The EOM-IP-CCSD calculations predict greater oscillator strength (by 2.5 times) for the $D_0 \rightarrow D_1$ transition in α-MeBz than in benzyl. The D_2 state is predicted to be less than 500 cm^{-1} above D_1 in α-MeBz, and still carries a greater oscillator strength in its transition from D_0, with $f_{02} = 0.103$ compared to $f_{01} = 0.042$. As a result, it is somewhat surprising that the effects of vibronic coupling between D_1 and D_2 are not more readily apparent in the spectrum.

Taking into account the complexity of the electronic structure of α-MeBz and intrinsic problems of many computational methods in describing its electronic states, determining the preferred orientation of the methyl rotor in the ground and first excited states appears to be a challenging task. Table 5.2 summarizes the rotational barriers obtained at different levels of theory.

All methods except IP-CISD predict the ground state more stable in the anti geometry, with the rotation barrier between 120 and 230 cm^{-1}. Observing that the increase both in the basis set and in the correlation level lower the rotational barrier in D_0, the best computational estimate of the ground state barrier is 140-180 cm^{-1}. Rather misleadingly, IP-CISD in diffuse basis sets gives lower energy for the syn configuration. This suggests that even in the ground electronic state, the molecular structure is very sensitive to the level of theory employed.

All IP methods suggest that the anti conformation is preferred in the first excited state. However, this would imply that the methyl group is not rotated upon excitation that contradicts the experimental evidence. Additionally, the calculations with EOM-EE-CCSD and multi-configurational methods show that the syn conformation is lower in energy for the experimentally observed B-type state. As discussed above, the thought is that EOM-EE-CCSD provides a more balanced description of the excited states in α-MeBz than the IP methods do. Calculations at the ground state geometry with MCSCF and MCQDPT also provide a hint that the B-type state prefers the syn conformation; however, more precise analysis was not possible due to a failure of these methods to find the optimal geometry of the B-type state.

6. PHENYLCYANOMETHYL SIMULATIONS

This chapter will summarize simulations performed on the phenylcyanomethyl (PCN) radical. The purpose of these simulations is to identify the unknown peak in the experimental absorption spectrum. The specific peak in question is around 200 cm^{-1} above the $D_0 \rightarrow D_1$ transition, seen in 6.1.

Over the course of this project, many different explanations for this peak have been analyzed including Duchenski mixing between two out of plane vibrational modes, vibronic coupling to a near by S_2 state, and finally a double-welled potential energy surface in the S_1 state. The current hypothesis is that the excited state is non-planar, resulting in a double welled potential energy surface. This would allow for a ground state normal mode to have large overlap with both the $\nu = 0$ and $\nu = 2$ vibrational

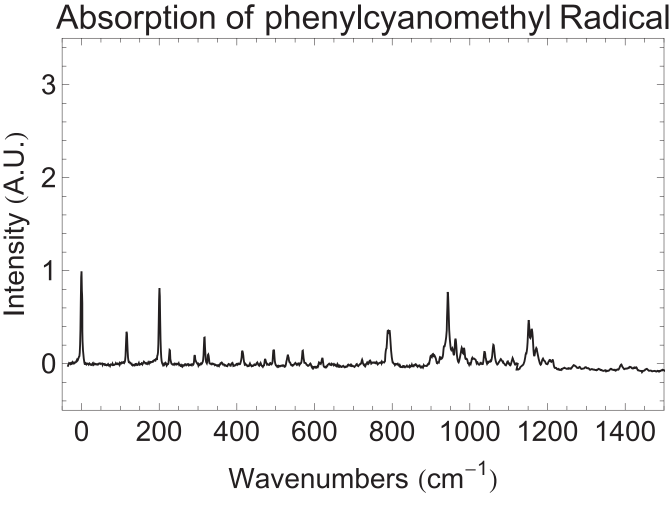

Figure 6.1. Absorption spectrum of the phenylcyanomethyl radical. The source of the intense peak 200 cm^{-1} over the origin is unknown.

states to a corresponding excited state normal mode. This will be elaborated on further in 6.2.1.

6.1 Ab-initio Calculations

Due to the complexities involved in simulating excited state radicals, two different ab-initio methods have been employed to investigate the nature of the $D_0 \rightarrow D_1$ transition. The first set of calculations use the EOM-IP-CCSD method with the 6-31G* basis set. This method was chosen because it treats the ground state as an electronically excited state by initially computing the wavefunction of the corresponding anion and then exciting a single electron to infinity. This allows for a more equal treatment of ground and excited state, and thus resulting in better transition energies and intensities. These calculations were performed with Q-Chem. [35]

The complete active space multi-configurational self consistent field (CASSCF) method was also used to explore the excited states of the PCN radical. This was done using the 6-31G* basis and the 11 electrons in 11 orbitals active space. The orbitals used in the active space are shown in Fig. 6.2. This method was chosen due to its accuracy and speed, as well as the fact it was used to study the similar molecule phenylpropargyl radical. [74] The initial CASSCF(11,11) calculations returned The results of both sets of calculations are summarized in Tables 6.1 and 6.2.

Since both ground and excited state geometries are required to compute the vibrational manifold off of the $D_0 \rightarrow D_1$ transition, both the ground and excited states of the PCN radical were optimized. Geometries, bond lengths, and the cyano-phenyl bond angle are reported for EOM-IP-CCSD in Fig. 6.3 and for CASSCF(11,11) in Fig. 6.4. Further, frequency calculations were performed on all geometries and used to construct Franck-Condon spectra reported in Section 6.2.

Based on previous calculations with the α-methylbenzyl radical and benzyl radical, as seen in Chapter 5, it is believed that the D_1 state that is observed experimentally should have a weak b-type transition. Based on the TDM values reported in 6.2, the

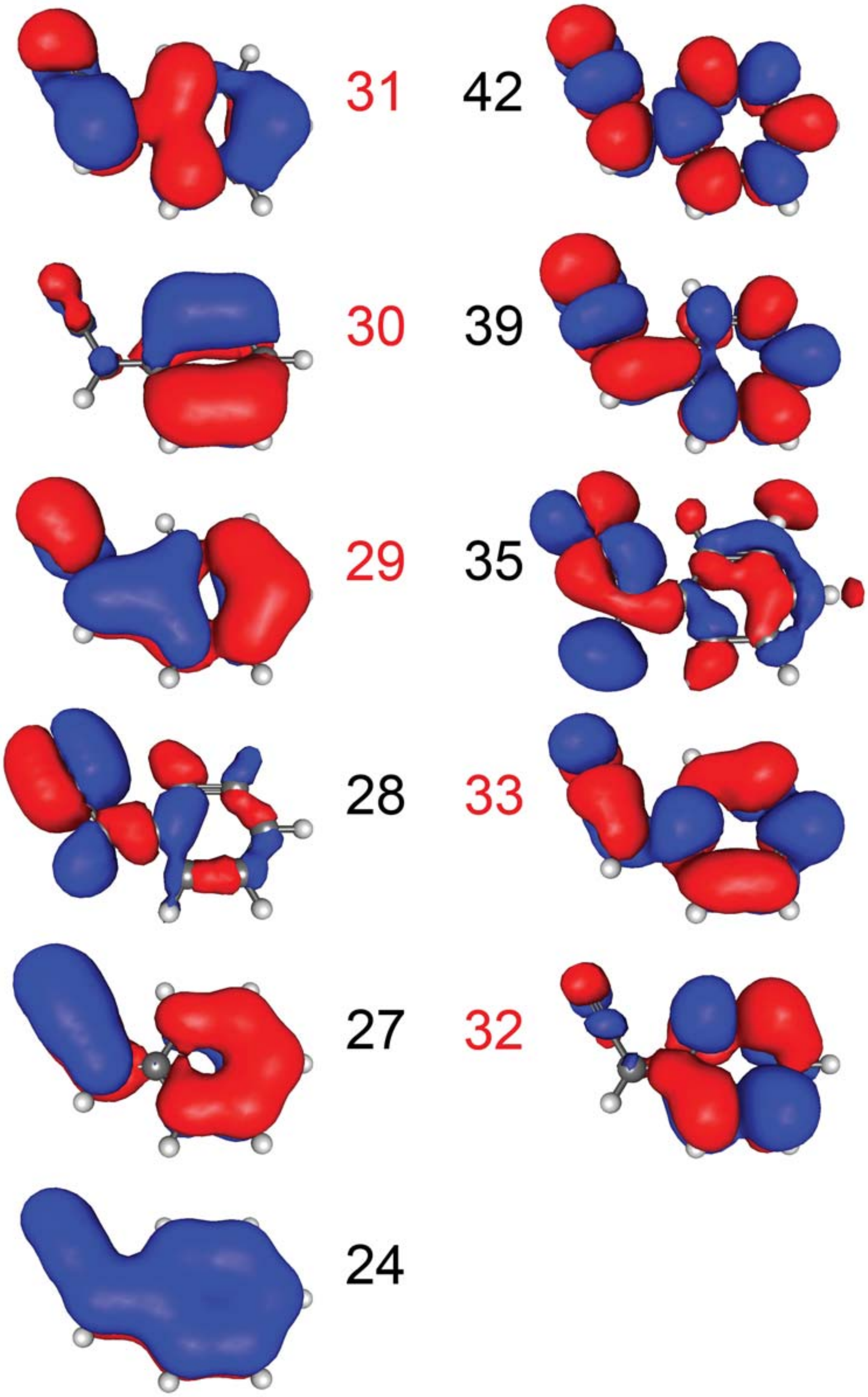

Figure 6.2. Orbitals included in the CASSCF(11,11) calculations.

Table 6.1.

Calculations performed on PCN radical. Many calculations predict that the D_1 and D_2 states are very close in energy. This results in an ambiguous ordering between the states. IP and OOP in the table correspond to whether the geometry is planar or non-planar. The CASPT2(11,11) calculations were performed at the CASSCF(11,11) geometries.

Method	State Optimized	D_0 Energy	D_1 Energy	D_2 Energy
EOM-IP-CCSD	D_0 IP	-362.083357	-361.951136	-361.946854
EOM-IP-CCSD	D_1 IP	-362.018443	-361.907920	-361.884295
EOM-IP-CCSD	D_1 OOP	-361.981249	-361.910110	-361.863170
CASSCF(11,11)	D_0 IP	-361.013674	-360.904781	-360.895801
CASSCF(11,11)	D_1 IP	-361.006970	-360.911730	-360.886697
CASSCF(11,11)	D_2 IP	-361.005747	-360.901473	-360.895144
CASPT2(11,11)	D_0 IP	-362.033393	-361.926475	-361.924000
CASPT2(11,11)	D_1 IP	-362.027659	-361.932295	-361.917350

Table 6.2.

Both the CASSCF(11,11) calculations agree that the first excited state primarily has a TDM direction along the a-axis. This is in disagreement with EOM-IP-CCSD methods which predict a TDM for D_1 along the b-axis. Based on similar molecules, it is believed that EOM-IP-CCSD obtains the correct state ordering.

Method	State Optimized	$D_0 \rightarrow D_1$ Direction	$D_0 \rightarrow D_1$ Strength	$D_0 \rightarrow D_2$ Direction	$D_0 \rightarrow D_2$ Strength
EOM-IP-CCSD	D_0	0.1:99.9:0.0	0.012	99.2:0.7:0.0	.236
EOM-IP-CCSD	D_1 IP	10.4:89.6:0.0	0.437	99.3:0.6:0.0	1.681
EOM-IP-CCSD	D_1 OOP	3.7:96.2:0.0	0.004	73.3:26.5:0.1	.139
CASSCF(11,11)	D_0	93.7:6.2:0.0	0.007	23.0:77.0:0.0	0.001
CASSCF(11,11)	D_1	94.0:6.0:0.0	0.006	24.7:75.3:0.0	0.001
CASSCF(11,11)	D_2	71.5:28.5:0.0	0.005	97.4:2.6:0.0	0.006

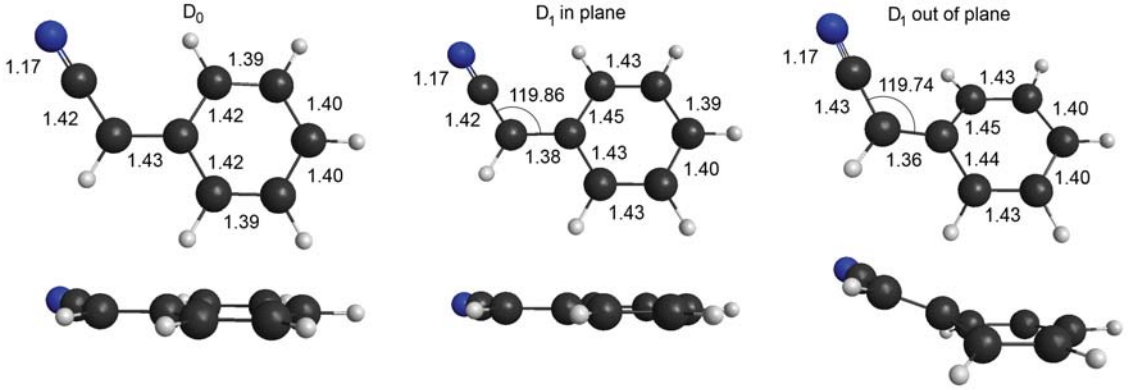

Figure 6.3. EOM-IP-CCSD minimum energy geometries for the D_0 state (left), in plane D_1 state (middle), and the out of plane D_1 state (right).

EOM-IP-CCSD calculations appear to obtain the correct state ordering for both the D_0 and in plane D_1 optimized geometry. The out of plane D_1 optimized geometry has an ambiguous state ordering due to the mixing between TDM intensity and direction, though it could very likely be that this is the D_2 state that is partly mixed with the D_1 state after passing through a conical intersection.

In order to compute the vibrational manifold off of the $D_0 \rightarrow D_1$ transition, While CASSCF calculations predict a planar geometry for each state and EOM-IP-CCSD predicts a planar geometry for the ground state, EOM-IP-CCSD found a minimum in energy for the D_1 state in both the planar (IP) geometry and an out of plane geometry (OOP). This is likely due to the fact that EOM-IP-CCSD predicts a state ordering different that that of the CASSCF methods based on TDM direction 6.2. The minimum of the correct EOM-IP-CCSD state is at the out of plane geometry, as depicted in Fig. 6.3.

6.2 Franck-Condon Spectra

Frequency calculations at the geometries listed in Table 6.1 were then used to construct FC-spectra with the program EZ-Spectrum, [36] which could then be com-

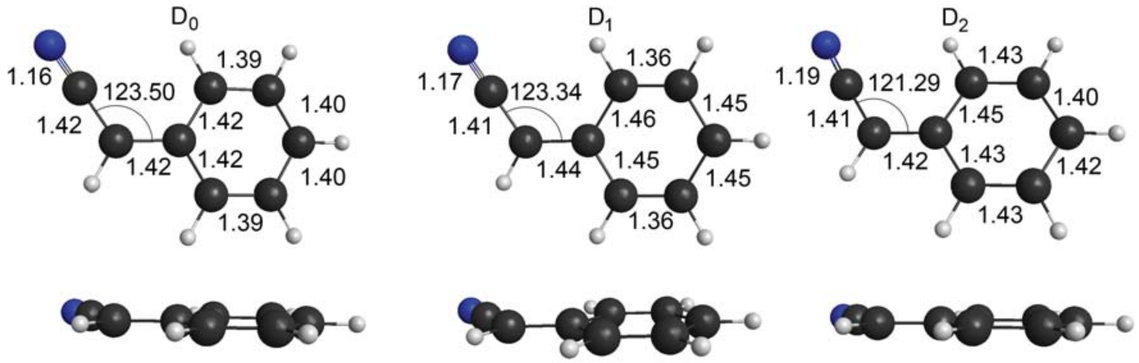

Figure 6.4. CASSCF(11,11) minimum energy geometries for the D$_0$ (left), D$_1$ (middle), and D$_2$ (right) states.

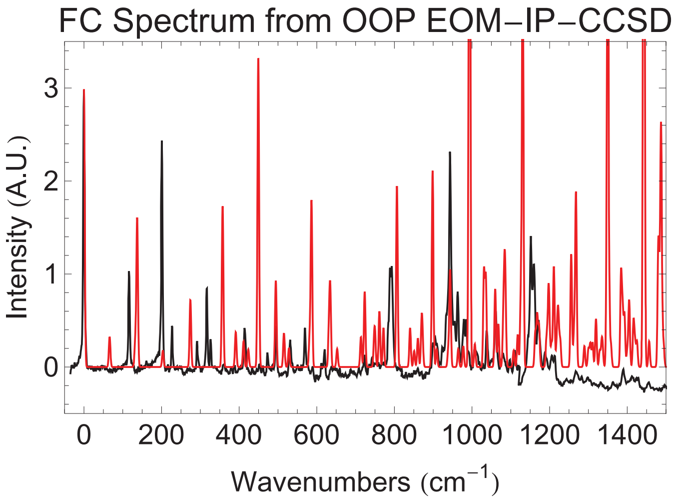

Figure 6.5. Franck-Condon absorption spectrum calculated between the ground state planar geometry and the D$_1$ state out of plane geometry (red trace).

pared to the experimental lineshape. The predicted spectrum from the out of plane EOM-IP-CCSD D$_1$ state and the EOM-IP-CCSD D$_0$ state is shown in Fig. 6.5. Due to the extremely large geometry change depicted in 6.3, the resulting predicted spectrum has many vibrational modes showing much to large intensity. The FC spectrum resulting from the in plane EOM-IP-CCSD D$_1$ geometry, shown in Fig. 6.5shows no better agreement with experiment, though the peaks are not as anomalously large. This leads to the conclusion that, although the EOM-IP-CCSD calculations appear to get the state ordering correct, they fail to produce reasonable geometries for the PCN radical.

The same FC calculations were performed with CASSCF(11,11) from the D$_0$ state to the D$_1$ state (Fig. 6.7 and to the D$_2$ state (Fig. 6.8). While the calculation to the D$_1$ state misses completely the intensity in the low frequency calculations, it is able to obtain some of the higher frequency peaks. Likely, the peak near 1175 cm^{-1} is due to the peak at 960 cm^{-1} convoluting with the unknown 200 cm^{-1} peak, which is completely missed. The calculation to the D$_2$ state shows little correspondence to

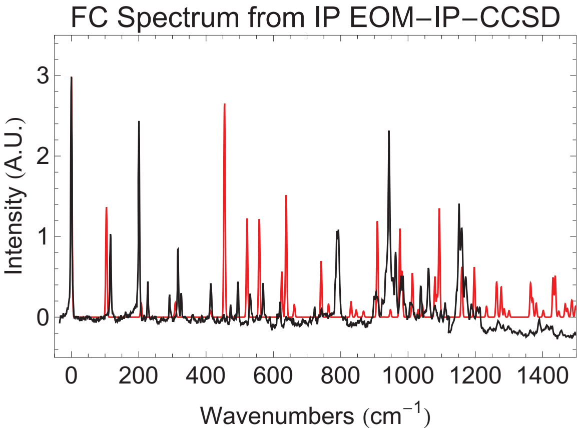

Figure 6.6. Franck-Condon absorption spectrum calculated between the ground state planar geometry and the D_1 state geometry constrained to be planar.

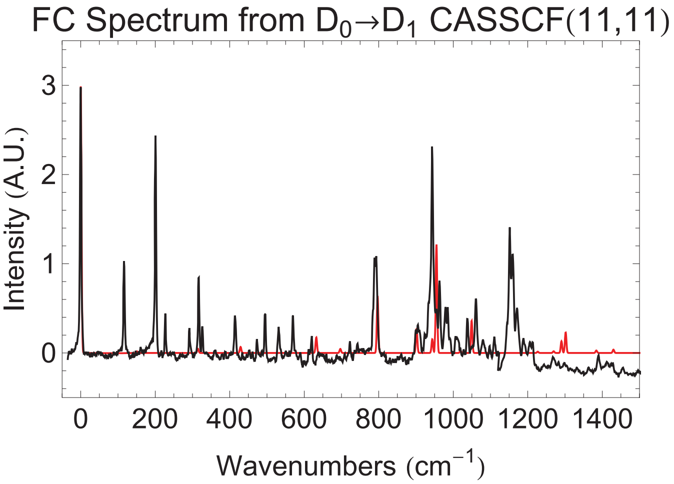

Figure 6.7. Absorption $D_0 \rightarrow D_1$ absorption spectrum from CASSCF(11,11) geometries and frequencies.

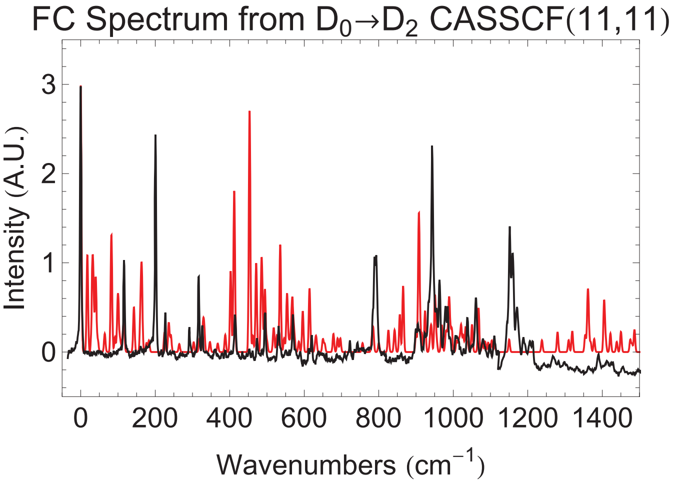

Figure 6.8. Absorption $D_0 \rightarrow D_2$ absorption spectrum from CASSCF(11,11) geometries and frequencies.

the observed spectrum. This suggests that the computed D_1 state is closer to the actual excited state geometry.

6.2.1 Ab-initio Potential Energy Surface with EOM-IP-CCSD Calculations.

In order to test the hypothosis that the out of plane nature of the D_1 state causes the unknown peak at 200 cm^{-1}, the potential energy surface of the D_1 state was constructed between the optimized D_0 and out of plane D_1 geometries (Fig. 6.9). After constructing the potential energy surface of the D_1 state at a resolution of .1Å, a fourth order polynomial interpolation algorithm was used to construct a surface at a resolution of 0.0005Å. After constructing the fine surface, the Schrödinger equation was numerically integrated over the symmetric D_1 potential energy surface along the out of plane coordinate. By changing the boundary conditions at 0 displacement, it is possible to find all vibrational states for the given potential energy surface. These are then plotted in Fig. 6.9.

By finding the overlap between these wavefunctions and the ground state vibrational wavefunction it is possible to determine the Franck-Condon factor for the $0 \rightarrow 0$ and $0 \rightarrow 2$ vibrational transitions. Unfortunatly, because the computed barrier is so wide, neither transition is predicted to have any applicable intensity. This is due to the magnitude of the out of plane motion, as can be seen in Fig. 6.3. In order to conclude with greater certanty that the out of plane vibration is not responsible for the 200 cm^{-1} peak, a CASSCF potential energy surface needs to be computed.

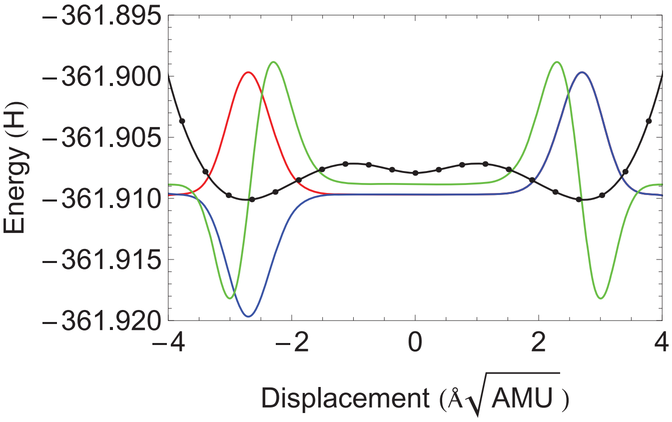

Figure 6.9. EOM-IP-CCSD potential energy surface constructed by linear displacement from planar D_0 geometry to out of plane D_1 geometry (black). The dots are computed points while the line is the interpolated potential. The red, blue, and green traces are the ground, first, and second vibrational wavefunctions along this potential.

7. ULTRAFAST RADIATONLESS DECAY IN THE PHOTOACID 3-CYANO-6-HYDROXYCOUMARIN

In this chapter the ultrafast radiationless decay of the photoacid 3-cyano-6-hydroxycoumarin is investigated.

7.1 Computational Methods

Calculations to determine an optimal method for large-scale condensed-phase calculations are performed for CHCM-water cluster with CIS(D), EOM-EE-CCSD (briefly EOM-CCSD), and TD-DFT with B3LYP and PBE0 functionals on a 6-31+G* basis. Additionally, the basis set dependence on excitation energies was investigated at the PBE0 level in 6-31+G*, 6-311++G**, and aug-cc-pVTZ. To facilitate these comparisons, all calculations were performed at the PBE0/6-31+G* optimized geometry. [35]

Two different solvation models are employed over the course of this work. The Polarizable Continuum Model (PCM), an implicit solvent model, is used with default parameters for water solvent. Additionally, an explicit polarizable solvent mode, the general Effective Fragment Potential method, is employed. For the EFP calculations, parameters for CHCM and COCM$^-$ were obtained in GAMESS using MAKEFPruns. The 6-31+G* basis was used for obtaining electrostatic parameters and 6-311++G(3df,2p) for parameters of all other terms. A standard water potential from a fragment library was used. CHCM or COCM$^-$ was placed in a 22 box with periodic boundary conditions, to which water molecules were added using the GROMACS solvate box command. The EFPMD module of libefp open-source EFP software was used for molecular dynamics simulations. [75] A 1 fs timestep and switching functions for all EFP terms were used. The following equilibration sequence was used: (i) geometry optimization with turned-off polarization, (ii) geometry optimization with polarization turned on, (iii) 10 ps run in an NVT ensemble at 300 K after assigning velocities from a Boltzman distribution. After equilibration, a 10ps NVTrun was performed, with 8 geometries pulled at 1.25 ps separations. For each frame, velocities were reassigned from a Boltzman distribution at 300K and each of the 8 geometries was re-equilibrated using the same scheme as described above. After equilibration, NVT production runs of 10 ps were run on each of the 8 systems. From these runs, 32 frames were selected with a minimum separation of 0.09 ps (90 fs) where hydrogen bonding was observed between a water molecule and either the hydroxy group of CHCM or exposed oxygen on $COCM^-$. These 64 geometries, 32 for each of CHCM and $COCM^-$, were used for the calculations exploring proton transfer pathways and absorption spectra in water solvent.

In order to validate computational methodology, B3LYP and PBE0 TD-DFT and CIS(D) excited state calculations for CHCM-water complex were compared against an EOM-CCSD calculation in 6-31+G* basis set. The results are presented in Table 7.1. Electronic states are characterized by a leading transition; involved orbitals are shown in Fig. 7.5. CIS(D) excitation energies are within 0.2 eV from the EOM-CCSD benchmark, and the order of first five states is preserved. PBE0 and B3LYP excitation energies are systematically lower than the EOM-CCSD ones, by 0.3-0.7 eV in case of PBE0 and 0.4-0.9 eV in case of B3LYP. Additionally, B3LYP calculations reverse the fourth and fifth excited states, as can be seen from the values of the transition dipole moments and verified by the orbitals. Even more importantly, the energy difference between the first and fifth excited states is underestimated by B3LYP by 0.5 eV with respect to EOM-CCSD. The first and fifth states are the two most important states for understanding non-adiabatic dynamics of CHCM. Based on these observations, B3LYP was excluded from further consideration. On the other hand,

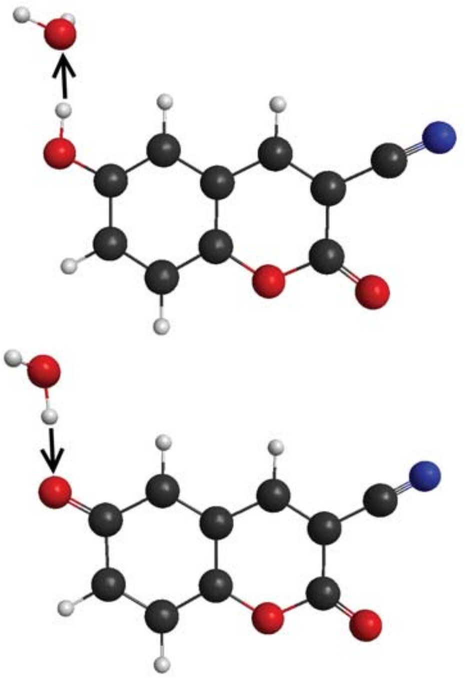

Figure 7.1. Proton transfer to solvent in CHCM (top) and back-protonation in COCM$^-$ (bottom).

both CIS(D) and PBE0 accurately describe energy difference between the first and fifth states, with corresponding discrepancies of < 0.1 eV and < 0.2 eV with respect to EOM-CCSD. However, CIS(D) is not currently implemented with PCM polarizable model in available to us electronic structure software, so it could not be used for all the modeling necessary for this work. This left PBE0/6-31+G* as the optimal methodology to investigate excited state proton transfer in CHCM in solvent.

A simple model for transferring a proton between solvent and solute was used. From the starting geometry, which is an optimized geometry of CHCM-water dimer in the case of PCM and gas phase calculations, or a geometry of CHCM-water dimer extracted from a frame of EFP MD in the case of QM/EFP calculations, the hydrogen atom from CHCM hydroxyl group was linearly displaced along the vector pointing the water oxygen until the distance between the two becomes .94 Å (Fig. 7.1). The proton transfer pathway was broken up into 10 increments totaling 9 equidistant intermediate

Table 7.1.

Excitation energy (in eV) and oscillator strengths (in parenthesis) of electronic transitions in CHCM hydrogen bonded to a single water molecule.

	Character	PBE0	B3LYP	CIS(D)	EOM-CCSD
State 1	53 ⇒ 1	3.498 (0.119)	3.385 (0.106)	3.835 (0.429)	3.828 (0.149)
State 2	51 ⇒ 1	4.460 (0.000)	4.308 (0.000)	5.075 (0.000)	5.137 (0.000)
State 3	52 ⇒ 1	4.529 (0.479)	4.421 (0.465)	4.693 (0.250)	4.875 (0.336)
State 4	53 ⇒ 2	5.223 (0.017)	5.057 (0.013)	5.790 (0.012)	5.634 (0.112)
State 5	53 ⇒ 3	5.346 (0.000)	4.934 (0.000)	5.918 (0.003)	5.859 (0.000)

positions, a beginning point, and an ending point. Excited state calculations were performed at these points to construct the excited state proton transfer curves.

The back-protonation mechanism was investigated similarly. In this case, a starting structure was the $COCM^-$ anion and H-bonded water molecule; the final structure was neutral CHCM and HO^-.

Dependence of excitation energies on basis set size is shown in 7.2. TD-DFT PBE0 calculations with the 6-31+G*, 6-311++G**, and aug-cc-pVTZ basis sets show that the excitation energies have little dependence on basis set, changing by less than .05 eV. This observation allows us to safely use the smaller 6-31+G* basis for all calculations in this study.

7.2 Absorption Properties

Experimental linear absorption spectra are compared to calculated absorption spectra of CHCM (Fig. 7.2) and $COCM^-$(Fig. 7.3). All calculations treat the CHCM or $COCM^-$ molecule and a single hydrogen-bonded water quantum-mechanically. As only a single geometry is used in the PCM and gas phase calculations, the resulting spectrum has a stick form. Conversely, sampling of solvent configurations is accounted

Table 7.2.

PBE0 excitation energies(eV) of the first three excited states of CHCM in 6-31+G*, 6-311++G**, and aug-cc-pVTZ basis sets.

	6-31+G*	6-311++G**	aug-cc-pVTZ
S1	3.498	3.477	3.462
S2	4.460	4.433	4.420
S3	4.529	4.505	4.489
number of basis functions	299	379	851

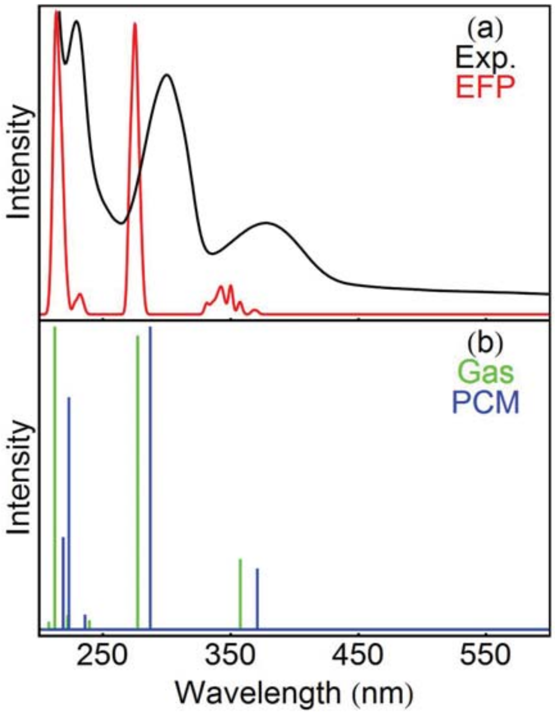

Figure 7.2. Absorption spectra of CHCM.(a) Experimental spectrum in methanol / water 1/1 v/v at pH 6.5 (black) and calculated with PBE0/EFP (red), (b) calculated with PBE0/PCM (blue) and a gas phase PBE0 calculation (green).

for in PBE0/EFP calculations, such that a set of distinct transition energy and intensity data is obtained. These sets of transition data are blurred using Gaussians with a width of 5 nm and summed to produce the spectra seen in frame (b) of Figs. 7.2 and 7.3.

For the neutral species, the gas phase PBE0 calculations produce a spectrum in surprisingly good agreement with experiment. All three of the lowest energy absorption bands are well replicated. Both solvation methods also provide good agreement to the experimental spectrum, though the EFP spectrum is slightly blue shifted in comparison to both the experimental spectrum and the PCM method. Interestingly, the electrostatic component of the EFP water potential produces a blue solvatochromic shift, while the polarization component both in EFP and PCM causes a red shift. In case of EFP, this polarization-induced shift is smaller in magnitude than the shift due to electrostatics. As a result, PCM and EFP solvent models predict shifts of different signs, even though the absolute values of these shifts are small enough to ignore these peculiar discrepancies.

The calculated gas phase spectra of $COCM^-$ are in much worse agreement with experiment than in the neutral case. This indicates that solvent effects become more important when the molecule is charged. Both EFP and PCM solvent methods improve the agreement with the experimental spectra. However, by construction, PCM does not account for inhomogeneous broadening of the spectral lines due to different solvent configurations. As anions interact more strongly with the polar water solvent, broadening becomes more pronounced in the anion than in the neutral spectra. Thus, PCM becomes less reliable in describing solvated anion species. Conversely, the EFP model nicely describes line-broadening and overall provides a very nice agreement with experimental absorption spectrum.

7.3 Conical intersections in CHCM

In this section we investigate excited state proton transfer (ESPT) in CHCM using theoretical methodology justified in the previous sections. As experimental transient absorption spectra reveal, the excited state of deprotonated chromophore is quenched quickly. Thus, we consider a well-known mechanism of fluorescence quenching, [76] in which the bright excited state experiences a conical intersection with a dark state along a proton transfer pathway. Following the procedure detailed in Computational Detail section, we obtain electronic excited state energies by linearly displacing the proton from the $CHCM+H_2O$ to the $COCM^-+H_3O^+$ geometry. These plots are shown in Fig. 7.4. Indeed, the gas phase calculations, shown in frame (a), indicate that a conical intersection between the first bright excited state, corresponding to 380 nm peak in absorption spectrum and state 1 in Table 7.1, and a dark state occurs around 80% completion of the proton transfer process. This dark state corresponds to State 5 in Table 7.1. However, when solvent models are used, as shown in frames

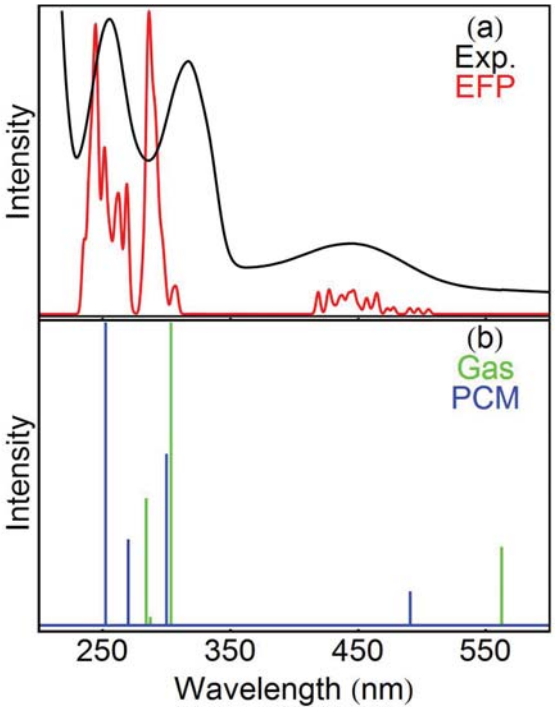

Figure 7.3. Absorption spectra of deprotonated COCM^{-}. (a) Experimental spectrum in methanol / water 1/1 v/v at pH 9.4 (black) and calculated with PBE0/EFP (red), (b) calculated with PBE0/PCM (blue) and from a gas phase PBE0 calculation (green).

(b) and (c) of Fig. 7.4, no conical intersection is observed. Both PCM and EFP solvation models return the same result, suggesting that this effect is not an anomaly.

A failure to observe a decrease in energy for the $\pi\pi^*$ state (red state in Fig. 7.4) along the proton transfer coordinate is slightly troubling, because it indicates that the excited state proton transfer process is not enthalpically favored even though the process is known to be spontaneous. Two additional considerations must also be taken into account however. First, there will also be an entropic contribution to free energy which will almost certainly favor the $\mathrm{COCM}^-{+}\mathrm{H_3O^+}$ state. Second, the surfaces were not relaxed geometrically, which is to say that the end point configuration has not had the $\pi\pi^*$ orbital reduced to the lowest energy geometry. This is likely why the PCM calculation shows a smaller gain in energy for the $\pi\pi^*$ state along the proton transfer coordinate, because in these calculations the solvent degrees of freedom were allowed to relax. The purpose of these calculations was not to determine spontaneity of the proton transfer process but instead to see if certain states would cross, providing a possible explanation for the de-excitation of the photoacid.

In order to rationalize disappearance of the conical intersection in solvent, the dipole moments of the various electronic excited states are shown in Fig. 9d. It is generally understood that polar solvents stabilize polar electronic states, i.e., the states that exhibit large static dipole moments. As seen in frame (d) of Fig. 7.4, the dipole moment of the dark state decreases significantly along the proton transfer coordinate, while the dipole moments of the ground and bright states grow monotonically. As a result, the water solvent destabilizes the dark state with respect to the ground and bright states as the proton is transferred further from CHCM to adjacent water. This destabilization of the dark state by solvent makes it too high in energy to reach the conical intersection with the bright state. A similar effect was discovered by Sobolewski and Domcke in their simulations of phenol as the number of (quantum) solvent molecules was increased. Thus, effect of micro-solvation on conical intersections was discussed in Ref. [77], while here we analyze the effect of macro-solvation.

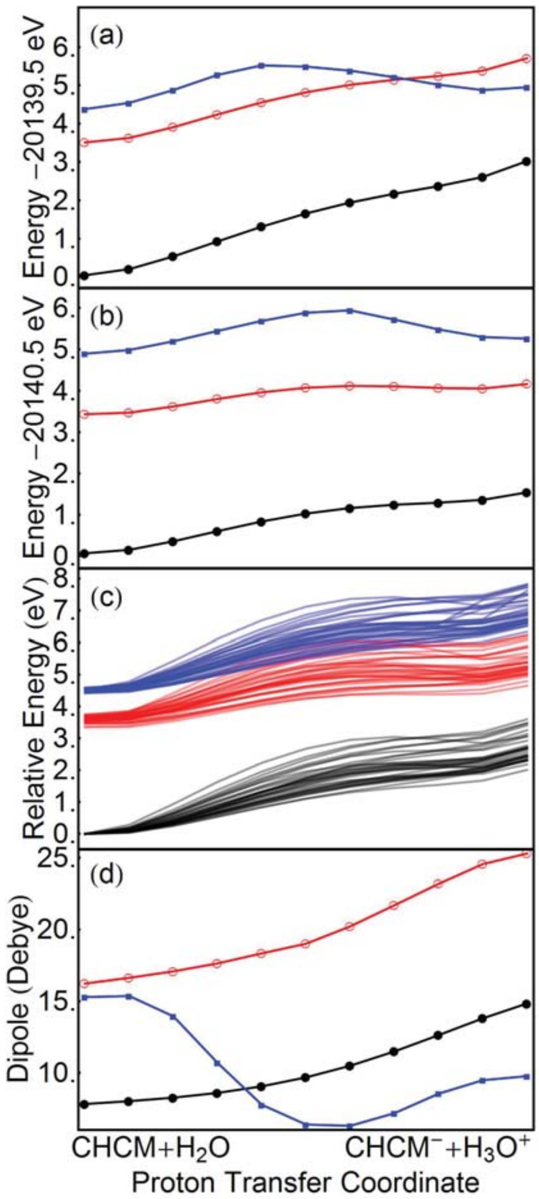

Figure 7.4. Electronic state energy for gas (a), PCM (b), and EFP (c) calculations as well as gas phase dipole moment (d) as a function of proton transfer to solvent coordinate for CHCM+H_2O→$CHCM^-$+H_3O^+. The black trace (filled circle) is the ground state, red trace (open circle) first excited (bright) state, blue trace (filled square) second excited (dark) state. Orbital diagrams for both the first and last molecular configurations are shown in Fig. 7.1. While a conical intersection is observed between the first and second electronic states in the gas phase, no similar conical intersection is observed for the other states.

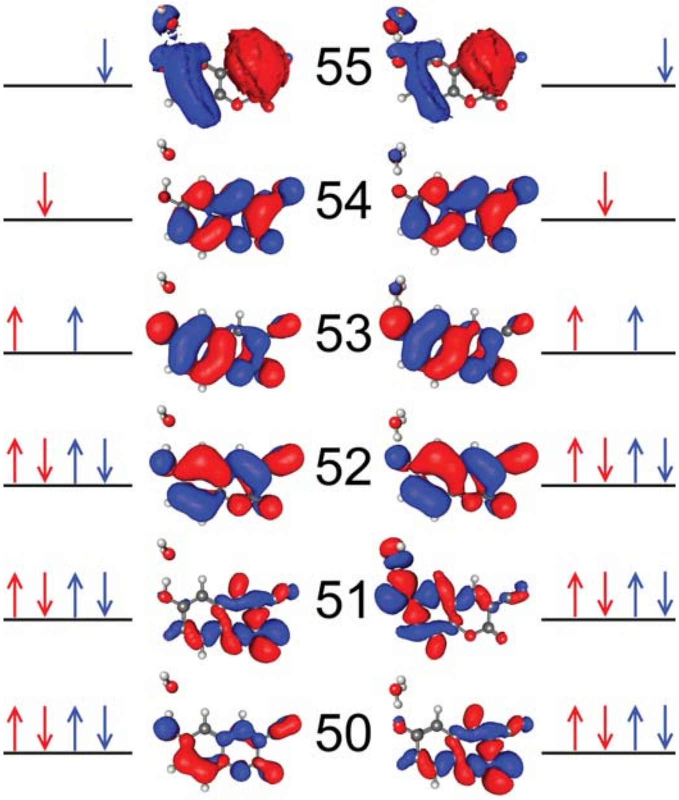

Figure 7.5. Orbitals for neutral CHCM with H_2O from the first and last steps of Fig. 7.4. The colors of the electron configurations corresponds to the state plotted seen in Fig. 7.4. Further, the red electron configuration is state 1 and the blue electron configuration is state 5 in Table 7.1. State 1 has a non-zero transition dipole moment and is seen in Fig. 7.2 around 350 nm, while state 5 is spectroscopically dark.

A failure to observe a conical intersection in CHCM+H_2O complex in solution over the course of proton transfer necessitates another look at the experimental data. Indeed, analyzing the excremental data, there appear to be two distinct time scales involved in the transient absorption spectra. The first occurs in a matter of a few ps, as the peaks at 510 and 550 nm grow in. Then over a longer 40 ps time scale, the transient absorption decays to that of the ground state anion. Since the 510 and 550 nm peaks are attributed to the absorption of the excited state anion, this time dependence can mean that the proton transfer reaction is decoupled from de-excitation of the chromophore. Thus we consider the possibility of non-radiative decay of excited state of CHCM after proton transfer is complete.

7.4 Conical Intersections in $COCM^-$

A possible alternative explanation for de-excitation of $COCM^-$ in protic solvents is that an elongated vibration on a water molecule hydrogen-bonded coordinate to the bare and negatively charged oxygen atom in $COCM^-$ could induce a conical intersection between the bright and dark excited states. This mechanism can be also referred to as "back-protonation". Indeed, this explanation is in accord with the experimental data because when the deprotonated form of the photoacid is excited, it still decays with an approximate lifetime of 40 ps, even though there is no proton to detach. Additionally, this mechanism is consistent with the data, which indicates that the de-excitation mechanism must be related to the presence of the hydroxyl group on the coumarin dye.

The hypothesis of de-excitation of $COCM^-$ via back-protonation is examined similarly to our approach for analysis of proton transfer, by linearly displacing a proton from a water molecule hydrogen bonded to the bare oxygen atom of the deprotonated $COCM^-$ anion. This model assumes that the proton accepted by a water molecule during ESPT is diffused into solvent and does not remain near $COCM^-$ anion.

The dependence of the excitation energies on proton transfer coordinate is shown in Fig. 7.6. These plots suggest that as the proton moves from the water molecule to $COCM^-$ anion, a conical intersection occurs in the gas phase (frame (a) of Fig. 7.6) and in 31 of 32 EFP trajectories (frame (c) of Fig. 7.6). The PCM trajectory shows a conical intersection at the very endpoint (frame (c) of Fig. 7.6). Thus, these data suggest that a conical intersection is probable in a back-protonation reaction.

The reason a conical intersection appears in the elongated vibration case, while not in the proton transfer reaction, is due to the character of the involved states. The low-lying dark state in elongated vibration mechanism is indeed a different state than the state considered for forward proton transfer. Molecular orbitals characterizing the former dark state are shown in Fig. 7.7. Importantly, in contrast to the dark state considered in the direct proton transfer mechanism, the dark state in the back-protonation mechanism has a large static dipole moment, as shown in frame d of Fig. 7.6. Thus, solvent stabilizes both the dark and bright states, such that the gas-phase picture remains valid. These observations suggest that the elongated hydrogen vibration is a possible explanation for the de-excitation of $COCM^-$ anion in protic solvent.

7.5 Conclusions

The photochemistry of 3-cyano-6-hydroxycoumarin (CHCM) is investigated with steady-state and time-resolved absorption and emission spectroscopy and electronic structure calculations. Transient absorption spectra reveal that electronically-excited CHCM in the presence of the proton accepting solvents deprotonates, with a characteristic times of 0.28 ns in MeOH and 6.5 ps in MeCN/water 1/1 v/v, accounting for the partial or total quenching of the CHCM emission in these solvents. Thus, CHCM can be classified as a photoacid. However, the excited anion produced in this reaction appears totally non fluorescent and has a finite lifetime of about 40 ps in MeCN/water 1/1 v/v. Decay of the anion excited state is a generally undesirable

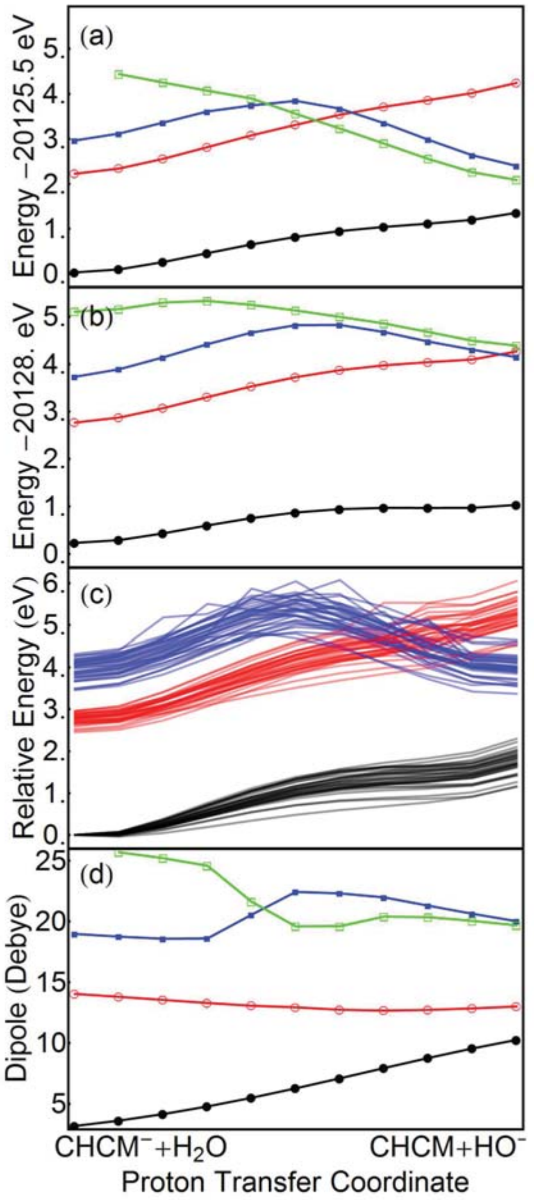

Figure 7.6. Electronic state energy for gas (a), PCM (b), and EFP (c) calculations as well as gas phase dipole moment (d) as a function of proton transfer to solvent coordinate for CHCM$^-$+H$_2$O$\rightarrow$CHCM+OH$^-$. The black trace (filled circle) is the ground state, red trace (open circle) first excited (bright) state, blue trace (filled square) second excited (dark) state, and green trace (open square) third excited (dark) state. Here, a conical intersection is observed between the first and dark excited states in the gas phase. In the PCM calculation only the lower of the two dark states is observed to cross with the first excited state. Finally, in 31 of 32 EFP calculations a conical intersection is also observed between the first excited and lower energy dark states.

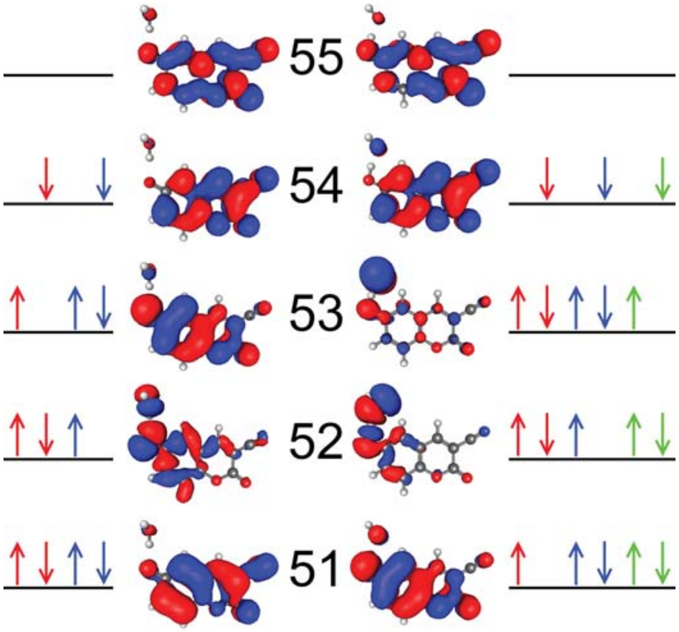

Figure 7.7. Orbitals for $COCM^{-}+H_2O \rightarrow CHCM+OH^{-}$ in the gas phase from the first and last steps of 7.3. The colors of the electron configurations corresponds to the state plotted seen in 7.3. The blue and green states have low transition dipole moments with the ground state, so would not be spectroscopically visible.

process for a photoacid, since it limits its potential applications. Indeed, once the deprotonated photoacid decays back to the ground state, the molecule becomes a strong conjugate base and re-captures the donated proton. As expected, upon replacement of the hydroxy group with a methoxy group, the CHCM excited state is long-lived and strongly fluorescent in all solvents.

In order to understand photo-dynamics of CHCM, specifically the observation that fluorescence is quenched upon excited-state proton transfer, gas phase and condensed phase electronic structure calculations are performed. Excited state calculations of CHCM-water complex reveal that TD-DFT with PBE0 functional in 6-31+G* basis provides sufficient accuracy in describing five lowest electronic transitions. The proton transfer reaction is modeled by a linear displacement of proton from hydroxyl group of CHCM toward hydrogen-bonded water. The gas phase calculations along the proton transfer coordinate show a conical intersection between the bright excited state and a higher-lying dark state. However, when solvent effects are introduced either implicitly with PCM or explicitly with QM/EFP, the conical intersection no longer appears. This is attributed to the static dipole moment of the dark state being smaller than that of the bright state, causing solvent to destabilize the dark state, increasing the energy gap between the two states and preventing the conical intersection between them. This result predicts that direct proton transfer-induced de-excitation does not occur, which is in agreement with the experimental evidence that the anion excited state is efficiently populated.

REFERENCES

REFERENCES

[1] M. Born and R. Oppenheimer. Quantum theory of molecules. *Annals of Physics*, 84:0457–0484, 1927.

[2] G. A. Worth and L. S. Cederbaum. Beyond born-oppenheimer: Molecular dynamics through a conical intersection. *Annual Revews of Physical Chemistry*, 55:127–158, 2004.

[3] J. C. Tully. Nonadiabatic molecular dynamics. *International Journal of Quantum Chemistry*, 40:299–309, 1991.

[4] P. Ehrenfest. Bemerkung über die angenäherte gültigkeit der klassischen mechanik innerhalb der quantenmechanik. *Zeitschrift Fur Physik B-Condensed Matter*, 45:455–457, 1927.

[5] H. D. Meyera and W. H. Miller. A classical analog for electronic degrees of freedom in nonadiabatic collision processes. *Journal of Chemical Physics*, 70(7):3214–3223, 1979.

[6] U. Manthe, H.-D. Meyer, and L. S. Cederbaum. Wave-packet dynamics within the multiconfiguration hartree framework: General aspects and application to noci. *Journal of Chemical Physics*, 97:3199–3213, 1992.

[7] R. Kosloff. Time-dependent quantum-mechanical methods for molecular dynamics. *Journal of Physical Chemistry*, 92:2087–2100, 1988.

[8] R. L. Fulton. Vibronic interactions. the adiabatic approximation. *Journal of Chemical Physics*, 56(3):1210–1218, 1970.

[9] R. L. Fulton and M. Gouterman. Vibronic coupling i. mathematical treatment for two electronic states. *Journal of Chemical Physics*, 35(5):1059, 1961.

[10] A. Witkowski. Coupling of the molecular exciton with the nuclear vibrations. In Oktay Sinanoğlu, editor, *Modern Quantum Chemistry*, volume III. Academic Press, New York, 1965.

[11] P. Petelenz and M. Andrzejak. Vibronic interpretation of the low-energy absorption spectrum of the sexithiophene single crystal. *Journal of Chemical Physics*, 113:11306–11314, 2000.

[12] K. Sakota and H. Sekiya. Excited-state double-proton transfer in the 7-azaindole dimer in the gas phase. 1. evidence of complete localization in the lowest excited electronic state of asymmetric isotopomers. *Journal of Physical Chemistry A*, 109(12):2718–2721, 2005.

[13] M. Andrzejak and P. Petelenz. Vibronic coupling in dimer - a convenient approximation revisited. *Chemical Physics*, 335:155–163, 2007.

[14] P. Ottiger, S. Leutwyler, and H. K oppel. S_1/s_2 excitonic splittings and vibronic coupling in the excited state of the jet-cooled 2-aminopyridine dimer. *Journal of Chemical Physics*, 131:204308, 2009.

[15] C. G. Heid, P. Ottiger, R. Leist, and S. Leutwyler. The s_1/s_2 exciton interaction in 2-pyridone·6-methyl-2-pyridone: Davydov splitting, vibronic coupling, and vibronic quenching. *Journal of Chemical Physics*, 135:154311, 2011.

[16] C. P. Rodrigo, C. W. Müller, N. R. Pillsbury, H. J. III William, D. F. Plusquellic, and T. S. Zwier. Conformer-specific vibronic spectroscopy and vibronic coupling in a flexible bichromophore: Bis-(4-hydroxyphenyl)methane. *Journal of Chemical Physics*, 134:164312, 2011.

[17] A. M. Kelley. A multimode vibronic treatment of absorption, resonance raman, and hyper-rayleigh scattering of excitonically coupled molecular dimers. *Journal of Chemical Physics*, 119(6):3320–3331, 2003.

[18] J. Guthmuller, F. Zutterman, and B. Champagne. Prediction of vibronic coupling and absorption spectra of dimers from time-dependent density functional theory: The case of a stacked streptocyanine. *Journal of Chemical Theory and Computation*, 4(12):2094–2100, 2008.

[19] J. Guthmuller, F. Zutterman, and B. Champagne. Multimode simulation of dimer absorption spectra from first principles calculations: Application to the 3,4,9,10-perylenetetracarboxylic diimide dimer. *Journal of Chemical Physics*, 131(15), 2009.

[20] J. Seibt, V. Dehm, F. Wuerthner, and V. Engel. Absorption spectroscopy of molecular trimers. *Journal of Chemical Physics*, 126(16), 2007.

[21] F. C. Spano and L. Silvestri. Multiple mode exciton-vibrational coupling in h-aggregates: Synergistic enhancement of the quantum yield. *Journal of Chemical Physics*, 132(9):094704, 2010.

[22] C. Woywod, W. Domcke, A. L. Sobolewski, and H. J. Werner. Characterization of the s_1-s_2 conical intersection in pyrazine using *ab initio* multiconfiguration self-consistent-field and multireference configuration-interaction methods. *Journal of Chemical Physics*, 1994.

[23] M. Feigel. Phenyl rotation in diphenylether and diphenylmethane calculated with ab initio methods. *Journal of Molecular Structure-Theochem*, 366(1-2):83 – 88, 1996.

[24] R. Coffman and D. S. McClure. The electronic spectra of crystalline toluene, dibenzyl, diphenylmethane, and biphenyl in the near ultraviolet. *Canadian Journal of Chemistry*, 36(1):48–58, 1958.

[25] D. S. McClure. Energy transfer in molecular crystals and in double molecules. *Canadian Journal of Chemistry*, 36(1):59–71, 1958.

[26] N. R. Pillsbury, J. A. Steams, C. W. Müller, D. F. Plusquellic, and T. S. Zwier. State-specific studies of internal mixing in prototypical flexible bichromophore: Diphenylmethane. *Journal of Chemical Physics*, 129:114301, 2008.

[27] J. A. Steams, N. R. Pillsbury, K. O. Doublass, C. W. Müller, T. S. Zwier, and D. F. Plusquellic. Rotatinoally resolved studies of s_0 and the exciton coupled s_1/s_2 origin regions of diphenylmethane and the d_{12} isotopologue. *Journal of Chemical Physics*, 129:224305, 2008.

[28] C. P. Hsu, G. R. Fleming, M. Head-Gordon, and T. Head-Gordon. Excitation energy transfer in condensed media. *Journal of Chemical Physics*, 114(7):3065–3072, 2001.

[29] T. Förster. Delocalized excitation and excitation transfer. In Oktay Sinanoğlu, editor, *Modern Quantum Chemistry*, volume III. Academic Press, New York, 1965.

[30] E. Condon. A theory of intensity distribution in band systems. *Physical Reviews*, 28:1182–1201, 1926.

[31] C. Lee, W. Yang, and R. G. Parr. Development of the colle-salvetti correlation-energy formula into a functional of the electron density. *Physical Review B*, 37:785–789, Jan 1988.

[32] S. H. Vosko, L. Wilk, and M. Nusair. Accurate spin-dependent electron liquid correlation energies for local spin density calculations: a critical analysis. *Canadian Journal of Physics*, 58(8):1200–1211, 1980.

[33] A. D. Becke. Density-functional thermochemistry 3: The role of exact exchange. *Journal Of Chemical Physics*, 98(7):5648–5652, 1993.

[34] Jr. T. H. Dunning. Gaussian basis sets for use in correlated molecular calculations. i. the atoms boron through neon and hydrogen. *Journal of Chemical Physics*, 90(2):1007–1023, 1989.

[35] Y. Shao, L.F. Molnar, Y. Jung, J. Kussmann, C. Ochsenfeld, S. Brown, A.T.B. Gilbert, L.V. Slipchenko, S.V. Levchenko, D.P. O'Neil, R.A. Distasio Jr, R.C. Lochan, T. Wang, G.J.O. Beran, N.A. Besley, J.M. Herbert, C.Y. Lin, T. Van Voorhis, S.H. Chien, A. Sodt, R.P. Steele, V.A. Rassolov, P. Maslen, P.P. Korambath, R.D. Adamson, B. Austin, J. Baker, E.F.C. Bird, H. Daschel, R.J. Doerksen, A. Drew, B.D. Dunietz, A.D. Dutoi, T.R. Furlani, S.R. Gwaltney, A. Heyden, S. Hirata, C.-P. Hsu, G.S. Kedziora, R.Z. Khalliulin, P. Klunziger, A.M. Lee, W.Z. Liang, I. Lotan, N. Nair, B. Peters, E.I. Proynov, P.A. Pieniazek, Y.M. Rhee, J. Ritchie, E. Rosta, C.D. Sherrill, A.C. Simmonett, J.E. Subotnik, H.L. Woodcock III, W. Zhang, A.T. Bell, A.K. Chakraborty, D.M. Chipman, F.J. Keil, A. Warshel, W.J. Herhe, H.F. Schaefer III, J. Kong, A.I. Krylov, P.M.W. Gill, and M. Head-Gordon. Advances in methods and algorithms in a modern quantum chemistry program package. *Physical Chemistry Chemical Physics*, 8:3172–3191, 2006.

[36] V.A. Mozhayskiy and A.I. Krylov.
ezSpectrum, http://iopenshell.usc.edu/downloads/.

[37] J. P. Perdew. Density-functional approximation for the correlation energy of the inhomogeneous electron gas. *Physical Review B*, 33:8822–8824, Jun 1986.

[38] A. D. Becke. Density-functional exchange-energy approximation with correct asymptotic behavior. *Physical Review A*, 38:3098–3100, Sep 1988.

[39] J. D. Chai and M. Head-Gordon. Long-range corrected hybrid density functionals with damped atom-atom dispersion corrections. *Physical Chemistry Chemical Physics*, 10:6615–6620, 2008.

[40] J. F. Stanton and R. J. Bartlett. The equation of motion coupled-cluster method. a systematic biorthogonal approach to molecular excitation energies, transition probabilities, and excited state properties. *Journal of Chemical Physics*, 98(9):7029–7039, 1993.

[41] H. Sekino and R. J. Bartlett. A linear response, coupled-cluster theory for excitation energy. *International Journal of Quantum Chemistry*, 26(S18):255–265, 1984.

[42] H. Koch, H. Jørgen A. A. Jensen, P. Jørgensen, and T. Helgaker. Excitation energies from the coupled cluster singles and doubles linear response function (ccsdlr). applications to be, ch^+,co, and h_2o. *Journal of Chemical Physics*, 93(5):3345–3350, 1990.

[43] A.I. Krylov. Equation-of-motion coupled-cluster methods for open-shell and electronically excited species: The hitchhiker's guide to Fock space. *Annual Reviews of Physical Chemistry*, 59:433–462, 2008.

[44] N. R. Pillsbury, N. M. Kidwell, B. Nebgen, L. V. Slipchenko, K. O. Douglass, J. R. Cable, D. F. Plusquellic, and T. S. Zwier. Vibronic coupling in asymmetric bichromophores: Experimental investigation of diphenylmethane-d(5). *Journal of Chemical Physics*, 141(6), 2014.

[45] B. Nebgen, F. L. Emmert, III, and L. V. Slipchenko. Vibronic coupling in asymmetric bichromophores: Theory and application to diphenylmethane. *Journal of Chemical Physics*, 137(8), 2012.

[46] B. Nebgen and L. V. Slipchenko. Vibronic coupling in asymmetric bichromophores: Theory and application to diphenylmethane-d5. *The Journal of Chemical Physics*, 141(13):–, 2014.

[47] J. Seibt, V. Dehm, F. Wurthner, and V. Engel. Absorption spectroscopy of molecular trimers. *Journal of Chemical Physics*, 126(16):164308, 2007.

[48] MATLAB. *version 7.10.0 (R2010a)*. The MathWorks Inc., Natick, Massachusetts, 2010.

[49] A. Witkowski and W. Moffitt. Electronic spectra of dimers: Derivation of the fundamental vibronic equation. *Journal of Chemical Physics*, 33(3):872–875, 1960.

[50] S. Balay, S. Abhyankar, M. F. Adams, J. Brown, P. Brune, K. Buschelman, V. Eijkhout, W. D. Groppand, D. Kaushik, M. G. Knepley, L. C. McInnes, K. Rupp, B. F. Smith, and H. Zhang. PETSc users manual. Technical Report ANL-95/11 - Revision 3.5, Argonne National Laboratory, 2014.

[51] S. Balay, S. Abhyankar, M. F. Adams, J. Brown, P. Brune, K. Buschelman, V. Eijkhout, W. D. Gropp, D. Kaushik, M. G. Knepley, L. C. McInnes, K. Rupp, B. F. Smith, and H. Zhang. PETSc Web page. http://www.mcs.anl.gov/petsc, 2014.

[52] S. Balay, W. D. Gropp, L. C. McInnes, and B. F. Smith. Efficient management of parallelism in object oriented numerical software libraries. In E. Arge, A. M. Bruaset, and H. P. Langtangen, editors, *Modern Software Tools in Scientific Computing*, pages 163–202. Birkhäuser Press, 1997.

[53] V. Hernandez, J. E. Roman, and V. Vidal. SLEPc: A scalable and flexible toolkit for the solution of eigenvalue problems. *ACM Transactions of Mathematical Software*, 31(3):351–362, 2005.

[54] V. Hernandez, J. E. Roman, and V. Vidal. SLEPc: Scalable Library for Eigenvalue Problem Computations. *Lecture Notes in Computer Science*, 2565:377–391, 2003.

[55] J. E. Roman, C. Campos, E. Romero, and A. Tomas. SLEPc users manual. Technical Report DSIC-II/24/02 - Revision 3.5, D. Sistemes Informàtics i Computació, Universitat Politècnica de València, 2014.

[56] B. Nebgen and L. V. Slipchenko. EVSpectrum Web Page. https://github.com/bnebgen/EVspectrum, 2014.

[57] N. M. Kidwell, N. J. Reilly, B. Nebgen, D. N. Mehta-Hurt, R. D. Hoehn, D. L. Kokkin, M. C. McCarthy, L. V. Slipchenko, and T. S. Zwier. Jet-cooled spectroscopy of the a-methylbenzyl radical: Probing the state-dependent effects of methyl rocking against a radical site. *The Journal of Physical Chemistry A*, 117(50):13465–13480, 2013.

[58] H. Sekino and R. J. Bartlett. A linear response, coupled-cluster theory for excitation-energy. *International Journal Of Quantum Chemistry*, (18):255–265, 1984.

[59] J. F. Stanton and R. J. Bartlett. The equation of motion coupled-cluster method - a systematic biorthogonal approach to molecular-excitation energies, transition-probabilities, and excited-state properties. *Journal Of Chemical Physics*, 98(9):7029–7039, 1993.

[60] J. F. Stanton and J. Gauss. Analytic energy derivatives for ionized states described by the equation-of-motion coupled-cluster method. *Journal Of Chemical Physics*, 101(10):8938–8944, 1994.

[61] J. F. Stanton and J. Gauss. A simple scheme for the direct calculation of ionization potentials with coupled-cluster theory that exploits established excitation energy methods. *Journal Of Chemical Physics*, 111(19):8785–8788, 1999.

[62] L. V. Slipchenko and A. I. Krylov. Spin-conserving and spin-flipping equation-of-motion coupled-cluster method with triple excitations. *Journal Of Chemical Physics*, 123(8), 2005.

[63] B. O. Roos, P. R. Taylor, and P. E. M. Siegbahn. A complete active space scf method (casscf) using a density-matrix formulated super-ci approach. *Chemical Physics*, 48(2):157–173, 1980.

[64] H. Nakano. Quasi-degenerate perturbation-theory with multiconfigurational self-consistent-field reference functions. *Journal Of Chemical Physics*, 99(10):7983–7992, 1993.

[65] M. W. Schmidt, K. K. Baldridge, J. A. Boatz, S. T. Elbert, M. S. Gordon, J. H. Jensen, S. Koseki, N. Matsunaga, K. A. Nguyen, S. J. Su, T. L. Windus, M. Dupuis, and J. A. Montgomery. General atomic and molecular electronic-structure system. *Journal Of Computational Chemistry*, 14(11):1347–1363, 1993.

[66] W. J. Hehre, Ditchfie R, and J. A. Pople. Self-consistent molecular-orbital methods .12. further extensions of gaussian-type basis sets for use in molecular-orbital studies of organic-molecules. *Journal Of Chemical Physics*, 56(5):2257–2261, 1972.

[67] P. C. Harihara and J. A. Pople. Influence of polarization functions on molecular-orbital hydrogenation energies. *Theoretica Chimica Acta*, 28(3):213–222, 1973.

[68] K. Raghavachari, G. W. Trucks, J. A. Pople, and M Head-Gordon. A 5th-order perturbation comparison of electron correlation theories. *Chemical Physics Letters*, 157(6):479–483, 1989.

[69] C. Cossart-Magos and S. Leach. Determination of the symmetry of the first excited electronic state of benzyl by rotational contour analysis of vibronic bands of the emission spectra of $C_6H_5CH_2$, $C_6H_5CD_2$, and $C_6D_5CD_2$. *Journal of Chemical Physics*, 56(4):1534–1545, 1972.

[70] M. Heaven, L. Dimauro, and T. A. Miller. Laser-induced fluorescence spectra of free-jet cooled organic free radicals. vinoxy, cyclopentadienyl, and benzyl. *Chemical Physics Letters*, 95(45):347 – 351, 1983.

[71] J. E. Rice, N. C. Handy, and P. J. Knowles. An mcscf study of the x $^2B_2$, $^2A_2$ and 2^2B_2 states of benzyl. *Journal Of The Chemical Society-Faraday Transactions Ii*, 83(9):1643–1649, 1987.

[72] F. Negri, G. Orlandi, F. Zerbetto, and M. Z. Zgierski. Quantum chemical and vibronic analysis of the $1^2B_2 \leftrightarrow 1^2A_2$, 2^2B_2 transition in benzyl-H_7 and benzyl-D_7 radicals. *Journal Of Chemical Physics*, 93(1):600–608, 1990.

[73] C. Cossart-Magos and S. Leach. 2-mode vibronic interaction between neighboring 1^2A_2 and 2^2B_2 excited electronic states of benzyl radical. *Journal Of Chemical Physics*, 64(10):4006–4019, 1976.

[74] N. J. Reilly, M. Nakajima, B. A. Gibson, T. W. Schmidt, and S. H. Kable. Laser-induced fluorescence and dispersed fluorescence spectroscopy of jet-cooled 1-phenylpropargyl radical. *Journal of Chemical Physics*, 130(14):144313, 2009.

[75] I. A. Kaliman and L. V. Slipchenko. Libefp: A new parallel implementation of the effective fragment potential method as a portable software library. *Journal of Computational Chemistry*, 34(26):2284–2292, 2013.

[76] A. L. Sobolewski and W. Domcke. Computational studies of the photophysics of hydrogen-bonded molecular systems. *Journal of Physical Chemistry A*, 111(46):11725–11735, 2007.

[77] A. L. Sobolewski and W. Domcke. Photoinduced electron and proton transfer in phenol and its clusters with water and ammonia. *Journal of Physical Chemistry A*, 105(40):9275–9283, 2001.

APPENDIX

A. APPENDIX: SAMPLE INPUT FILE FOR EV-SPECTRUM

This appendix contains an input file for EV-Spectrum.

```
$comment
Dimer example
2-vibrational modes
$end

$problem
nvib 2
nelec 2
neigen 30
vbasis 8 8
$end

$hamiltonian
c[1]|1><1|n[1]
c[2]|1><1|n[2]
c[3]|1><1|a^[1]
c[3]|1><1|a_[1]
c[4]|1><1|
c[5]|2><2|n[1]
c[6]|2><2|n[2]
c[7]|2><2|a^[2]
c[7]|2><2|a_[2]
```

```
c[8]|2><2|
c[9]|1><2|
c[9]|2><1|
$end

$parameters
c[1] 550.0
c[2] 500.0
c[3] 311.1
c[4] -525.0
c[5] 560
c[6] 490
c[7] 242.5
c[8] 525.0
c[9] 110
$end

$groundfrequency
gs[1] 500.0
gs[2] 560
$end
```

VITA

VITA

Ben Nebgen was born in Ames, Iowa but moved at a young age to Rhinelander, Wisconsin, where he grew up. After graduating from Rhinelander High School in 2006, he attended Cornell University. At Cornell, he majored in chemistry and did research under Dr. Stephen Lee and Dr. Roger Loring. in 2010 he graduated with Magna Cum Laude.

Ben began graduate school in fall 2010 under his adviser Dr. Lyudmila Slipchenko. There he developed a vibronic coupling model for multi-chromophores and applied it to many systems with experimental data taken by Zwier and co workers. Additionally, he worked on simulating the excited states of various radicals. Additional duties included maintaining one of the group's computer clusters as well as being the teaching assistant for chemistry 579, a graduate level molecular dynamics course.

Ben intends to continue doing theoretical chemistry research with Dr. Oleg Prezhdo at the University of Southern California. Research will focus on fragmentation methods applied to nano-particles with application to synthetic light harvesting systems. Ben Nebgen will be reachable at the e-mail address btn7@cornell.edu.

PUBLICATION

THE JOURNAL OF CHEMICAL PHYSICS **137**, 084112 (2012)

Vibronic coupling in asymmetric bichromophores: Theory and application to diphenylmethane

Ben Nebgen, Frank Lee Emmert III, and Lyudmila V. Slipchenko
Department of Chemistry, Purdue University, West Lafayette, Indiana 47907, USA

(Received 15 May 2012; accepted 7 August 2012; published online 30 August 2012)

The theory for modeling vibronic interactions in bichromophores was introduced in sixties by Witkowski and Moffitt [J. Chem. Phys. **33**, 872 (1960)] and extended by Fulton and Gouterman [J. Chem. Phys. **35**, 1059 (1961)]. The present work describes extension of this vibronic model to describe bichromophores with broken vibrational symmetry such as partly deuterated molecules. Additionally, the model is extended to include inter-chromophore vibrational modes. The model can treat multiple vibrational modes by employing Lanczos diagonalization procedure of sparse matrices. The developed vibronic model is applied to simulation of vibronic spectra of flexible bichromophore diphenylmethane and compared to high-resolution experimental spectra [J. A. Stearns, N. R. Pillsbury, K. O. Douglass, C. W. Müller, T. S. Zwier, and D. F. Plusquellic, J. Chem. Phys. **129**, 224305 (2008)]. © *2012 American Institute of Physics*. [http://dx.doi.org/10.1063/1.4747336]

I. INTRODUCTION

The interaction of light and matter is a fundamental phenomenon whose understanding and control are quintessential for advances in science and technology. Often, quantum-mechanical treatment of the light-induced processes can be simplified by separating electronic and nuclear degrees of freedom by introducing the conventional Born-Oppenheimer (BO) approximation.[1] Yet, to explain processes such as conversion of solar to electrical energy as occurs in photosynthetic centers of plants and bacteria and is mimicked in photovoltaic devices, the electronic and nuclear motions cannot be uncoupled such that the BO approximation should be abandoned. A wide variety of classical, semi-classical, and quantum techniques have been suggested to simulate dynamics in such systems.[2] In classical approaches the nuclear wavepacket is approximated by an ensemble of particles that follow classical trajectories. Semi-classical methods add some missing quantum effects to this picture by allowing transitions between the electronic states, for example, through surface hopping[3] or using the mean-field approximation.[4,5] In quantum-dynamics methods the nuclear wavepacket is described by including quantum effects, such as interference between different parts of the packet.[6,7]

Alternatively, one can circumvent complexities associated with modeling dynamics of vibronic systems and describe their vibronic spectra statically. This can be accomplished by solving the time-independent Schrodinger equation with an electronic-nuclear Hamiltonian. The present work applies the latter (static) approach to a molecular system composed of two (nearly) identical chromophores. Such bichromophores or molecular dimers have nearly degenerate electronic energy levels with an energy splitting close to the separation in vibrational energy levels, resulting in coupling of the electronic and nuclear degrees of freedom. Pioneering work in this direction was done by Witkowski and Moffitt,[8] who derived the Hamiltonian for a dimer with a specific symmetry element exchanging the monomers. This vibronic model was expanded on by Fulton and Gouterman (FG)[9,10] by describing excited state vibrations through a series of displaced harmonic oscillators.[10,11] Following this initial work, Siebrand and co-workers extended the theory to Raman scattering[12] and made connections to molecular aggregates.[13] Since then, this model has been applied to a number of molecular dimers,[14–19] extended to include multiple vibrational modes,[20–22] and used to describe vibronic states in more complex molecular aggregates.[23,24]

The original FG vibronic coupling model is limited to cases where the dimer has a symmetry element interchanging the Hamiltonians of monomers. The symmetry element simplifies the dimer Hamiltonian and its numerical solution. However, at the expense of increased computational complexity, the Hamiltonian can be left in the asymmetric form and, after expanding the vibrational wavefunction in a basis, diagonalized numerically using the iterative Lanczos diagonalization routine, as previously suggested by Domcke and co-workers.[25] This approach can handle asymmetries in the vibrational wavefunction arising from partial deuteration. The present work describes an extension of the vibronic model to the asymmetric bichromophores of this type. The present work assumes that the bichromophore retains symmetry of the electronic wavefunction. However, with evaluation of an additional electronic integral this model can be generalized to molecules with asymmetries in electronic wavefunction arising, for example, from asymmetric molecular orientations, substituent groups on monomers, or from different interaction of monomers with environment, as would occur in realistic biological or materials systems. The present work also introduces the Hamiltonian for the inter-chromophore vibrational modes, i.e., vibrations that occur between the chromophores themselves. The inter-monomer Hamiltonian is fundamentally different from the intra-monomer one because the electronic coupling depends on the distance and orientation between the two monomers and thus upon the inter-monomer vibrations.

Developments described in the present study differentiate from the previously reported extensions of the original FG vibronic model in several important aspects. For example, while the FG model was previously extended to simulate several vibrational modes,[20–22] our implementation utilizes the iterative Lanczos diagonalization routine that allows simultaneous modeling of a larger number of vibrations. The previous work on asymmetric dimers[18] was focused on electronic asymmetries while maintaining the assumption of vibrational symmetry. This is in contrast to our model that targets vibrational rather than electronic asymmetry. There are also reports on modeling inter-monomer vibrations,[17,18] which, however, do not include the explicit modulation of the exciton coupling matrix element along an inter-monomer mode. Our work presents a general approach for modeling the inter-monomer vibrations and explicitly includes a change of the electronic coupling along these modes.

To characterize the developed model, a series of model spectra are produced and analyzed. As an initial test, the extended vibronic coupling model is applied to vibronic spectra of flexible bichromophore diphenylmethane (DPM), which has been the subject of several spectroscopic studies over the last half century.[26–30] Application to this symmetric molecule demonstrates the validity of the inter-monomer mode Hamiltonian and tests the asymmetric model in the symmetric limit. Our future work will focus on modeling vibronic spectrum of partially deuterated DPM (d5-DPM) that will fully utilize asymmetric aspects of the developed model.

II. THEORY

For a bichromophore (also called dimer) composed of two (nearly) identical monomers, the Hamiltonian can be written as a sum of the monomer Hamiltonians and electronic coupling $V_{AB}(L)$ and kinetic energy T_L terms

$$H = H_A + H_B + V_{AB}(L) + T_L. \tag{1}$$

The electronic coupling and the kinetic energy terms depend on the vector of six inter-monomer vibrational modes L. In this treatment, the electronic wavefunction of the dimer is not antisymmetrized, i.e., the electron exchange between the two monomers is neglected. This is a reasonable assumption for a large class of molecules, especially when monomers are spatially separated. However, the following derivations remain true even if the electronic wavefunction of the dimer is antisymmetrized, as is the case for bichromophores. Antisymmetrization of the electronic wavefunction affects the electronic coupling V_{AB} term that will include not only Coulomb but also exchange component.

Vibrations considered in this model are divided into intra-monomer and inter-monomer vibrations. Intra-monomer modes have kinetic and potential energy terms located within H_A and H_B and thus can be computed by calculations on either monomer. The inter-monomer modes are vibrations along the L vector introduced above. Typically, the inter-monomer modes have much lower frequencies than the intra-monomer modes. They cannot be obtained from monomer properties but require (partial) knowledge of the dimer Hessian. Because of these principal differences, the treatment of the intra- and inter-monomer modes in the model should be different. Note that only the intra-monomer modes were considered in the original model and most extensions. The current paper provides the first systematic extension of the dimer vibronic coupling model to the inter-monomer vibrations.

A. Intra-monomer modes

Main steps of the symmetric dimer vibronic coupling model are repeated here in order to introduce notations and bring into context our developments. For the intra-monomer modes, the Hamiltonian of monomer A (and analogously for monomer B) is written as a sum of the vibrational kinetic energy term $T_A(Q_A)$ and the electronic Hamiltonian $h_A(q_A; Q_A)$,

$$H_A = h_A(q_A; Q_A) + T_A(Q_A). \tag{2}$$

The electronic Hamiltonian depends explicitly on the electron coordinate (q_A) and parametrically on the nuclear coordinate (Q_A) of monomer A. Let $\{\psi_i^{\mathrm{el}}(q_A; Q_A)\}_{\forall i \geq 0}$ be the eigenvectors of the electronic Hamiltonian h_A with energies $E_i(Q_A)$; $\{\phi_j(Q_A)\}_{\forall j \geq 0}$ be the eigenvectors of the vibrational Hamiltonian $E_i(Q_A) + T_A(Q_A)$. Since similar relationships hold for monomer B, $H_A + H_B$ will satisfy the eigenvalue problem

$$\begin{aligned}(H_A + H_B)\psi_i^{\mathrm{el}}(q_A; Q_A)\phi_n(Q_A)\psi_j^{\mathrm{el}}(q_B; Q_B)\phi_m(Q_B) \\ = E_{i,j,n,m}(Q_A, Q_B)\psi_i^{\mathrm{el}}(q_A; Q_A)\phi_n(Q_A) \\ \times \psi_j^{\mathrm{el}}(q_B; Q_B)\phi_m(Q_B),\end{aligned} \tag{3}$$

where

$$E_{i,j,n,m}(Q_A, Q_B) = E_{i,n}(Q_A) + E_{j,m}(Q_B), \tag{4}$$

i and j represent the level of electronic excitation on monomers A and B, respectively. Similarly, n and m represent the vibrational excitation on either monomer.

Before introducing the electronic coupling, the energies obey the following relation:

$$E_{i,j,n,m} = E_{j,i,m,n}. \tag{5}$$

The degeneracy in the electronic states is split by the electronic coupling term $V_{AB}(L)$ in the electronic Hamiltonian Eq. (1).

Consider now a pair of exciton states. The excitation may occur either on monomer A or monomer B; neither double excitations (both on A and B) nor charge-transfer excitations (electron moves from A to B or vice versa) are considered in this model. Thus, a two element basis is sufficient for the electronic wavefunction

$$\begin{aligned}\{\pi_A^{(1)} &= \psi_1^{\mathrm{el}}(q_A; Q_A)\psi_0^{\mathrm{el}}(q_B; Q_B), \\ \pi_B^{(1)} &= \psi_0^{\mathrm{el}}(q_A; Q_A)\psi_1^{\mathrm{el}}(q_B; Q_B)\}.\end{aligned} \tag{6}$$

Though the following derivations are valid for any electronic states in the monomer, for the sake of simplicity, we use the notations corresponding to the electronic transition from the ground state ψ_0 to the first electronic excited state ψ_1.

To find algebraic expressions for the vibrational energies, the Hamiltonian has to be expanded in the electronic basis, resulting in the following matrix elements:

$$\langle\pi_A^{(1)}|H|\pi_A^{(1)}\rangle = T_A + E^{(1)}(Q_A) + T_B$$
$$+E^{(0)}(Q_B) + \langle\pi_A^{(1)}|V_{AB}|\pi_A^{(1)}\rangle, \quad (7)$$

$$\langle\pi_B^{(1)}|H|\pi_B^{(1)}\rangle = T_A + E^{(0)}(Q_A) + T_B$$
$$+E^{1}(Q_B) + \langle\pi_B^{(1)}|V_{AB}|\pi_B^{(1)}\rangle,$$
$$\langle\pi_A^{(1)}|H|\pi_B^{(1)}\rangle = \langle\pi_B^{(1)}|H|\pi_A^{(1)}\rangle = \langle\pi_A^{(1)}|V_{AB}|\pi_B^{(1)}\rangle. \quad (8)$$

In case of the intra-monomer modes, $V_{AB}(L)$ is expanded in Taylor series about the equilibrium position of $L = 0$ and only the zero-order term is kept:

$$\langle\pi_A^{(1)}|V_{AB}(L)|\pi_B^{(1)}\rangle \simeq \langle\pi_A^{(1)}|V_{AB}(0)|\pi_B^{(1)}\rangle$$
$$+\frac{\partial}{\partial L}\langle\pi_A^{(1)}|V_{AB}(L)|\pi_B^{(1)}\rangle|_{L=0}L$$
$$+\frac{\partial^2}{\partial^2 L}\langle\pi_A^{(1)}|V_{AB}(L)|\pi_B^{(1)}\rangle|_{L=0}\frac{L^2}{2}. \quad (9)$$

The remaining terms in the Taylor expansion along with the T_L term will be considered in Sec. II B regarding inter-monomer modes, since such vibrations affecting the relative positioning of the monomers are anticipated to have a large effect on coupling constant. Assuming the harmonic approximation for the potential energy surface (PES) in the vicinity of the minimum provides a functional form for $E^{(0)}(Q_A)$, $E^{(1)}(Q_A)$, $E^{(0)}(Q_B)$, and $E^{(1)}(Q_B)$. For example, for monomer A,

$$E^{(0)}(Q_A) = \frac{1}{2}M\omega_A^2 Q_A^2, \quad (10)$$

$$E^{(1)}(Q_A) = E_e + l_A Q_A + \frac{1}{2}M\omega_A^2 Q_A^2, \quad (11)$$

where M is the reduced mass and ω is the characteristic frequency of the normal mode. The displacement l_A is defined as

$$l_A = dQM\omega_A^2, \quad (12)$$

dQ is the displacement along the normal mode between geometries of the ground and excited states (see Fig. 1). For simplicity $Q_A = 0$ is defined as the equilibrium position for the normal mode in the ground electronic state, such that a linear term is only present in the expression for the excited state potential energy surface.

The integral $\langle\pi_A^{(1)}|V_{AB}|\pi_A^{(1)}\rangle$ in Eq. (7) can be evaluated from standard electronic structure packages by modifications of the electronic structure integral codes. Input of this integral is one of the requirements to handling electronic wavefunction asymmetry. However, this term is not necessary for bichromophores with symmetric electronic wavefunction since, by symmetry,

$$\langle\pi_A^{(1)}|V_{AB}|\pi_A^{(1)}\rangle = \langle\pi_B^{(1)}|V_{AB}|\pi_B^{(1)}\rangle. \quad (13)$$

Thus, these terms shift all energy levels by the same quantity and do not affect energy spacings. Leutwyler and coworkers studied electronic wavefunction asymmetry in the 2-pyridone · 6-methyl-2-pyridone dimer by adding these terms to the Hamiltonian matrix.[18]

To summarize, the Hamiltonian in the electronic basis can be written as

$$H = \begin{pmatrix} \frac{P_A^2}{2M} + E_A + l_A Q_A + \frac{1}{2}M\omega_A^2 Q_A^2 + \frac{P_B^2}{2M} + \frac{1}{2}M\omega_B^2 Q_B^2 & V_{AB} \\ V_{AB} & \frac{P_A^2}{2M} + \frac{1}{2}M\omega_A^2 Q_A^2 + \frac{P_B^2}{2M} + E_B + lQ_B + \frac{1}{2}M\omega_B^2 Q_B^2 \end{pmatrix}. \quad (14)$$

The electronic coupling (or resonance integral) V_{AB} term can be evaluated by a number of perturbative or supermolecular techniques.[31–36] In this work, the coupling is calculated as half the splitting between the exciton states of the dimer.

In the original vibronic coupling model, the Hamiltonian in Eq. (14) is transformed to a symmetric basis

$$\pi_+^{(1)} = \frac{1}{\sqrt{2}}(\pi_A^{(1)} + \pi_B^{(1)}), \quad (15)$$

$$\pi_-^{(1)} = \frac{1}{\sqrt{2}}(\pi_A^{(1)} - \pi_B^{(1)}). \quad (16)$$

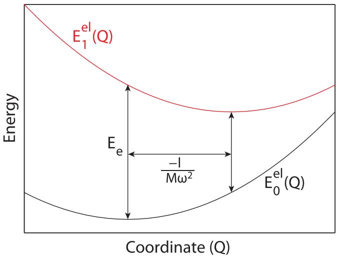

FIG. 1. Potential energy surfaces for the ground (black) and excited (red) electronic state along vibrational mode Q. E_e is the vertical excitation energy and $\frac{-l}{M\omega^2}$ is the displacement between the two minima.

This unitary transformation does not change the eigenvalues of the Hamiltonian. In addition to the electronic basis transformation, Fulton and Gouterman used a vibrational coordinate transformation from Q_A and Q_B to

$$Q_{\pm} = \frac{1}{\sqrt{2}}(Q_A \pm Q_B). \tag{17}$$

This step simplifies diagonalization of the Hamiltonian, but only when the dimer has a symmetry element ensuring $l_A = l_B$ and $\omega_A = \omega_B$.

In order to extend the model to asymmetric dimers, the transformation to the symmetric basis is not performed. By expressing momentum and position operators with raising and lowering operators and assuming a harmonic basis, the Hamiltonian matrix elements are

$$\begin{aligned}\langle\pi_A^{(1)}|H|\pi_A^{(1)}\rangle &= b_A\hbar\omega_A\big(\sqrt{n+1}\delta_{(n',n+1)} \\ &\quad + \sqrt{n}\delta_{(n',n-1)}\big)\delta_{(m',m)} + \left(\hbar\omega_A\left(n+\frac{1}{2}\right)\right. \\ &\quad \left. + \hbar\omega_B\left(m+\frac{1}{2}\right) + E_A\right)\delta_{(n',n)}\delta_{(m',m)},\end{aligned} \tag{18}$$

$$\begin{aligned}\langle\pi_B^{(1)}|H|\pi_B^{(1)}\rangle &= b_B\hbar\omega_B\big(\sqrt{m+1}\delta_{(m',m+1)} \\ &\quad + \sqrt{m}\delta_{(m',m-1)}\big)\delta_{(n',n)} + \left(\hbar\omega_A\left(n+\frac{1}{2}\right)\right. \\ &\quad \left. + \hbar\omega_B\left(m+\frac{1}{2}\right) + E_B\right)\delta_{(n',n)}\delta_{(m',m)},\end{aligned} \tag{19}$$

$$\langle\pi_A^{(1)}|\ H|\pi_B^{(1)}\rangle = \langle\pi_B^{(1)}|H|\pi_A^{(1)}\rangle = V_{AB}\delta_{(n',n)}\delta_{(m',m)}, \tag{20}$$

where n and n' (m and m') represent the excitation quanta of a given normal mode for the vibration on A (B) monomer. Dimensionless displacement parameters b_A and b_B are related to l_A and l_B as

$$b_A\hbar\omega_A = l_A\sqrt{\frac{\hbar}{2M\omega_A}}. \tag{21}$$

The expressions in Eqs. (18)–(20) are expanded in the vibrational basis. The solution generally converges rapidly, requiring around five basis functions in each vibration for spectroscopically reasonable values of b_A and b_B. Convergence with respect to the size of the basis is shown in the supplementary material.[37]

Equations (18)–(20) can be extended in a straightforward manner for multiple vibrational modes on each monomer. In this case, each matrix element is a sum over Hamiltonians for different vibrations and the basis functions are products of the basis function from each vibration.

As pointed out by Förster and others[16,31,38] there are different regimes of vibronic coupling: strong, weak, and intermediate. The quantity that characterizes a mode as either being strongly coupled or weakly coupled to the electronic excitation is given as[10,11]

$$p = \frac{2|\langle\pi_A^{(1)}|V_{AB}|\pi_B^{(1)}\rangle|}{M\omega^2 dQ^2}. \tag{22}$$

Here, $p \gg 1$ corresponds to strongly coupled systems; $p \ll 1$ characterizes weakly coupled systems. $p \simeq 1$ defines the intermediate coupling regime which exhibits the most complicated spectra. For a vibration in the strong or weak limit, it is possible to analytically compute the energies and intensities.[16] Application of perturbation theory to strong and weak coupling regimes is shown in the supplementary material.[37] However, analytic solutions break down as the vibration enters the intermediate coupling regime. Therefore, in the present work, numerical diagonalization of the Hamiltonian using the Lanczos algorithm is employed for all cases, resulting in what Andrzejak and Petelenz call the exact numerical solution.[16]

B. Inter-monomer modes

To compute the eigenstates of inter-monomer vibrations, it is necessary to account for the inter-monomer kinetic energy term, T_L from Eq. (1), as well as higher order terms from the Taylor expansion of V_{AB} in Eq. (9). In order to build a total Hamiltonian, the inter-monomer Hamiltonian will be constructed in the $\{\pi_A^{(1)}, \pi_B^{(1)}\}$ basis and added onto the intra-monomer Hamiltonian. However, because the inter-monomer modes are inherently dependant on the electronic state of the dimer, it is convenient to work in the symmetrized basis $\{\pi_+^{(1)}, \pi_-^{(1)}\}$ as defined in Eqs. (15) and (16), which are the eigenvectors of the dimer electronic Hamiltonian for molecules with only a vibrational asymmetry. So, the Hamiltonian matrix elements of T_L and $V_{AB}(L)$ are first evaluated in the symmetrized basis $\{\pi_+^{(1)}, \pi_-^{(1)}\}$ and then transformed to the monomer basis $\{\pi_A^{(1)}, \pi_B^{(1)}\}$ and added to the Hamiltonian of the intra-monomer modes. In the case of a molecule that does not have electronic wavefunction symmetry, a more complicated approach to finding the relationship between the dimer electronic wavefunctions and the monomer localized electronic basis will need to be taken, but this is beyond the scope of this paper.

Since the geometries of both exciton states $\pi_+^{(1)}$ and $\pi_-^{(1)}$ are different from the ground state geometry along the inter-monomer mode L, the excited state surfaces are described as displaced parabolas. Note that the first (constant) term of the V_{AB} expansion is omitted here since it is already included in the intra-monomer mode Hamiltonian (14). Thus, for geometries near the minima of the excited states,

$$\begin{aligned}&\langle\pi_+^{(1)}|V_{AB}(L) - V_{AB}(0) + T_L|\pi_+^{(1)}\rangle \\ &\quad = l_+L + \frac{1}{2}M\omega_+^2L^2 + \frac{P_+^2}{2M},\end{aligned} \tag{23}$$

$$\begin{aligned}&\langle\pi_-^{(1)}|V_{AB}(L) - V_{AB}(0) + T_L|\pi_-^{(1)}\rangle \\ &\quad = l_-L + \frac{1}{2}M\omega_-^2L^2 + \frac{P_-^2}{2M},\end{aligned} \tag{24}$$

where l_+ and l_- are the displacement parameters analogous to the l_A and l_B terms in the intra-monomer mode case. In the dimer basis, each mode has two displacement parameters (l_+ and l_-) corresponding to the displacements in the ground state to first and second electronic excited state transitions. P_+ and P_- are the kinetic energy terms for the inter-monomer mode in the exciton states. The off-diagonal terms of the inter-monomer Hamiltonian are zero for symmetric electronic wavefunction due to the hermicity of V_{AB} and T_L,

$$\langle \pi_+^{(1)} | V_{AB}(L) + T_L | \pi_-^{(1)} \rangle = \frac{1}{2} \big(\langle \pi_A^{(1)} \big| V_{AB}(L) + T_L \big| \pi_A^{(1)} \rangle - \langle \pi_B^{(1)} \big| V_{AB}(L) + T_L \big| \pi_B^{(1)} \rangle \big) = 0. \tag{25}$$

The reverse transformation from dimer symmetrized electronic basis into the monomer localized basis can be realized by using the following matrix equality:

$$\begin{bmatrix} \pi_A^{(1)} \\ \pi_B^{(1)} \end{bmatrix} = \frac{1}{\sqrt{2}} \begin{bmatrix} 1 & 1 \\ 1 & -1 \end{bmatrix} \begin{bmatrix} \pi_+^{(1)} \\ \pi_-^{(1)} \end{bmatrix}. \tag{26}$$

Applying this matrix transformation to the $V_{AB}(L) + T_L$ terms results in the following form of the inter-monomer mode Hamiltonian:

$$\langle \pi_A^{(1)} \big| V_{AB}(L) + T_L \big| \pi_A^{(1)} \rangle = \langle \pi_B^{(1)} \big| V_{AB}(L) + T_L \big| \pi_B^{(1)} \rangle = \frac{1}{2}(l_+ + l_-)L + \frac{1}{2}\left(\frac{1}{2}M\omega_+^2 + \frac{1}{2}M\omega_-^2\right)L^2, \tag{27}$$

$$\langle \pi_A^{(1)} \big| V_{AB}(L) + T_L \big| \pi_B^{(1)} \rangle = \langle \pi_B^{(1)} \big| V_{AB}(L) + T_L \big| \pi_A^{(1)} \rangle = \frac{1}{2}(l_+ - l_-)L + \frac{1}{2}\left(\frac{1}{2}M\omega_+^2 - \frac{1}{2}M\omega_-^2\right)L^2. \tag{28}$$

The Hamiltonian described in Eqs. (27) and (28) can be added to the intra-monomer mode Hamiltonian (Eqs. (18)–(20)), expanded in a vibrational basis of inter- and intra-monomer modes, and numerically diagonalized.

C. Intensities

Diagonalizing the Hamiltonian (Eqs. (18)–(20), (27) and (28)) results in the vibrational substructure of the exciton states. Evaluation of the intensities of the vibronic states in a fluorescence spectrum is discussed in this subsection. Absorption intensities can be derived analogously.

Following Fulton and Gouterman,[10] the transition dipoles of a symmetric R^+ and antisymmetric R^- excited state to the ground state are

$$R^+ = \int\int \psi_1(q; Q, L)^* M^+ \psi_0(q; Q, L) dq \; \phi_1(Q, L)^* \phi_0(Q, L) dQ dL, \tag{29}$$

$$R^- = \int\int \psi_1(q; Q, L)^* M^- \psi_0(q; Q, L) dq \; \phi_1(Q, L)^* \phi_0(Q, L) dQ dL, \tag{30}$$

where $\psi_1(q; Q, L)$ is the initial (excited state) electronic wavefucntion of the dimer, $\phi_1(Q, L)$ is the initial vibrational wavefunction, $\psi_0(q; Q, L)$ and $\phi_0(Q, L)$ are the final (ground state) electronic and vibrational wavefunctions (the latter is not necessarily the wavefunction with no vibrational excitations). M^+ and M^- are the symmetric and antisymmetric transition dipole operators. The evaluation of R^+ shall now be demonstrated while R^- can be obtained analogously. Assuming that the electronic wavefunction is not strongly affected by the changes in vibrational coordinates, the integral over electronic coordinates and transition dipole operator may be factored out of the integral over nuclear coordinates. Expanding $\psi_1(q)$ in the vibrational basis results in

$$\psi_1(q) = \pi_A^{(1)} \sum_n \sum_m \sum_p C_{n,m,p}^A \phi_n(Q_A) \phi_m(Q_B) \phi_p(L) + \pi_B^{(1)} \sum_n \sum_m \sum_p C_{n,m,p}^B \phi_n(Q_A) \phi_m(Q_B) \phi_p(L), \tag{31}$$

where $\{C_{n,m,p}^A, C_{n,m,p}^B\}$ are the expansion coefficients representing the dimer vibrational wavefunction on the basis of monomer vibrational wavefunctions. Equation (31) can be transformed into the symmetrized electronic dimer basis by applying Eq. (15). It is easy to see that the evaluation of the symmetric transition dipole moment R^+ reduces to calculation of the vibrational overlap integral and the purely electronic transition dipole moment (TDM) between the ground and symmetric excited state $\pi_+^{(1)}$,

$$\int \pi_+^{(1)} M^+ \psi_0 dq. \tag{32}$$

The transition dipole moment between the symmetric dipole operator and antisymmetric wavefunction is zero by a symmetry argument. This is explicitly shown in the supplementary material.[37] Thus, Eq. (29) can be rewritten as

$$R^+ = \frac{1}{\sqrt{2}} \int \pi_+^{(1)} M^+ \psi_0(q; Q) dq \left(\int \sum_n \sum_m \sum_p C_{n,m,p}^A \phi_n(Q_A) \phi_m(Q_B) \phi_p(L) \phi_0(Q, L) dQ dL + \int \sum_n \sum_m \sum_p C_{n,m,p}^B \phi_n(Q_A) \phi_m(Q_B) \phi_p(L) \phi_0(Q, L) dQ dL \right). \tag{33}$$

The final state vibrational wavefunctions are combinations of wavefunctions corresponding to various vibrational modes, $\phi_0(Q, L) = \phi_i(Q_A)\phi_j(Q_B)\phi_k(L)$, where i, j, and k represent the excitation level on A, B, and inter-monomer vibrations, respectively. Assuming orthogonality of the vibrational wavefunctions and the parallel mode approximation,[39] the expression in Eq. (33) reduces to

$$R^+ = \frac{1}{\sqrt{2}} \int \pi_+^{(1)} M^+ \psi_0(q;Q)dq \left(C^A_{i,j,k} + C^B_{i,j,k}\right). \tag{34}$$

The transition dipole corresponding to the transition from the antisymmetric electronic state is

$$R^- = \frac{1}{\sqrt{2}} \int \pi_-^{(1)} M^- \psi_0(q;Q)dq \left(C^A_{i,j,k} - C^B_{i,j,k}\right). \tag{35}$$

The intensity is proportional to a square of the transition dipole moment. The total spectrum may be obtained by summing the intensities of the peaks corresponding to the symmetric and antisymmetric transitions. Note that transitions in asymmetric bichromophores may have mixed symmetric/antisymmetric character.

III. MODEL SPECTRA

In this section, general behavior of a model vibronically coupled bichromophore system is considered. In particular, spectra of asymmetric chromophores, i.e., chromophores with different vibrational frequencies or displacements of a normal mode, and spectra of inter-monomer modes are discussed. Model spectra showing the differences between the strong, weak, and intermediate coupling regimes as well as the interaction between multiple vibrations are shown in the supplementary material.[37] In all figures in this section and the supplementary material,[37] transitions through the antisymmetric TDM are shown in red while transitions through the symmetric TDM are shown in blue.

Various effects of asymmetry in intra-monomer vibrational modes are illustrated in Figs. 2–4. The asymmetry of the vibrational mode is controlled by parameter δ, with $\delta = 0$ corresponding to a symmetric vibration, i.e., vibration that is identical on monomers A and B. Figure 2 shows a case when vibrational modes on monomers have different frequencies. The interesting effect arising due to this asymmetry is splitting of the vibrational peaks in the absorption spectrum. Interestingly, the progression off the S_1 state favors the higher energy vibration while the progression off the S_2 state favors the lower energy one. The picture does not change when the symmetries of S_1 and S_2 states are switched: the lowest state exhibits the more intense progression in a high-frequency vibration. Splittings of the vibrational peaks are also observed in the corresponding emission spectra, but intensities of the split lines are almost equal.

A different case of asymmetry arises when the vibrational modes on the monomers have different displacements between the ground and excited state. Such asymmetries are expected to occur in deuterated molecules because deuteration changes the normal mode vectors, and thus the displacements to the excited state geometry. Model spectra corresponding to the mode in strong coupling regime are reported in Fig. 3. Despite the fact that the frequencies of the two vibrations are identical, the absorption spectrum shows energy splittings in the Frank-Condon progressions both off S_1 and S_2 origins. Similar to the case of the asymmetric frequencies, the lower frequency peak has lower intensity off S_1 and higher intensity off S_2. However, unlike the case with asymmetric frequencies, the intensity of the S_1 origin and S_1 band is depleted suggesting that the vibration with higher b value is coupled to the S_1 state. Different from the case of asymmetric vibrational frequencies, no splitting is present in the emission spectra because the emission levels are governed by the ground state frequencies.

In the previous example (Fig. 3), the vibration is in the strong coupling limit. In Fig. 4, the vibrational mode with

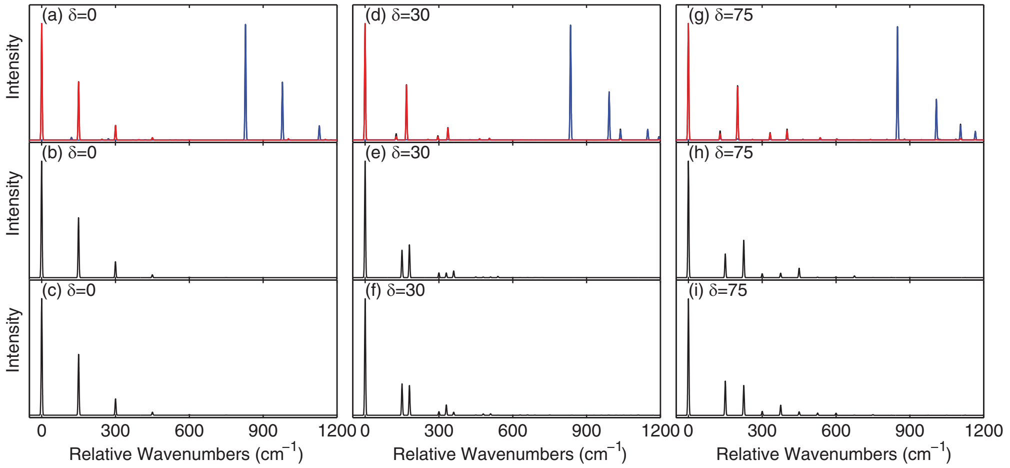

FIG. 2. Model spectra of one intra-monomer vibrational mode in strong coupling regime with different frequencies on either monomer. $\omega_A = 150\,\text{cm}^{-1}$, $\omega_B = 150 + \delta\ \text{cm}^{-1}$, $b_A = b_B = 1.0$, $V_{AB} = 400\,\text{cm}^{-1}$. The first row is absorption, the second row is S_1 emission, and the third row is S_2 emission. $\delta = 0$ in (a)–(c); $\delta = 30\,\text{cm}^{-1}$ in (d)–(f); $\delta = 75\,\text{cm}^{-1}$ in (g)–(i).

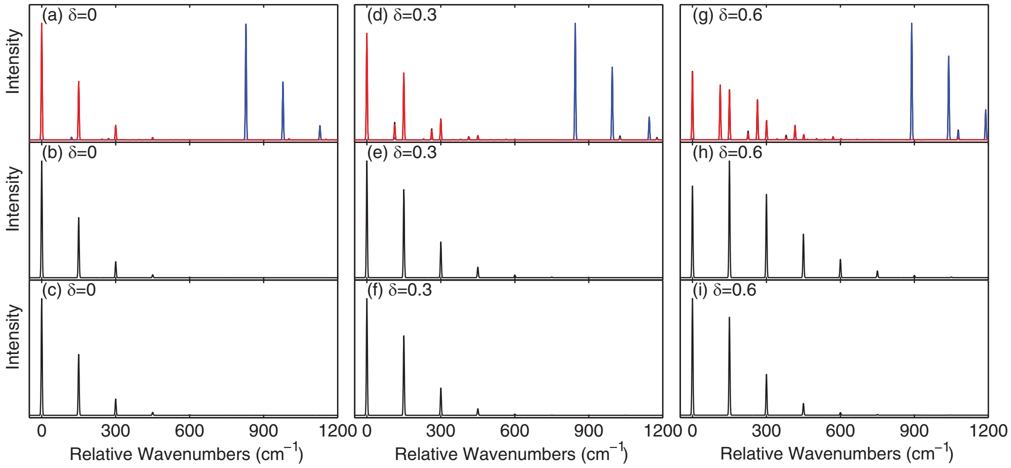

FIG. 3. Model spectra of one intra-monomer vibrational mode in strong coupling regime with different displacements on either monomer. $\omega_A = \omega_B = 150\,\text{cm}^{-1}$, $b_A = 1.0$, $b_B = 1.0 + \delta$, $V_{AB} = 400\,\text{cm}^{-1}$. The first row is absorption, the second row is S_1 emission, and the third row is S_2 emission. $\delta = 0$ in (a)–(c); $\delta = 0.3$ in (d)–(f); $\delta = 0.6$ in (g)–(i).

asymmetric displacements is placed in the weak coupling regime. In this case, the asymmetry is manifested in mixing of S_1 and S_2 progressions, i.e., as the asymmetry is increased, each peak in the absorption spectrum has a mixture of the symmetric and antisymmetric character. The peak corresponding to the S_2 origin gains intensity while the higher vibrational energy levels in the S_2 emission spectrum are reduced in intensity. Another interesting effect observed in these spectra is the increase of the splitting between the S_1 and S_2 origins upon increasing asymmetry between the modes.

Finally, the properties of the inter-monomer vibrations are examined. In the considered examples, the S_1 state is antisymmetric and S_2 is symmetric. As discussed above, the inter-monomer vibrations may have different displacement and frequency parameters for the first and second excited states of a bichromophore. In the first series of spectra, shown in Fig. 5, the effect of changing an excited state frequency is investigated. As demonstrated in Fig. 5, changing the S_1 frequency for an inter-monomer mode results in corresponding change in the vibrational progression off the S_1 origin, while maintaining the same vibrational pattern for the progression off the S_2 state. Both the S_1 and S_2 emission spectra retain the same vibrational spacing because these progressions are dictated by the ground state vibrational states which are independent of whether the molecule was in the S_1 or S_2 excited states.

The effect of different displacements between the $S_1 - S_0$ and $S_2 - S_0$ states (b_{S_-} and b_{S_+} parameters, respectively) is investigated in Fig. 6. When the b_{S_-} displacement is

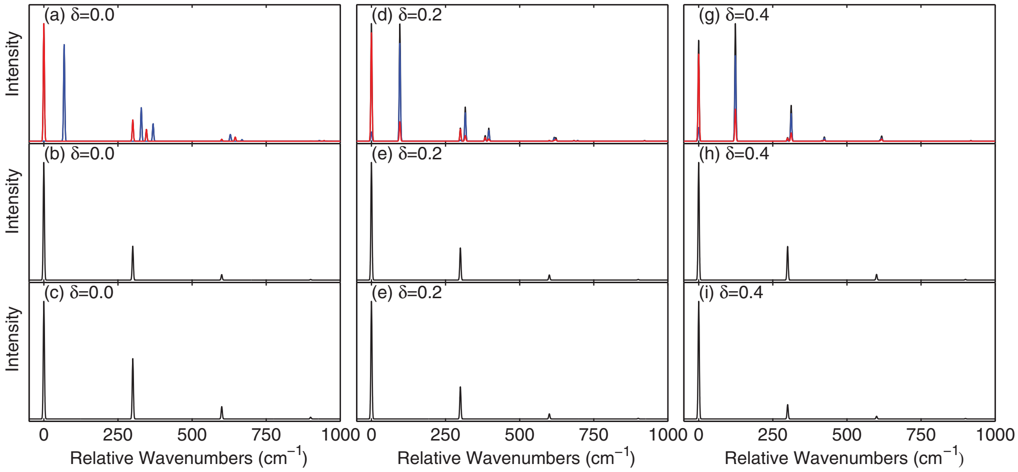

FIG. 4. Model spectra of one intra-monomer vibrational mode in weak coupling regime with different displacements on either monomer. $\omega_A = \omega_B = 300\,\text{cm}^{-1}$, $b_A = 0.6$, $b_B = 0.6 - \delta$, $V_{AB} = 50\,\text{cm}^{-1}$. The first row is absorption, the second row is S_1 emission, and the third row is S_2 emission. $\delta = 0$ in (a)–(c); $\delta = 0.2$ in (d)–(f); $\delta = 0.4$ in (g)–(i).

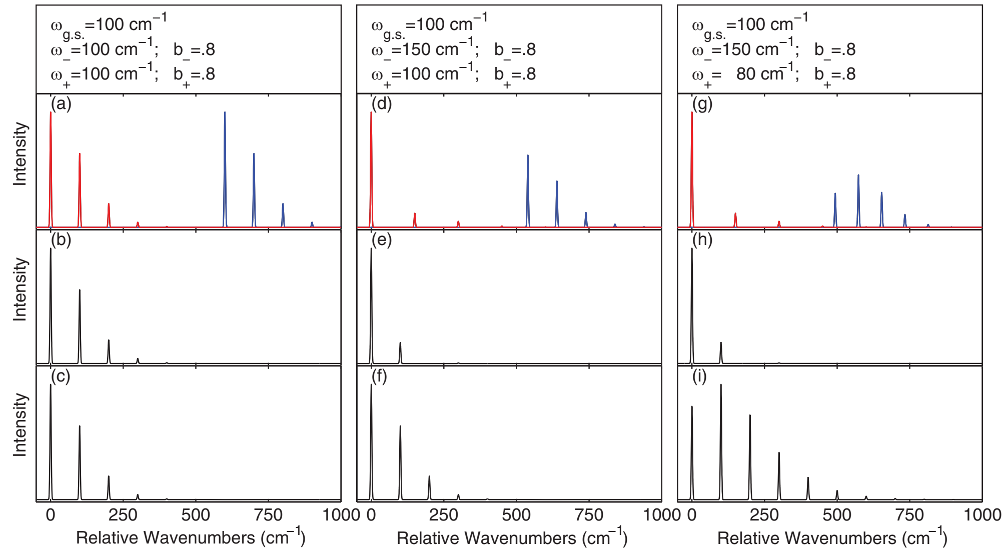

FIG. 5. Model spectra of one inter-monomer vibrational mode with different frequencies in the ground and first and second excited states of the dimer. $V_{AB} = 300\ \mathrm{cm}^{-1}$, $b_- = b_+ = 0.8$ in all spectra. $\omega_{g\cdot s} = \omega_- = \omega_+ = 100\ \mathrm{cm}^{-1}$ in (a)–(c); $\omega_{g\cdot s} = 100\ \mathrm{cm}^{-1}$, $\omega_- = 150\ \mathrm{cm}^{-1}$, $\omega_+ = 100\ \mathrm{cm}^{-1}$ in (d)–(f); $\omega_{g\cdot s} = 100\ \mathrm{cm}^{-1}$, $\omega_- = 150\ \mathrm{cm}^{-1}$, $\omega_+ = 80\ \mathrm{cm}^{-1}$ in (g)–(i). The first row is absorption, the second row is S_1 (S_-) emission, and the third row is S_2 (S_+) emission. Changing the frequency of one state does not change the spacing between frequency levels for the other state.

decreased, the Frank-Condon progression off the S_1 origin in absorption and emission is depleted, while the S_2 bands remain unaffected. Similar effects are observed in the spectra of diphenylmethane, analyzed in Sec. IV. In those spectra, the low frequency inter-monomer vibrations T and $\bar{T}$ appear in the S_1 but not S_2 florescence spectra.

IV. MODELING VIBRONIC SPECTRUM OF DIPHENYLMETHANE

In this section the extended FG model is applied to simulate vibronic spectra of the bichromophore DPM. Zwier and co-workers have gathered high-resolution absorption and

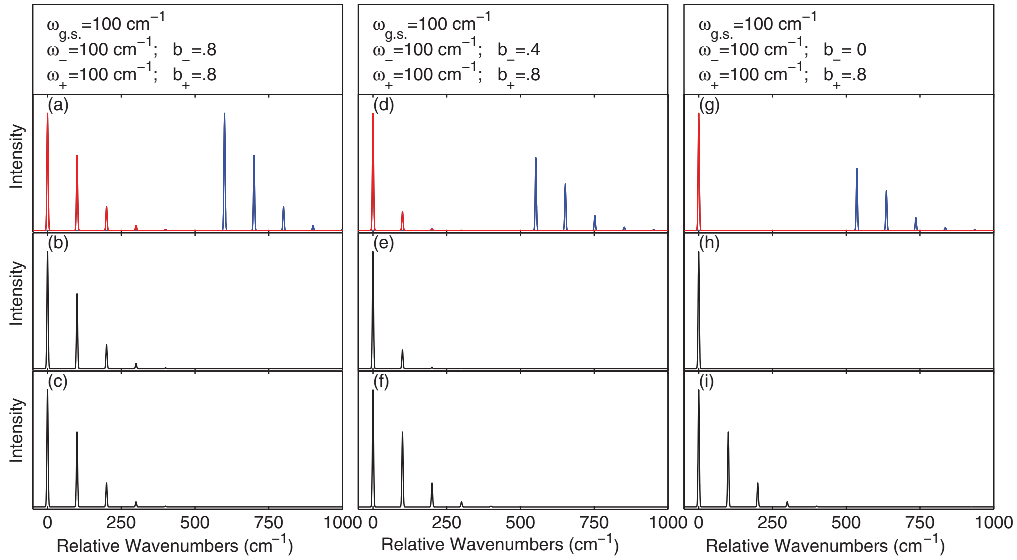

FIG. 6. Model spectra of one inter-monomer vibrational mode with different displacement parameters for the S_1 and S_2 states of the dimer. $V_{AB} = 300\ \mathrm{cm}^{-1}$, $\omega_{g\cdot s} = \omega_- = \omega_+ = 100\ \mathrm{cm}^{-1}$ in all spectra. $b_- = b_+ = 0.8$ in (a)–(c); $b_- = 0.4, b_+ = 0.8$ in (d)–(f); $b_- = 0.0, b_+ = 0.8$ in (g)–(i). The first row is absorption, the second row is S_1 (S_-) emission, and the third row is S_2 (S_+) emission. Changing the displacement for one state allows to suppress the Frank-Condon progression on this state while keeping it on the other.

TABLE I. Intra-monomer vibrational parameters for diphenylmethane as found from B3LYP/cc-pVTZ calculations on toluene.

Assignment	Expt. ω[a] (cm^{-1})	Calc. ω (cm^{-1})	b	p	Quenching factor[b]	Basis functions[c]
$6a_1^0$	554	530	0.26	3.4	Simulated	2
$6b_1^0$	622	639	0.43	1.1	Simulated	5
11_1^0	749	748	0.05	68	1.0	...
1_1^0	822	801	0.65	0.36	Simulated	7
12_1^0	1006	1023	0.73	0.23	0.81	...
$18a_1^0$	1035	1054	0.39	0.77	0.97	...
$9a_1^0$	1204	1206	0.43	0.54	0.89	...
$19b_1^0$	1447	1535	0.02	129	1.0	...

[a] DPM experimental frequencies from Ref. 29.

[b] Quenching factors used to compute the effective electronic coupling as in Eq. (36) for modes not directly included in the simulation ("simulated"). The product of all quenching factors is $\prod_{i=1}^{N} e^{-b_i^2} = 0.48$.

[c] Number of vibrational basis functions used in modeling.

TABLE II. Inter-monomer vibrational parameters as found from B3LYP/cc-pVTZ calculations on S_0, S_1, and S_2 states of diphenylmethane.

Assignment	$\omega_{S_0}(\omega_{g.s.})$ (cm^{-1})	$\omega_{S_1}(\omega_-)$ (cm^{-1})	$\omega_{S_2}(\omega_+)$ (cm^{-1})	$b_{S_1}(b_-)$	$b_{S_2}(b_+)$
$\bar{T}$	22.5	38.3	...[a]	−0.02	−0.06
T	38.5	47.9	35.2	0.60	0.60
β	68.1	62.0	67.5	−1.0	1.2
$\bar{R}$	191	192	105	0.0	0.0
R	225	202	157	−0.62	−0.08

[a] No real-value frequency could be obtained.

emission spectra of the first two singlet excited states of DPM and we will follow their notations for labeling the DPM vibrational modes.[29]

A. Computational details

Vibrational frequencies and displacement parameters for each vibration as well as an electronic coupling term and relative transition dipole moments of S_1 and S_2 are required as input for the vibronic model. The parameters for intra-monomer modes were obtained from density functional theory (DFT) and time-dependent density functional theory (TD-DFT) calculations on toluene which is considered to be a "monomer" of diphenylmethane. The ground and first excited state geometries of toluene were optimized with B3LYP functional[40–42] in the cc-pVTZ basis set[43] with the Q-Chem electronic structure package.[44] Vibrational frequencies of the ground state of toluene were obtained at the same level of theory. ezSpectrum software[45] was used to find the displacements between the ground and first excited state geometries on the basis of the ground state vibrational vectors. These displacements were converted into b parameters; the normal modes with the largest b parameters and corresponding p values (Eq. (22)) are listed in Table I. The number of vibrational basis functions needed for convergence for different b values is determined from extensive testing shown in supplementary material.[37]

To obtain the parameters for the inter-monomer modes, one needs to perform electronic structure calculations on the S_0, S_1, and S_2 states of the dimer (DPM). The parameters obtained from DFT and TD-DFT B3LYP/cc-pVTZ computations are summarized in Table II. The experimental spectra of DPM reveal progressions along five low-frequency inter-monomer modes: symmetric and antisymmetric torsions T and $\bar{T}$, symmetric and antisymmetric R and $\bar{R}$ modes, and the butterfly mode β (shown in supplementary material[37]). From those, parameters of R and $\bar{R}$ were computed in a standard way, i.e., S_0, S_1, and S_2 states of DPM were optimized (the constrained optimization with fixed values of torsional angle corresponding to the T mode was employed for S_2), then the displacements between the ground and the first and second excited state geometries were found on the basis of the ground state vibrations.

Due to an anharmonic nature of the other three modes and extreme sensitivity of parameters to the level of theory employed, their parameters were obtained from PES calculations. Namely, potential energy slices were constructed along normal mode vectors of each mode starting from the S_1 state geometry and employing 0.002 $Å\sqrt{amu}$ displacement increments in either direction of the vibrational vector. TD-DFT B3LYP/cc-pVTZ calculations were performed to find energies of S_1 and S_2 states at each of these geometries. For each vibration, the S_1 and S_2 energies were fit to parabolas, from which frequency and displacement parameters were extracted. As an example, plots of the energies and parabolic fits for the T mode are shown in Fig. 7. However, while this procedure improved agreement between experimental and calculated values of the low-frequency modes compared to the direct calculation of Hessians of the S_1 and S_2 states, it still resulted in overestimated frequencies for all modes and strongly overestimated displacement for the β mode. It should be noted, however, that the β mode is governed by an interplay of covalent and non-covalent, in particular dispersion, interactions between the aromatic rings, and as such is extremely sensitive to the level of theory.

In order to improve the agreement with the experimental spectra, some of the parameters for inter-monomer modes were adjusted. The butterfly mode β that reveals very little intensity in the experimental spectra was excluded from modeling. The resulting set of inter-monomer parameters is presented in Table III.

Vertical splittings between the first and second electronic excited states of DPM were computed by a number of electronic structure methods, including TD-DFT with various functionals (B3LYP, BP86,[46,47] and long-range and

TABLE III. Adjusted (fitted to experimental spectra) inter-monomer vibrational parameters. Calculated values were kept where appropriate.

Assignment	$\omega_{S_0}(\omega_{g.s.})$ (cm^{-1})	$\omega_{S_1}(\omega_-)$ (cm^{-1})	$\omega_{S_2}(\omega_+)$ (cm^{-1})	$b_{S_1}(b_-)$	$b_{S_2}(b_+)$	Basis functions[a]
$\bar{T}$	10.0	23.0	10.0	−0.02	−0.06	8
T	20.0	28.3	20.0	1.40	0.0	12
$\bar{R}$	191	275	105	0.0	0.0	3
R	225	285	188	−0.55	−0.08	7

[a] Number of vibrational basis functions used in modeling.

TABLE IV. Vertical $S_1 - S_2$ splittings computed at the ground state optimized geometry.[a]

Level of theory	$S_1 - S_2$ splitting (cm^{-1})
EOM-CCSD/cc-pVDZ	430
ωB97X-D/cc-pVTZ	549
BP86/cc-pVTZ	539
B3LYP/cc-pVTZ	1069

[a] MP2/cc-pVTZ ground state geometry was used in these calculations.

dispersion corrected ωB97X-D (Ref. 48)), and equation-of-motion coupled cluster with single and double excitations method[49–52] (EOM-CCSD) (see Table IV). Apparently, the value of splitting is sensitive to the level of theory, with the best estimates provided by EOM-CCSD and TD-DFT with ωB97X-D. This results in the electronic coupling, taken as a half of the splitting, in the range of $215 - 275$ cm^{-1}. Including quenching factor due to high-frequency (weakly-coupled) vibrational modes not explicitly included in the simulation (see Table I) results in the effective electronic coupling

$$V_{AB}^{eff} = V_{AB}\prod_{i=1}^{N} e^{\frac{-b_{A,i}^2}{2}} e^{\frac{-b_{B,i}^2}{2}} = V_{AB}\prod_{i=1}^{N} e^{-b_i^2}, \qquad (36)$$

where $b_{A,i}$ and $b_{B,i}$ are displacements for the ith mode on monomer A and B, respectively. In the symmetric case, as in DPM, $b_{A,i} = b_{B,i}$. Using the parameters in Table I, this results in an effective coupling in the range of $103 - 132$ cm^{-1}. The coupling constant used for modeling DPM spectra was taken as 155.8 cm^{-1}. All simulated peaks were modeled by Gaussians with a standard deviation of 1 cm^{-1}.

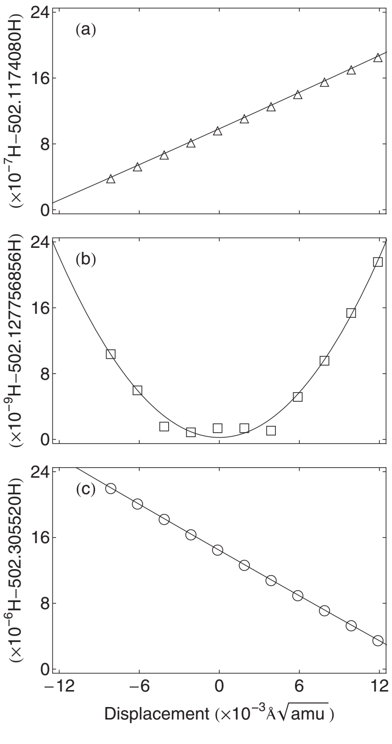

FIG. 7. Potential energy surfaces of the symmetric torsion T mode in (a) the second excited state, (b) the first excited state, and (c) the ground state. The abscissa is the displacement from the optimized S_1 geometry. Energy scales in frames (a)–(c) are different because near the S_1 minimum, the PES of the S_1 state is dominated by second order effects while PESs of the other two states are dominated by first order effects.

B. DPM spectra

Using simulated parameters for intra-monomer vibrational modes (Table I), partly fitted parameters for inter-monomer vibrational modes (Table III), and effective coupling constant $V_{AB} = 155.8$ cm^{-1}, theoretical spectra for DPM were computed as shown in Fig. 8. Comparison of the experimental and theoretical low-frequency absorption spectra (Fig. 8(a)) shows a quantitative agreement both in peak positions and intensities. In particularly, one can clearly recognize a progression along the torsional mode T, with peaks at 27, 54, and 81 cm^{-1}. The peak at 43 cm^{-1} is the second vibrational state of $\bar{T}$ (i.e., $\bar{T}^2$), while the first vibrational quanta are not present. This is because the intensity in the $\bar{T}$ mode is originated due to a frequency change rather than a displacement between the electronic states. Therefore, only even quanta of this mode gain non-zero intensity. Small displacement along the $\bar{T}$ mode ensures that the electronic transition dipole moment that is formally dependent on this mode stays constant and the Condon approximation (Eqs. (34) and (35)) is valid.

As follows from decomposition of the absorption spectrum into symmetric and antisymmetric components (Fig. 8(b)), the origin of the second excited state appears at about 123 cm^{-1}, in agreement with experimental assignment. The intensity of S_2 origin is well reproduced by a S_1/S_2 TDM ratio of 2.08 : 1, which is in close agreement with the 1.98 : 1 ratio computed at the ωB97X-D/cc-pVTZ level of theory.

Analysis of the emission spectrum from the S_1 origin (Fig. 8(c)) shows that the peak at 63 cm^{-1}, missing in the simulated spectrum, is due to the β mode that was excluded from simulations, as mentioned above. Another inter-monomer vibration, R, reveals itself in an intense line at 221 cm^{-1}. This peak is well reproduced by the *ab inito* computations, with only a minor correction in the displacement parameter. All intra-monomer modes, $6a_1^0$, $6b_1^0$, and 1_1^0, are reasonably well described by *ab initio* calculations, with frequency discrepancies not exceeding 30 cm^{-1}. The 11_0^1 vibration with frequency 748 cm^{-1} was not included in the calculation due to a lack of intensity in the S_2 emission spectrum (Fig. 8(d)). There is also a nice agreement between theory and experiment in the high-frequency peaks due to intra-monomer vibrations in the emission spectrum of the S_2 origin (Fig. 8(d)). It is very encouraging that the model spectrum accurately predicts the change in intensity of vibronic bands in the S_1 and S_2 emission spectra, even though there is no parameter that directly controls that intensity ratio.

The obviously missing part of the modeled S_2 emission spectrum is the so called "clump" emission around 100 cm^{-1}. As proposed by Zwier and co-workers, these bands are not

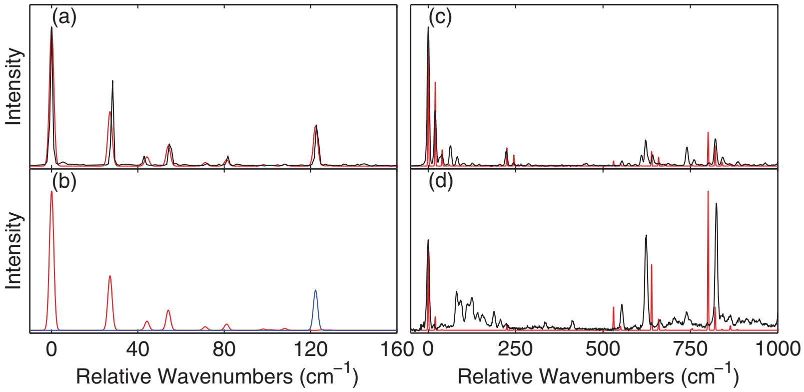

FIG. 8. DPM spectra produced from parameters in Tables I and III with an electronic coupling constant of 155.8 cm^{-1}. Comparison of the calculated (red) and experimental (black) absorption spectra is shown in (a). Breakdown of the calculated spectrum by the electronic state, with the red trace representing the S_1 (anti-symmetric) state and the blue trace representing the S_2 (symmetric) state in (b). (c) and (d) Comparisons of the calculated (red) and experimental (black) emission spectra from the S_1 and S_2 origins, respectively.

vibronic progressions off the S_2 state but emissions from the S_1 vibrational bands that gain their intensity due to the energetic proximity to the S_2 origin.[29] Indeed, the simulation produces two vibronic S_1 states (with very low intensity) within ±10 cm^{-1} of the S_2 origin. One of them is mainly composed of $T^3\bar{T}^3$ hot band, and another one is a mixture of $T^5\bar{T}$ and $T^6\bar{T}$. We mimicked the "clump" emission spectrum by producing emission spectra from these two vibronic states and adding them in equal proportions, and fitting the intensity of the combined spectra to the experimental "clump" emission. The resulting spectrum is provided in Fig. 9. The modeled "clump" spectrum qualitatively reproduces the experimental emission in the region 0−200 cm^{-1}, with a low-intensity region from 0−80 cm^{-1} followed by a clump of peaks. Thus, our results are in accord with assignments suggested by Zwier.[29]

V. CONCLUSIONS

The vibronic model has been extended to treat asymmetric molecules and inter-chromophore vibrational modes. Several vibrational modes can be considered simultaneously by means of Lanczos diagonalization of the sparse Hamiltonian matrix. Considered model spectra provide detailed analysis of the theory, including effects of simultaneous modeling of several modes and effects of asymmetries in different kinds in intra- and inter-monomer vibrations.

Modeling of the vibronic spectra of DPM demonstrates applicability of the developed model to real-life bichromophores. It is found that obtaining accurate parameters for the FG model may be challenging, especially parameters for the low-frequency inter-monomer modes that require computations of optimal geometries and vibrational frequencies of a bichromophore. However, inclusion of the inter-monomer modes is essential for modeling spectra of flexible bichromophores. Using the computed parameters for the intra-monomer modes and partly fit parameters for the inter-monomer modes, the experimental absorption and emission spectra of DPM were successfully reproduced. Additionally, a qualitative modeling of the clump emission spectrum was provided, even though a more rigorous theoretical framework may be needed in order to provide physically meaningful rather than fit representation of this region.

Future work will include applications of the developed model to asymmetrically deuterated diphenylmethane and other related asymmetrically substituted bichromophores, as well as extensions of the vibronic model to electronic asymmetries and tri- and multi-chromophore complexes.

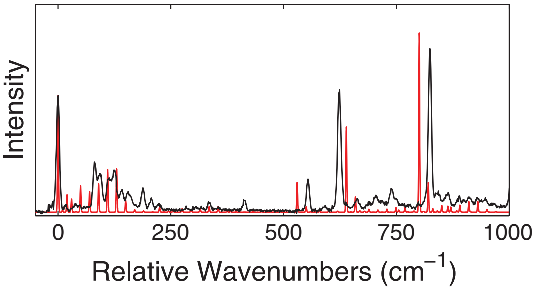

FIG. 9. S_2 "clump" emission spectra. The calculated spectrum (in red) is produced by adding S_2 emission spectrum as in Fig. 8(d) with emissions from energetically close S_1 vibrational states. Experiential spectrum is in black.

ACKNOWLEDGMENTS

This work was supported by National Science Foundation (NSF) Career Grant No. CHE-0955419 and Purdue Research Foundation. B.N. was partly supported by Andrews Graduate Fellowship. The authors thank Professor Tim Zwier, Dr. Christian Müller, and Dr. David Plusquellic for many fruitful discussions related to this work.

[1] M. Born and R. Oppenheimer, Ann. Phys. **84**, 0457 (1927).
[2] G. A. Worth and L. S. Cederbaum, Annu. Rev. Phys. Chem. **55**, 127 (2004).
[3] J. C. Tully, Int. J. Quantum Chem. **40**, 299 (1991).

[4] P. Ehrenfest, Z. Phys. A: Hadron Nucl. **45**, 455 (1927).

[5] H.-D. Meyera and W. H. Miller, J. Chem. Phys. **70**, 3214 (1979).

[6] U. Manthe, H.-D. Meyer, and L. S. Cederbaum, J. Chem. Phys. **97**, 3199 (1992).

[7] R. Kosloff, J. Phys. Chem. **92**, 2087 (1988).

[8] A. Witkowski and W. Moffitt, J. Chem. Phys. **33**, 872 (1960).

[9] R. L. Fulton, J. Chem. Phys. **56**, 1210 (1970).

[10] R. L. Fulton and M. Gouterman, J. Chem. Phys. **35**, 1059 (1961).

[11] A. Witkowski, in *Modern Quantum Chemistry*, edited by O. Sinanoğlu (Academic, New York, 1965), Vol. III.

[12] A. R. Gregory, W. H. Henneker, W. Siebrand, and M. Z. Zgierski, J. Chem. Phys. **63**, 5475 (1975).

[13] W. Siebrand, J. Chem. Phys. **40**, 2223 (1964).

[14] P. Petelenz and M. Andrzejak, J. Chem. Phys. **113**, 11306 (2000).

[15] K. Sakota and H. Sekiya, J. Phys. Chem. A **109**, 2718 (2005).

[16] M. Andrzejak and P. Petelenz, Chem. Phys. **335**, 155 (2007).

[17] P. Ottiger, S. Leutwyler, and H. Koppel, J. Chem. Phys. **131**, 204308 (2009).

[18] C. G. Heid, P. Ottiger, R. Leist, and S. Leutwyler, J. Chem. Phys. **135**, 154311 (2011).

[19] C. P. Rodrigo, C. W. Müller, N. R. Pillsbury, W. H. James III, D. F. Plusquellic, and T. S. Zwier, J. Chem. Phys. **134**, 164312 (2011).

[20] A. M. Kelley, J. Chem. Phys. **119**, 3320 (2003).

[21] J. Guthmuller, F. Zutterman, and B. Champagne, J. Chem. Theory Comput. **4**, 2094 (2008).

[22] J. Guthmuller, F. Zutterman, and B. Champagne, J. Chem. Phys. **131**, 154302 (2009).

[23] J. Seibt, V. Dehm, F. Wuerthner, and V. Engel, J. Chem. Phys. **126**, 164308 (2007).

[24] F. C. Spano and L. Silvestri, J. Chem. Phys. **132**, 094704 (2010).

[25] C. Woywod, W. Domcke, A. L. Sobolewski, and H.-J. Werner, J. Chem. Phys. **100**(2), 1400 (1994).

[26] M. Feigel, J. Mol. Struct.: THEOCHEM **366**, 83 (1996).

[27] R. Coffman and D. S. McClure, Can. J. Chem. **36**, 48 (1958).

[28] D. S. McClure, Can. J. Chem. **36**, 59 (1958).

[29] N. R. Pillsbury, J. A. Stearns, C. W. Müller, D. F. Plusquellic, and T. S. Zwier, J. Chem. Phys. **129**, 114301 (2008).

[30] J. A. Stearns, N. R. Pillsbury, K. O. Douglass, C. W. Müller, T. S. Zwier, and D. F. Plusquellic, J. Chem. Phys. **129**, 224305 (2008).

[31] T. Förster, in *Modern Quantum Chemistry*, edited by O. Sinanoğlu (Academic, New York, 1965), Vol. III.

[32] C.-P. Hsu, G. R. Fleming, M. Head-Gordon, and T. Head-Gordon, J. Chem. Phys. **114**, 3065 (2001).

[33] C.-P. Hsu, Acc. Chem. Res. **42**, 509 (2009).

[34] J. E. Subotnik, J. Vura-Weis, A. J. Sodt, and M. A. Ratner, J. Phys. Chem. A **114**, 8665 (2010).

[35] G. D. Scholes and K. P. Ghiggino, J. Phys. Chem. **98**, 4580 (1994).

[36] J.-L. Bredas, D. Beljonne, V. Coropceanu, and J. Cornil, Chem. Rev. **104**, 4971 (2004).

[37] See supplementary material at http://dx.doi.org/10.1063/1.4747336 for analysis of the convergence of vibronic spectra with a size of the vibrational basis, application of the perturbation theory to the strong and weak coupling limits, and visualization of the DPM inter-monomer vibrations.

[38] E. G. McRae and W. Siebrand, J. Chem. Phys. **41**, 905 (1964).

[39] E. Condon, Phys. Rev. **28**, 1182 (1926).

[40] C. Lee, W. Yang, and R. G. Parr, Phys. Rev. B **37**, 785 (1988).

[41] S. H. Vosko, L. Wilk, and M. Nusair, Can. J. Phys. **58**, 1200 (1980).

[42] A. D. Becke, J. Chem. Phys. **98**, 1372 (1993).

[43] J. Thom and H. Dunning, J. Chem. Phys. **90**, 1007 (1989).

[44] Y. Shao, L. Molnar, Y. Jung, J. Kussmann, C. Ochsenfeld, S. Brown, A. Gilbert, L. Slipchenko, S. Levchenko, D. O'Neil, R. DiStasio, Jr., R. Lochan, T. Wang, G. Beran, N. Besley, J. Herbert, C. Lin, T. Van Voorhis, S. Chien, A. Sodt, R. Steele, V. Rassolov, P. Maslen, P. Korambath, R. Adamson, B. Austin, J. Baker, E. Bird, H. Daschel, R. Doerksen, A. Drew, B. Dunietz, A. Dutoi, T. Furlani, S. Gwaltney, A. Heyden, S. Hirata, C.-P. Hsu, G. Kedziora, R. Khalliulin, P. Klunziger, A. Lee, W. Liang, I. Lotan, N. Nair, B. Peters, E. Proynov, P. Pieniazek, Y. Rhee, J. Ritchie, E. Rosta, C. Sherrill, A. Simmonett, J. Subotnik, H. Woodcock III, W. Zhang, A. Bell, A. Chakraborty, D. Chipman, F. Keil, A. Warshel, W. Herhe, H. Schaefer III, J. Kong, A. Krylov, P. Gill, and M. Head-Gordon, Phys. Chem. Chem. Phys. **8**, 3172 (2006).

[45] V. Mozhayskiy and A. Krylov, ezSpectrum, see http://iopenshell.usc.edu/downloads/.

[46] J. P. Perdew, Phys. Rev. B **33**, 8822 (1986).

[47] A. D. Becke, Phys. Rev. A **38**, 3098 (1988).

[48] J.-D. Chai and M. Head-Gordon, Phys. Chem. Chem. Phys. **10**, 6615 (2008).

[49] J. F. Stanton and R. J. Bartlett, J. Chem. Phys. **98**, 7029 (1993).

[50] H. Sekino and R. J. Bartlett, Int. J. Quantum Chem. **26**, 255 (1984).

[51] H. Koch, H. J. A. Jensen, P. Jørgensen, and T. Helgaker, J. Chem. Phys. **93**, 3345 (1990).

[52] A. Krylov, Annu. Rev. Phys. Chem. **59**, 433 (2008).